Colour Centres in 2-D hexagonal Boron Nitride

SAJID ALI

A thesis submitted in fulfilment for the degree of Doctor of Philosophy

School of Mathematical & Physical Sciences
Faculty of Science
UNIVERSITY OF TECHNOLOGY SYDNEY
AUSTRALIA

29-04-2019

Declaration of Authorship

I certify that the work in this thesis has not previously been submitted for a degree nor has it been submitted as part of requirements for a degree except as part of the collaborative doctoral degree and/or fully acknowledged within the text. I also certify that the thesis has been written by me. Any help that I have received in my research work and the preparation of the thesis itself has been acknowledged. In addition, I certify that all information sources and literature used are indicated in the thesis. This research is supported by Australian Government research training programme.

Signature of Student: Production Note: Signature removed prior to publication.

Date: 29-04-2019

Abstract

Point defects in semiconductors show a rich spin and optoelectronic physics that can be exploited to fabricate qubits for quantum computing technology as well as for single photon sources for quantum cryptography. This thesis contains a detailed study of emission from point defects in hexagonal boron nitride using density functional theory (DFT) and quantum chemistry approaches with an objective to identify the source of observed single photon emission. A survey of possible defects responsible for observed emission is performed using computationally inexpensive generalized-gradient approximation (GGA), Perdew-Burke-Ernzerhof (PBE) and those defects that form localized states with an energy gap of $\sim$2 eV are picked for calculations using highly non-local Heyd-Scuseria-Ernzerhof hybrid functional (HSE06). The photoluminescence line shape is calculated and compared with experiment to propose the most likely defects causing the observed emission. The standard DFT approaches are found to be inaccurate when compared with ab initio CCSD(T), EOM-CCSD, and CASPT2 approaches in predicting the excited-state energies, especially when dealing with states which have considerable open shell character. Thus, a benchmarking scheme is proposed and correction factors are devised for DFT energies. Finally, limitations of the finite model compound used in ab initio calculations are discussed and a possible solution is presented. A complete optical cycle of the likely defects is predicted using results from the HSE06 DFT approach, that are corrected by applying results from the high-level ab initio calculations. Finally, group theoretical analysis of defects is performed and possible applications in quantum computation technology are proposed.

Division of thesis

The division of this thesis is as follows. In Chapter 1, the overall theme of this work and how different concepts fit together is presented. In Chapter 2, the relevant experimental and theoretical literature is reviewed regarding the properties of emitters in h-BN and the context of the present work is presented in detail. In Chapter 3, the computational methods used in this thesis are presented. Chapter 4 contains the results for a survey of different possible emitting centres in h-BN. In Chapter 5, hyperfine coupling parameters are presented and comparisons are made with the experiments. Chapter 6 discusses inaccuracies in DFT energies and compares the calculated energies with ab initio CCSD(T), EOM-CCSD, and CASPT2 approaches. Correction factors for the DFT calculations are also proposed. Chapter 7 contains a study of the spectroscopy of likely defects responsible for the emission from h-BN using the DFT (HSE06) results, after applying correction factors devised in Chapter 6. and proposed optical cycles of the defects. The calculated photoluminescence line shapes for selected transitions are also presented. Polarization of allowed transitions are identified along with spin-orbit coupling driving non-radiative transitions. Zero-field splitting parameters are also presented and potential applications of the studied emitters in quantum applications proposed. Finally, a brief summary of the outcomes of this thesis and proposed future studies are presented.

Acknowledgment

I do not have words to pay gratitude to **Prof. Jeffrey R. Reimers**. All I can say is I am thankful to him for being an inspirational mentor and motivator during the course of my PhD studies. His research approach and scientific vision immensely influenced my thoughts and shaped my ideas. I am lucky to have worked under his guidance.

I am also profoundly thankful to **Prof. Mike Ford** for his guidance, support and priceless advice about my research and career. I pay sincere gratitude to him for helping me during my PhD research and guiding me in writing of this thesis.

A word of thanks to **Rika Kobayashi** for the technical help.

Finally, I would like to express my feelings of deep love and affection for my **mother, Late farther, and sisters**, as without their moral and emotional support and sensation of a strong family bond I would not have even imagined for a career in science.

Lastly, I dedicate the work to one who has never met me but is with me timelessly**…….**

SAJID ALI

List of Publications from this Work

1. **Sajid, A**.; Reimers, J. R.; Ford, M. J., Defect states in hexagonal boron nitride: Assignments of observed properties and prediction of properties relevant to quantum computation. *Physical Review B* **2018,** *97* (6).

2. **{Sajid, A.**; Tawfik, S. A.}[Equal Authors]; Fronzi, M.; Kianinia, M.; Tran, T. T.; Stampfl, C.; Aharonovich, I.; Toth, M.; Ford, M. J., First-principles investigation of quantum emission from hBN defects. *Nanoscale* **2017,** *9* (36), 13575-13582.

3. Reimers, J. R.; **Sajid, A.**; Kobayashi, R.; Ford, M. J., Understanding and Calibrating Density-Functional-Theory Calculations Describing the Energy and Spectroscopy of Defect Sites in Hexagonal Boron Nitride. *Journal of Chemical Theory and Computation* **2018,** *14* (3), 1602-1613.

4. Grosso, G.; Moon, H.; Lienhard, B.; **Sajid, A**.; Efetov, D. K.; Furchi, M. M.; Jarillo-Herrero, P.; Ford, M. J.; Aharonovich, I.; Englund, D., Tunable and high-purity room temperature single-photon emission from atomic defects in hexagonal boron nitride. *Nature Communications* **2017,** *8*.

5. Z. Xu, C. Elbadawi, T. T. Tran, M. Kianinia, X. Li, D. Liu, T. Hoffman, M. A. Nguyen, S. Kim, J. Edgar, X. Wu, L. Song, **Sajid, A.**, M. Ford, M. Toth, and I. Aharonovich, Single photon emission from plasma treated 2D hexagonal boron nitride. *Nanoscale* **2018,** *10* (17), 7957-7965.

6. **Sajid, A.**; Reimers, J. R.; Kobayashi, R.; and Ford, M. J., Improved methods for predicting the properties of defect states in 2D materials, applied to examine the V_NN_B defect in hexagonal boron nitride. *Journal of Chemical Theory and Computation (submitted)*.

7. **Sajid, A.**; Reimers, R.; and Ford, M. J., Single photon emitters in hexagonal Boron Nitride: A review of progress *(in preparation)*.

Other Publications during this time

1. G. Murtaza, **Sajid. A**., M. Rizwan, Y. Takagiwa, H. Kachai, M. Jibran, R. Khenata, S. Bin Omran. First principles study of Mg_2X (X=Si, Ge, Sn, Pb) Elastic, optoelectronic and thermoelectric properties. *Material Science in Semiconductor Processing*, (2015), 40, 429-435.

2. I. Zhu, L. L. C Lem, T. Nguyen, K. Fair, **Sajid. A**., M. J Ford, M. R. Phillips and C. Ton-That, Indirect excitons in hydrogen-doped ZnO. *Journal of Physics D: Applied Physics 2017*, 50.

3. **Sajid A**, Opto-Electronic Properties of Li_2C_2 Polymorphs. *Madridge J Nano Tech*. 2017, 2(1), 74-76.

4. Munir T, Munir HS, Kashif M, Fakhar-E-Alam M, Shahzad A, Amin N, **Sajid. A.**, Umair M., Synthesis and characterization of Copper Oxide nanoparticles by solution evaporation method. *Optoelectronics and Advanced Materials.* 01 May 2017, 19(5-6), 417-423.

5. M. Azizar Rahman, **Sajid. A.**, A. Gentle, Matthew R. Phillips, Michael J. Ford, Cuong Ton-That Wavelength tunable light source in individual ZnO microrod by Ga incorporation*(submitted)*.

Major Conference Presentations

1. **Sajid, A.**; Reimers, R.; and Ford, M. J. "Defect states in hexagonal boron nitride: Assignments of observed properties and prediction of properties relevant to quantum computation", *ICONN*, 29th January – 2nd February, 2018, Wollongong, Australia.

2. **Sajid, A.**; Reimers, R.; and Ford, M. J., "Emission from Point defect in Hexagonal Boron Nitride", 19th World Congress on Materials Science and Engineering, June 11-13, 2018, Barcelona, Spain.

3. **Sajid, A.**; Reimers, R.; and Ford, M. J., **"**Single photon emission from Hexagonal Boron Nitride", *ISHHC18*, July 22-25, 2018, Sydney, Australia.

Table of Contents

List of Figures

List of Tables

Chapter 1 Introduction

"Crystals are like people, it is the defects in them which tend to make them interesting!"

- Colin Humphreys

Imagine a situation in which you have two choices: to live your life with someone who is flawless, perfect, and fanatic in following rules and routines and is always predictable! Boring? Or, on the other hand, live with an unpredictable and imperfect person. You definitely will make the second choice, which is fair enough. Nature also made the second (wiser) choice some 4.5 billion years ago when some of the early crystals e.g. Zircon (The oldest crystal on earth found in Western Australia) were formed, and persisted with this choice for all the other naturally occurring materials on earth to make the world interesting and colourful for us. Courtesy of this choice (thermodynamic conditions) defects naturally occur in all materials and can be of different dimensions e.g. zero dimensional point defects, one dimensional edge and screw dislocations, two dimensional grain boundaries and stacking faults and three dimensional pores and cracks. Defects may occur at a small scale but they strongly affect the macroscopic properties of materials e.g. small amount of carbon in iron makes steel, which is stronger than pure iron. Semiconductors are well known to host both intrinsic and extrinsic point defects, which dramatically change their electronic, optical and electrical properties.

Defects either occur naturally in semi-conductor materials due to unintentional incorporation of impurities during the growth process or can be deterministically produced through electron beam irradiation. Point defects can act as colour centres in semiconductors, when they absorb (and emit) a particular wavelength of visible light. The existence of fluorescent point defects at low enough density can enable a few single photon emitters (SPE's) to be isolated and be stable at room temperature. This happens when at least one of the electronic states responsible for the emission is spatially localised, for example a defect state that is far from the bulk valence and conduction states of the host lattice. Single photon emitters (SPE's) play an important role in many leading quantum technologies [1,2], and provided their electronic structure and magnetic properties are known well, they can be employed for many purposes from quantum sensing [3-6], quantum nano-photonics [7-9] and quantum information processing [10,11]. Previously, the negatively charged nitrogen-vacancy (N_V^{-1}) centre in

diamond has emerged as a promising room temperature stable single photon-emitting source in the visible region. Some of other semiconducting systems known to host room temperature SPE's are the silicon vacancy centre in diamond, defects in silicon-carbide (SiC) and zinc-oxide (ZnO) [12,13].

Discovery of SPE from 2D materials has opened a new arena of research because of the unique optical and structural properties possessed by these SPE's [11,14-20]. Strong luminescence owing to the close proximity of emitter to the surface makes them promising for applications in high quantum efficiency applications. Other unique advantages possessed by SPE's in 2D materials are ease of coupling with waveguides and integratibility with other 2D materials. Hexagonal boron nitride (h-BN) is one such wide bandgap 2D semiconductor material, which has become very popular recently due to the observation of room temperature single photon emission (SPE) in both the visible [11,21-28] and UV regions [29-31]. SPE'S in h-BN possess ultra-high brightness, full polarization, and tuneable emission [32] making them very interesting for quantum sensing and optical communications. However to employ them in practical applications needs a thorough understanding of their geometrical, chemical, electronic and magnetic structure. This is a significant scientific challenge!

It has taken considerable effort over a decade or so to understand the underlying mechanisms of SPE in the N_V^{-1} colour centre, its energy level structure and excitation and decay pathways [33]. Despite this, there are still detailed features of the emission from this defect that are under debate, for example interaction with phonons [34]. The physics of SPE from defects in SiC is even less clear than the nitrogen-vacancy (N_V^{-1}) centre in diamond [35].

As discussed earlier, exploitation of these color centers in real applications requires a detailed knowledge of their electronic structure and magnetic properties. Accurate and reliable theoretical approaches for predicting electronic structure of ground and excited states are critical in this regard, and when combined with group theoretical analysis provide powerful tools for predicting the defect's optical cycle. An important feature is that DFT and time-dependent (TD) DFT can suffer various severe failings depending on the type of density functional used and the nature of the state being considered [36-43], demanding that great care be taken.

The discovery of SPE from h-BN monolayers and multilayers is relatively recent i.e. 2016 [11], the origin of the emission is currently under intense debate. Several experimental investigations and density functional theory (DFT) based computations have attributed the emission to point defects [11,27,44] such as vacancies, substitutions etc., with various color centers proposed. To enhance the contributions to this discussion from electronic structure calculations, methodologies are required that can calculate ground and excited-state energies to chemical accuracy, i.e., to better than 0.1 eV. This is extremely challenging for excited states (and ground states in some instances) where both dynamic and static correlation need to be included.

In this thesis, I attempt to identify the source of SPE from h-BN by calculating the properties e.g. photoluminescence line shape, hyperfine coupling parameters, excited state energies, zero field splitting, and by predicting the optical cycle of possible defects and making comparisons with available experimental data. The group theoretical analysis is performed to predict the potential application of various defect centres in quantum computation technologies. I identify the limitations of DFT approaches in calculating the excited state energies by comparing DFT energies with much more accurate quantum chemistry approaches. The latter calculations are, by necessity, limited to model compounds - non-periodic representations of the defect atomic structure. I propose correction factors and identify the limitations of the model compound approach. This work will help to understand the nature of emission from h-BN, as well as provide a much-needed step forward in assessing computational approaches applicable to the theoretical spectroscopy of defects in general.

Chapter 2 Review of Literature

Hexagonal boron nitride is a wide-band gap semiconductor which in bulk form has an indirect band gap of 6.08 eV [45]. While the band gap in monolayer or few-layer h-BN has not yet been determined experimentally, a recent theoretical calculation based upon an accurate version of DFT predicts the monolayer band gap to be direct with a value of 6.47 eV, with a cross-over to indirect occurring at two layers [46].

This material has shown promise as an ultra-violet emission source and evidence of lasing at UV wavelengths. Above band gap excitation reveals a number of features in the photoluminescence spectrum with a strong luminescence peak in the UV observed at 5.76 eV[47] that is assigned to recombination of the free exciton. The spatial distribution of this luminescence is homogeneous both in crystallites[48,49] and few-layer flakes[50,51] as measured by spatially resolved cathodoluminescence. Additional luminescence bands centred at 5.5 eV and 4 eV[48,52-55] are strongly localized near dislocations and boundaries[48-51] and have been assigned to defect states. The chemical nature of the defects responsible is still under debate. More recently anti-bunching (confirmation of single photon nature) has been demonstrated for this defect emission at 4.1 eV[56].

Photoluminescence in the visible part of the spectrum following below band gap excitation is also observed in bulk, few-layer and monolayer h-BN. Following the first observation of this emission as a bright, photo-stable source of single photons in 2016 by Tran et al [11] there has been considerable interest in this two-dimensional materials for its nanophotonic applications. Much of this work, both experimental and theoretical, has aimed at understanding the photo-physics of the emission in order to exploit its potential in applications such as quantum technology and quantum sensing. It is this body of literature that will be reviewed in the current chapter, in order to collect the varied work into the context of this thesis and as an aid in unravelling the origin of this quantum emission.

In this chapter, I will present an overview of the properties of SPE's in h-BN revealed by experiments and the corresponding computational efforts to interpret these observed properties in relation to the underlying electronic structure of possible defect centres responsible for emission. Here I would like to mention that the theoretical/computational research progress in

this direction is pioneered by the work presented in this thesis, I therefore discuss in detail the major computational/theoretical limitations and challenges identified in this work and propose possible solutions. I critically analyse the available literature and briefly state how this work fits in the overall scheme of things (with the detail to come in the following chapters). Before commencing a detailed review of the literature on SPE in h-BN, it is worth providing a brief review of the SPE and its application to quantum technology and a summary of current state of play regarding quantum sources in wide band gap semiconductors. There are detailed discussions on both of these points available in the literature [35,57].

2.1 The role of single photon sources in quantum technologies

Single photon sources are at the heart of all proposed quantum technologies such as communication, computations and metrology. A number of systems have already been utilized in such technologies including atoms [57], quantum dots [58] and superconducting circuits [59]. An ideal SPE is that which emits one photon per excitation pulse. In order for an SPE to be employed for quantum information processing it should meet other requirements (a general set of requirements) schematically shown in Fig. 2.1. Finding all of these features in one system is a major challenge, and currently no solid-state system possess all of these properties.

SPE'S based on atoms or trapped ions and quantum dots have excellent optical properties [60,61], however scalability and integration issues (in case of atoms or trapped ions) and problem of low-coherence times and indistinguishability (in case of quantum dots) prevents their usage in practical applications. Some of these issues are currently being investigated in detail [62].

The major challenge towards developing quantum technologies is the ability to address and control an isolated quantum system. Point defects in semi-conductors offer an attractive paradigm system in which these contradictory features i.e. isolation and access can be combined. An electrically driven point defect in a semiconductor with an electronic state in the bandgap is similar to an isolated atomic (quantum) system. The spin state associated with energy levels of defect represents the basic unit of information in quantum technology called a qubit [63]. SPE's based on semiconductors offer attractive features such as photostable emission, room temperature operation and long coherence times. SPE's in semiconductors also

offer ease of integration with nano-photonic devices and therefore are the most promising for practical applications. The application of point defect based SPE's for quantum technologies have already been demonstrated (to varying extents) in quantum computation [64], quantum communication [65] and metrology [66].

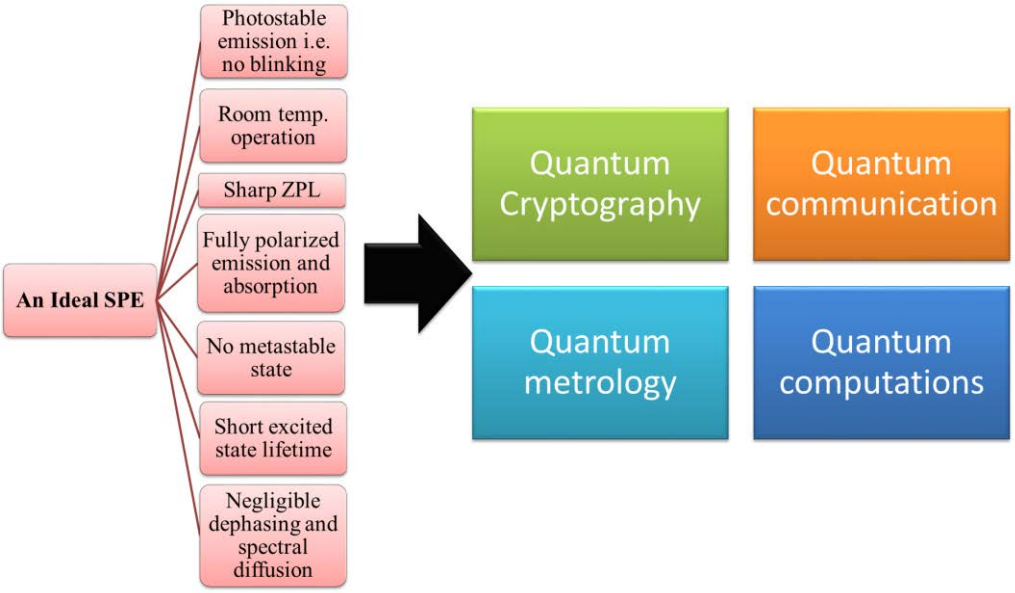

Figure 2.1 Major requirements that an SPE should meet to be employed in quantum technologies [13,35,57].

2.2 Defects in semi-conductors as single photon emitters

The luminescence spectrum of a defect is composed of the zero-phonon line (ZPL) and its phonon sidebands. The contribution of the luminescence intensity (ZPL intensity) relative to the total (ZPL + phonon side band (PSB)) integrated intensity is the Debye-Waller (DW) factor. DW factor is a quantity that is directly measurable in an experiment, while another important factor called Huang Rhys factor (HR) is deduced from DW factor i.e. $HR_{factor} = -\ln(DW_{factor})$ in practical situations (Note: In this thesis standard definition of HR factor i.e. "total number of phonons of all kinds emitted during a transition" is used). DW factor is a critical parameter for application of an SPE in technology, defect systems with high DW factors are desirable for use in long-range quantum computation and communication [13,35,67], as the ZPL photons then have sharp (strong) intensity and well-defined polarization (plane-polarization). Another critical parameter for SPE's is the quantum efficiency defined as the ratio of radiative rate to overall (radiative + non-radiative) rate.

So far, the N_v^{-1} centre in diamond is the most thoroughly studied SPE whose crystallographic and electronic structure has largely been resolved. SPEs in diamond are photostable, operate at room temperature and have long coherence times. However the N_v^{-1} centre have a DW factor of only 3% [68] even at low temperature, which limits it's applicability for quantum technologies. The quantum efficiency of N_v^{-1} centre in diamond is also low i.e. 0.7, due to the existence of a metastable state (alternative decay channel) [68]. In addition, N_v^{-1} has a non-zero electric dipole moment in both the ground and excited state making it sensitive to local electric fields due to strain for example, which contributes to undesirable homogeneous and inhomogeneous broadening [13]. The silicon vacancy (Si_V) centre in diamond possesses inversion symmetry and has a high DW factor of 70% [69] but has a low quantum efficiency of 0.035. Similarly defects in other materials e.g. SiC have lower DW factors of 33% and quantum efficiency of 0.7 [70]. Extensive experimental and theoretical studies are being performed to explore new solid-state systems that are potential hosts of SPE's that have parameters that are closer to the ideal SPE. One positive result of such studies is the discovery of SPE in 2D h-BN [11], which in some circumstances appears to have a high DW (estimates of up to 82% have been proposed in the literature [11] and a spectrally varying quantum efficiency in the range 0.5-1.0 [71]. Because of these superior properties, h-BN has attained considerable attention from the research community (both experimental and theoretical) [28,44,71-85]. In the following, I will focus on SPE's in h-BN. I will critically analyse the observed properties of SPE's in h-BN in connection with the computational studies done far.

2.3 Properties of SPE's in h-BN

Understanding the physics of defect emission requires an understanding of the electronic states involved and how they couple to vibrational motion on the defect atoms and surrounding lattice. This is best illustrated using a configuration co-ordinate diagram such as shown in Fig. 2.2. The diagram shows the relationship between changes in the defect geometry with changes in the electronic state of the defect, that is, a plot of the generalised potential energy surfaces for the ground and an excited state. An incoming photon can excite the system (by giving it energy $E_{absorb.}$) from the ground electronic potential energy surface into an excited state. At zero Kelvin, this excitation takes place out of the lowest vibrational state and produces a vertical transition that can take place abruptly without any change in defect geometry i.e. into

multiple vibrational levels of the upper potential energy surface. The defect can then relax to the equilibrium geometry of the excited state by losing energy through a non-radiative process. The energy lost in this latter process is termed as vibrational reorganization energy (λ_a). The system can then decay directly to the lowest vibrational state of the ground electronic state emitting a photon with energy (the zero phonon line) (E_{ZPL}) or radiate into excited vibrational levels of ground state giving rise to the phonon side bands. At finite temperature, it is also possible to absorb vibrational quanta during the decay. The total reorganization energy is a measure of overlap between ground and excited states ($\lambda = \lambda_a + \lambda_e$). Photoluminescence experiments can probe these decay processes under a variety of conditions revealing the ZPL energy, polarization and phonon sidebands. In this section, I will review the properties of reported SPE from h-BN in terms of some of these parameters. I also will summarize the magnetic properties, temperature dependence, zero field splitting and hyperfine coupling observed for these emitters. As all of these observed properties can provide a step towards revealing the actual structure of the culprit defect.

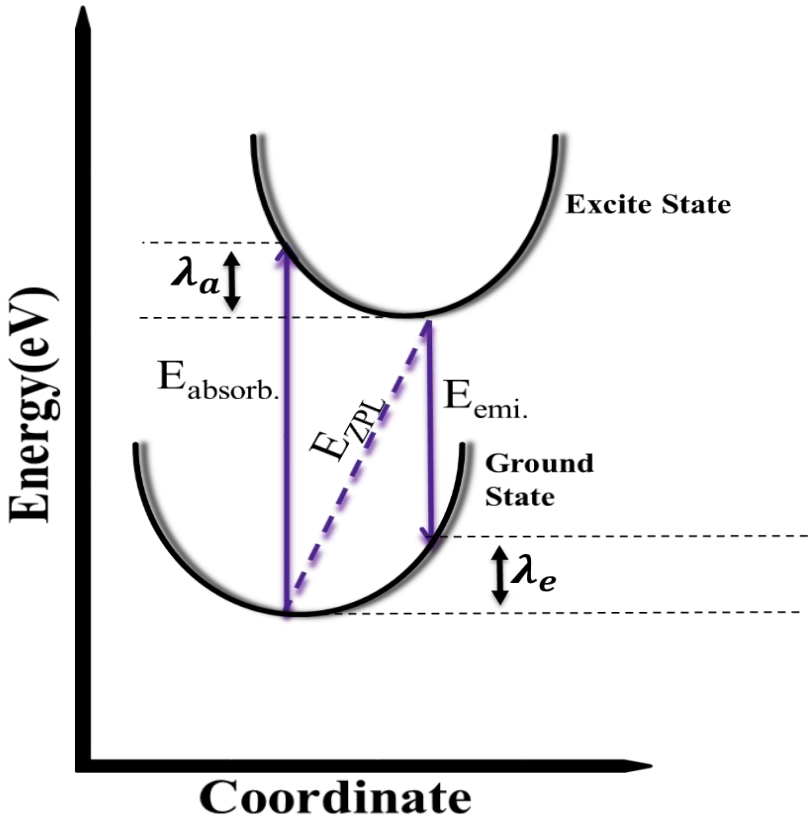

Figure 2.2 Configuration co-ordinate diagram showing important energies and optical transitions.

2.3.1 ZPL energy

Several groups across the globe have reported SPE from h-BN with some common features in terms of energy profile. In this section, I will review those common features and try to develop correlations. The first report on room temperature SPE from h-BN monolayers observed a ZPL energy of 1.99 eV and the emission was tentatively assigned to the V_NN_B defect [11]. Shortly after this, two different groups of emitters (group1 & group2) in h-BN were reported with different ZPL energies and phonon side-bands (PSB) [21]. Group 1 emitters had broad and asymmetric ZPLs with energies in the range 1.90 to 2.15 eV while, group 2 emitters had narrow and more symmetric ZPLs with energies in the range 1.63 to 1.82 eV [21]. Two of the Group 1 type emitters with ZPL energies centred at 1.82 eV and 2.16 eV were later studied for their spectral shift and temperature dependent line-width [86]. It was found that a 532 nm laser directly excites the emitter centred at 1.82 eV, while the other emitter is excited indirectly [86]. The line-widths were found to be 0.352 and 0.148 μeV for the 2.16 eV line and the 1.82 eV line, respectively. The amplitude of the 1.82 eV emitter was found to decrease much more rapidly with temperature compared to 2.16 eV emitter [86]. Similarly, two types of emitters were reported in another work , one with a broad ZPL centred at 2.15 eV and the other with a sharp ZPL at 1.45 eV [76]. The emitter with sharp ZPL was found to have almost no PSB [76]. Another group reported two families of highly efficient and ultra-bright quantum emitters in h-BN with ZPL centred at 1.97 eV and 2.08 eV [87]. To eliminate possible substrate effects on emission from h-BN, SPE's in suspended single crystalline h-BN films have been reported with ZPL energies in the range 1.77-2.25 eV [28]. SPE have also been demonstrated from h-BN powder and exfoliated h-BN flake with ZPL in the energy range of 1.8 -2.5 eV [81]. Room temperature SPE from zero-dimensional boron nitride allotrope (the boron nitride nano-cocoon) has also been demonstrated with ZPL energy centred around 2.14 eV [84]. A common feature of all these studies on SPE from h-BN is the presence of two type of emitters, suggesting there are two distinct defects or two different charge states of the same defect responsible for emission in the visible range. The subsequent studies on magnetic ground state of these emitters strongly suggest that the defects in h-BN form singlet-triplet systems [88], but still there is no direct evidence for this. Another study reports the presence of possible shelving states and possibility of different laser powers addressing different defect levels [89], which is suggestive

of a complex level structure of emitters in h-BN. This is also supported by another study, which reports large ZPL spectral diffusion and discrete jumps of up to 100 nm after exciting the emitters with blue lasers, while only a fraction of emitters fluoresce on green illumination and hence suggest complex level structure of these emitters and possibility of addressing different levels [90]. It has also been reported that the excitation efficiency as well as quantum efficiency of emitters in h-BN are strongly wavelength dependent and excitation wavelength has to be matched to the emitters to gain highest quantum efficiency, hence suggestive of complex level structure of the emitters [71]. Since in quantum optics it is highly desirable to have the ability to address different defect levels, making defects in h-BN even more attractive for these applications.

2.3.2 Strain tunability

For emitters in h-BN the ability to individually address defects levels accompanied with a mechanical control over emission wavelength by applying strain makes these even more useful. Spectral tunability of h-BN single photon emitters has been achieved over an energy range of 6 meV [32]. This observation has also been backed up with DFT simulations on a native defect species i.e. V_NN_B as shown in Fig 2.3. These simulations considered four strain directions along the plane of the h-BN sample, as labelled by the lattice directions shown in the inset of (shown in Fig 2.3). A realistic case, similar to experimental conditions, is taken into account by considering the effects of the Poisson's ratio of 0.37 of the bendable polycarbonate (PC) substrate. In these conditions, tensile strain along AC2 produces a compression along the orthogonal direction ZZ1: $\varepsilon_{ZZ1} = -0.37 \times \varepsilon_{AC2}$, and vice versa. The simulations also confirm the non-monotonic behaviour of the ZPL energy under the effect of strain and its role in the large spectral distribution observed experimentally [32].

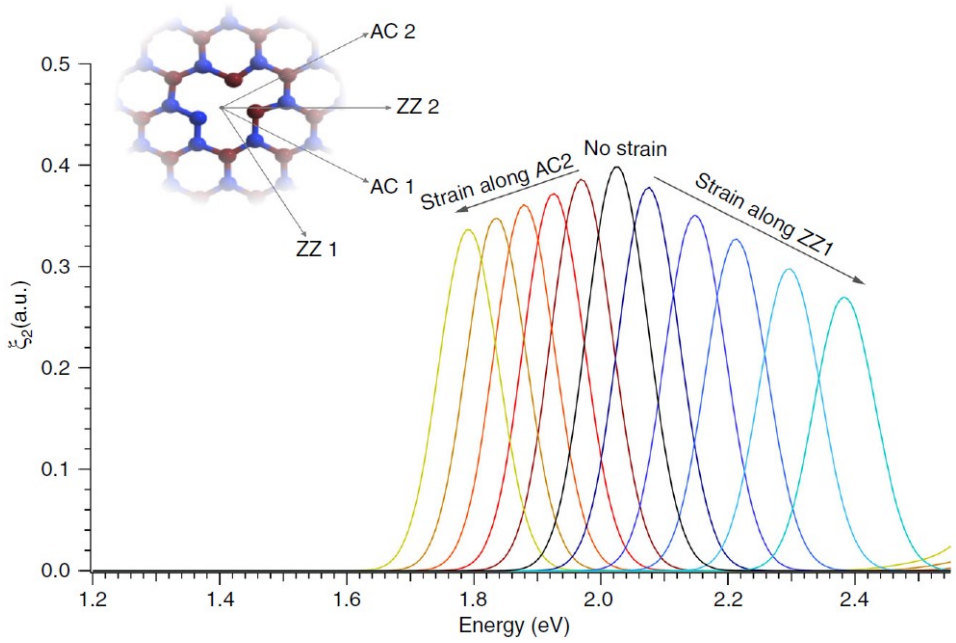

Figure 2.3 Simulated Spectral distribution as a function of strain. The cartoon in the inset shows the lattice directions in the plane of hexagonal lattice with respect to V_NN_B defect. Four independent directions can be identified; two along zigzag directions, ZZ1 and ZZ2 and two along the armchair directions, AC1 AND AC2. The main plot is simulated optical response in the form of imaginary part of dielectric function (ξ_2) as a function of the strain applied in either zigzag or armchair direction. The simulation takes into account the effect of high Poisson's ratio of the PC substrate of 0.37 that induces a compression (stretching) in the orthogonal direction with respect to the direction where tensile (compressive) strain is applied. The black graph shows the imaginary part of the dielectric function at zero strain. The graphs in red (blue) tones correspond to tensile strain applied along the AC2 (ZZ1) direction from 1 to 5%. In these conditions, the Poisson's ratio of PC substrate results in compression in the orthogonal direction from -0.27 to -1.85%.

This spectral tuning of up to 6 meV greatly increases the probability of spectral overlapping among different emitters. Although in this study [32], the emission dipole was in the plane of h-BN sheet, in general spin-preserved transitions can have their dipole in either the plane or perpendicular to the plane of h-BN sheet. In the next section, I discuss and review the emission dipole from h-BN emitters.

2.3.3 Emission dipole

In this section, I first discuss the effect of dipole allowed spin-preserved transitions. Such transitions may happen via dipole interaction. $H_{di} = \sum_j \sum_\alpha d_j^\alpha E_j^\alpha$, where $d = e(x,y,z)$ is the dipole moment of the electron and E is the electric field vector. Using the standard axis convention for C_{2v} point group, these allowed transitions are induced either by the axial (d_z) and plane-perpendicular (d_y) component of dipole moment i.e. $d_\parallel = d_z, d_y$ or out of plane

component i.e. $d_{\perp} = d_x$. Polarization measurements of the emission and absorption spectra of a defect reveal important information about defect level structure, symmetry and Inter-system crossing. The emission and absorption dipole have been found to be aligned (misaligned) for emitters in h-BN when excited at two different wavelengths, suggesting the indirect excitation of some of the emitters through a third intermediate electronic state [75]. The existence of a fast decaying intermediate and a long-lived metastable state accessible from the first excited electronic state has also been speculated in another recent study [88]. A level structure which can support a similar kind of misalignment of emission and absorption dipoles has been predicted in another recent study [79]. Polarized in-plane emission is observed after in-plane polarized light absorption, but the absorption can be either polarized parallel or else in-plane at some angle, e.g., 60° [75]. In principle, this could arise following, for one polarization, Franck-Condon allowed [91] transitions, and for the other polarization, Herzberg-Teller-allowed [92] vibronic transitions, all within the same electronic state [93]. However, the wide and variable energy spacing between the absorptions of different polarization imply that instead two states are involved, supporting Franck-Condon allowed, differently polarized, in-plane absorptions. This places strict requirements on the properties of defect states, especially those that are nominally of high symmetry such as V_NN_B, V_NC_B and V_BC_N etc. In its most symmetric form, V_NN_B, V_NC_B and V_BC_N would display C_{2v} symmetry, with all spectroscopic processes then restricted to those that this symmetry allows. Using the standard axis conventions for planar molecules [94,95], the irreducible representations of the C_{2v} point group are a_1 (d_z) and b_2 (d_y) (of σ type) and b_1 and a_2 (d_x) (of π type). Electronic excitations of A_1 symmetry are polarized in-plane along the defect C_2 axis, while those of B_2 symmetry are polarized in-plane orthogonal to this and allowed out-of-plane transitions have B_1 symmetry. Hence, the observed properties demand of V_NN_B, V_NC_B and V_BC_N is that its two lowest transitions be of A_1 and B_2 symmetry. Either spectral overlap of the two states, or else vibronic coupling between them, could modify the expected C_{2v}-based pure orthogonal polarization of the second state into some mixed polarization, accounting for the observed 60°-polarized absorption [75].

2.3.4 Interaction with vibrational modes

The width of the spectral bands (λ_a & λ_e) alone provides significant information, specifying the reorganization energy associated with the transition. Large change in nuclear coordinates between ground and excited state produces broad spectra; alternatively, if the transition is insensitive to nuclear motion, then the spectra will be sharp. Broad spectra are generally produced if orbitals from the valence or conduction bands of the h-BN are involved as interactions within these bands create a multitude of electronic transitions out of a single one. Sharp transitions are typically easier to observe and hence dominate experimental studies. Since, reorganization energy and Huang Rhys factor essentially give similar information about an optical spectrum, in this thesis both terminologies are used alternatively.

Amongst defects, there is a search for those that have defect orbitals lying within the bandgap that have allowed spectroscopic transitions [44]. Photoluminescence usually becomes the focus as it easier to observe than photo absorption as defects are usually present only in low concentration, with an added bonus often arising if the emitting state is different to the absorbing state and has different symmetry such that the absorption and emission polarizations vary [75]. The PL spectra from defects in h-BN reported in different studies are very sharp and intense and reorganization energies are very small i.e. 0.17 eV [75] and (0.2 to 1.0 eV) [21]. Group 1 emitters reported in ref. [21] has broad and asymmetric ZPLs, while group 2 emitters has narrow and more symmetric ZPLs [21]. Both groups of emitters show PSB at the B-N bond stretch frequency so both couple to this mode. However, surprisingly, the energy gap difference between ZPL and phonon side bands for two groups of emitters was found to be same i.e. 160 ± 5 meV [21]. Thus, the difference between shapes and ZPL energies for the two types of emitters may be attributed to difference in coupling to low energy phonon modes or to inhomogeneous broadening i.e. local environment. The latter speculation is also supported by the fact that two types of emitter have different radiative and non-radiative life times and thus the interaction of the two types of emitters with neighbouring impurities or the proximity of a centre to the surface is different [21].

Another recent study discusses the electron-phonon processes and the dephasing mechanisms of h-BN emitters at cryogenic temperatures and assigns the short photon

coherence time to ultrafast spectral diffusion (spectral broadening) present in these emitters, causing an inhomogeneous broadening of the line [96].

2.3.5 Magnetic state

Knowledge of the spin state of a semiconductor defects is necessary to exploit the defect's possible spin-dependent photoluminescence (PL) that facilitates initialization and readout of individual electron spins, along with their proximal nuclear spins [65]. In this section, I review the magneto-optical studies on SPE's in h-BN. Emitters in h-BN with non-magnetic ground and ultra-narrow and side band free emission have been reported earlier [76]. These emitters have been shown to be spatially correlated with structural defects in h-BN and are spatially independent of other types of emitters, having broad ZPL [76]. These emitters were tentatively assigned to di-vacancies (V_{BN}) in h-BN [76]. Another recent study reported no change in optical spectra of h-BN defects with the application of a magnetic field [81]. However in another recent work, anisotropic photoluminescence (PL) patterns were observed as a function of applied magnetic field for some selected emitters, while other emitters again show no change with applied magnetic field [79]. Systematic changes in brightness due to the applied magnetic field of some selected emitters in h-BN is suggestive of optically addressable spin of these emitters and hence a possible mechanism of spin-initialization and readout [79]. These variations are also suggestive of an electronic model featuring a spin-dependent ISC between triplet and singlet manifolds. A defect model with a singlet ground state configuration was tentatively proposed which accounts for all the experimental observations [79]. All these studies point toward a non-magnetic ground state of some of emitters in h-BN. This is consistent with the fact that no effect on ZPL with magnetic field have been seen from these defects in spite of many attempts [27]. Only recently however, defect species in h-BN with triplet ground state has been reported [97], indicating that more than one defects may be causing emission around 2 eV.

2.3.6 Temperature dependence

The temperature dependence of luminescence centres yield important information about electron-phonon coupling in the host semiconductor. The vibronic spectrum of a color centre with ZPL centred at 4.1eV has already been studied in detail [98]. In this section, I will

review the studies on temperature dependence of luminescence centres around 2 eV in h-BN. The room temperature quantum emission from h-BN is indicative of the existence of at least one localized orbitals within the h-BN band gap that is well isolated from bulk bands [11]. Quantum emitters in h-BN have been shown to be stable and operate at elevated temperatures [99]. A red shift in ZPL energy and broadening was seen with increase in temperature to 800K and both were found to be reversible upon cooling back to room temperature [99]. The shift in ZPL energy upon heating and cooling was tentatively assigned to the expansion of substrate lattice upon heating and electron-lattice interactions [99]. The stability of SPE from h-BN at elevated temperature is suggestive of possibility of using these in integrated quantum technologies for real-world environments. Another recent work, which investigated the temperature dependent line width, line shift, excited state lifetime, and intensity of quantum emitters in h-BN has also reported similar red shift and ZPL broadening for both types of emitters i.e. (1.82 eV and 2.16 eV) upon increasing the temperature [86]. Piezoelectric coupling to the low energy acoustic phonons was proposed to explain the exponential line width broadening of the ZPL [86] with temperature.

2.3.7 Hyperfine coupling

A standard method of defect identification is electron paramagnetic resonance (EPR) spectroscopy. A-priori calculations using density-functional theory (DFT) can provide useful tools for the interpretation of EPR data such as observed hyperfine tensors. Indeed, such calculations have been helpful in the identification of point defects in different semiconductors by comparing the experimental and calculated hyperfine constants [100-104]. Both unintentional occurrence of defects (e.g. vacancies) [105,106] during the preparation of single layer h-BN and the deterministic production of defects through electron beam irradiation [107] have been shown to have considerable effects on electronic and magnetic properties of h-BN. While both nitrogen (V_N) and boron (V_B) vacancies can act as paramagnetic centres in h-BN [108], electron paramagnetic resonance (EPR) studies indicate that N_v are more important [109-114]. Two types of paramagnetic centres have been identified: (i) three-boron centres (TBC) in which an unpaired electron interacts with three equivalent boron (B^{11}) nuclei, producing 10-line EPR spectra, and (ii) one-boron centres (OBC) in which oxidative damage at the centre forces the unpaired electron to interact with only a single B^{11}, producing 4-line EPR spectra.

The TBC can be deliberately produced either by irradiation [109-111] or by carbon doping [113], but controllable h-BN oxidation to produce OBCs has not yet been achieved. Of particular interest (in the context of this work) is that carbon-doped centres can give rise to intense PL [115,116]. In this thesis I have assigned observed h-BN electron-paramagnetic resonance (EPR) signals at 22.4 MHz (TBC), 20.83 MHz (TBC), and 352.70 MHz (OBC) to V_N, C_N, and V_NO_2, respectively [83]. I have also calculated the hyperfine coupling (HF) constants for various carbon-related anti-site defects, in which a nitrogen or boron vacancy is accompanied by a neighbouring carbon-atom and/or silicon-atom substitution. Indeed many EPR studies on h-BN samples need to be performed to assign this theoretical data for HF to possible emitting centres in h-BN. A recent EPR study has been performed which is a step forward in this direction [97]. The broad optical absorption band and near infrared photoluminescence band centred at ~490 nm and 820 nm, respectively were assigned tentatively to defect species with a triplet ground state [97]. Contrary to the non-magnetic quantum emitters [76], these defects have broad visible optical absorption band [97].

2.3.8 Zero field splitting

In general an $S = 1$ electron spin system is described by a spin Hamiltonian of the following form:$H = g_e\beta \boldsymbol{B}\hat{S} + \hat{S}D\hat{S}$. Here g_e is the electronic g-factor ($g_e = 2.0028 \pm 0.0003$); $\boldsymbol{B}$ is the external magnetic field and D is the zero field splitting tensor. This tensor comprises the anisotropic dipolar interaction of the two electron spins forming the triplet state averaged over their wave function. This tensor is traceless and thus characterized by two parameters, D and E i.e. the axial and rhombic zero-field splitting parameters, respectively. This spin-spin interaction arising because of the non-spherical shape of molecular orbitals lifts the degeneracy of multiplets. In this thesis I have calculated the spin-spin contribution towards zero field splitting parameters (D *and* E) for high spin ground states for V_NC_B (V_BC_N) and other defects [83]. Only V_BC_N was found to have triplet ground state with E=0.84 GHz and D=7.15 GHz [83]. A recent experimental study indeed reports the defect species with triplet ground state in h-BN. Although the measured value of 'D' i.e. 1.2 GHz is not in agreement with my calculations [97].

2.4 The theoretical/computational modelling

In this section, I briefly discuss the theoretical attempts made so far to reproduce the observed properties of SPE's in model defect systems in h-BN. I divide this section in two subsections to present clearly the contribution made by this work and by others.

2.4.1 This work

The work presented in this thesis pioneers most of the progress made in this direction (to un-earth the origin of emission), therefore I briefly discuss my work here with details to come in the later chapters. Theoretical studies so far have mainly focussed on point defects in h-BN [44,82,83,117,118]. The studies are built upon the following four criteria (actually proposed in this work [44]) for possible emitting centres. These criteria are motivated from experimental observations.

1. The stability of the emitters against high temperature annealing [99] imply that the positions of the defect levels are deep within the bandgap.

2. The observed emitters are in-plane polarized [11] as discussed earlier.

3. E_{ZPL} reported in different experimental papers for defects in h-BN is between 1.3 eV and 2.2 eV [11,28,32,75,84,86,99,119,120].

4. The emitters has a non-magnetic ground state [27].

In this work [44] (Chapter 4), I have surveyed several possible colour centres in h-BN, studied their ground and excited state structures. Based on the calculated electronic structure, ZPL energies, position of defect states within the bandgap and nature of transitions, a set of 13 possible defects are shortlisted as potential candidates. These include, but are not limited to, V_NN_B (a nitrogen vacancy and one of the surrounding boron replaced with a nitrogen), V_NC_B (nitrogen vacancy and one of surrounding boron replaced with a carbon) and V_BC_N (boron vacancy and one of surrounding nitrogen replaced with a carbon). All the other short listed defects are found to have large Huang-Rhys (HR) and hence large reorganization energy, meaning broad optical spectra. In the neutral state, only V_NC_B is found to have a low enough HR factor (1.66) to agree with experiment for 1^3B_1 to 2^3B_1 transition. Thus a luminescence line

shape is calculated for V_NC_B for transition between triplet manifold i.e. 1^3B_1 to 2^3B_1 using a first principles approach which has previously been applied successfully to N_v centre in diamond [121] and found to best fit the experimental line shape (see Fig. 7.4 in later chapters).

Later on (chapter 5 to chapter 7), I investigated in detail the defects V_NN_B (in neutral, +1 and -1 charge states) and V_NC_B in neutral charge state for satisfying the criteria's for possible emitters and having small HR factors and the defect V_BC_N for having a triplet ground state [82,83,122]. Since a standard method of defect identification is the comparison of calculated hyperfine coupling constants with experimental EPR data, I calculated (chapter 5) the hyperfine coupling constants for V_NN_B, V_NC_B, V_BC_N and some other important defects and made comparisons with available experimental EPR data [83].

In addition to this, the defects V_NC_B, V_BC_N and V_NN_B are benchmarked in this work (Chapter 6) [82,83,122] by comparing DFT energies of these defects with ab initio CCSD(T), EOM-CCSD, and CASPT2 calculations for a representative model compounds. Then I studied (Chapter 7) the spectroscopy of V_NC_B, V_BC_N and V_NN_B using DFT (HSE06) results, after applying correction factors obtained from benchmarking.

It is worth mentioning here that in a recent study a new non-planar ground state geometry has been predicted for V_NC_B and V_NN_B [123], thus bands involved in the transition would broaden due to out of plane distortion and HR factor would increase. Since the non-planar geometry is lower in energy by only 0.44 eV for V_NC_B and by 0.05 eV for V_NN_B, therefore significant changes are expected in the HR factor. However, because of the difficulty in assessing reliability of calculations to determine energy difference between planar and non-planar configuration, I only consider planar geometry (later discussed in detail). Therefore, in order to benchmark the DFT calculations and hence to have an estimate of how reliable the computational approaches are in predicting quantities like excited state energies I confine my calculations to the C_{2v} symmetry in this thesis and focus on achieving the high accuracy for calculation of defect manifolds.

2.4.2 Other's work

In the original work, based upon Density Functional Theory (DFT) calculations, the emission was tentatively assigned to the nitrogen antisite defect, V_NN_B [11]. Followed by our detailed survey of defects in h-BN [44], Abdi et al [73] mapped out the electronic structure and transitions for the nitrogen antisite defect, the negatively charged boron vacancy defect and the positively charged carbon antisite defect using a combination of group theory and DFT. The computed ZPL energies, the profile of excitation and emission dipole polarizations, and the competing relaxation processes were discussed and compared with the observed emission lines [73]. Furthermore, spin-orbit and spin-spin interactions were discussed in detail [73]. Here the hybrid HSE06 functional was combined with constrained-DFT to calculate excited state energies and propose the negative boron vacancy as the most promising candidate. However, one can argue [82,122] that calculation of excited states using ground state DFT is known to be problematic and the reliability of results needs to be assessed carefully, particularly where electronic states have considerable multireference character and static correlation becomes important. Another recent study [118] presents the calculated formation energies for the defects studied in my previous work [44], however the standard approach of calculation of formation energies for 3D materials cannot be applied to 2D systems like h-BN (because of different nature of homogeneous counter charged). In the following section, I discuss the major challenges involved in calculating the excited states energies and predicting formation energetics.

2.4.3 Major theoretical/computational challenges

The precise nature of observed defects is often difficult to determine, with potentially useful defects being difficult to predict, making popular their investigation by first principles computational techniques [44,100-102,104,124,125]. However, methods for performing accurate calculations of this type are still being developed. Small molecules containing the types of functionalities found in diamond and h-BN defects may be described to chemical accuracy using standard ab initio computational methods such as quantum Monte Carlo (QMC) [126], coupled-cluster singles and doubles (CCSD) [127] theory with perturbation corrections for triples excitations (CCSD(T)) [128], related time-dependent approaches such as equations

of motion coupled cluster (EOM-CCSD) [129,130], singles and doubles multi-reference configuration interaction (MRCI) [131], as well as its approximation, complete-active-space self-consistent field (CASSCF) [132] theory with perturbative corrections for singles and doubles excitations (CASPT2) [133]. While CCSD(T) is regarded as being the "gold standard" in molecular electronic structure computation, the multi-reference nature of many of the defect states of interest could demand QMC or MRCI approaches instead. The above ab initio methods are not yet available in solid state codes with periodic boundary conditions and so model compounds [134], i.e. small clusters containing the defect must be used. These ab initio approaches are also limited to relatively small numbers of atoms and clusters need to be of the order of 10 or so atoms in size before the calculations become prohibitively expensive. A range of improved high-level methods are available [135-154] but unfortunately rarely deployed.

Nevertheless, the most commonly applied approaches to electronic and nuclear structure simulation in modern times include DFT and its time-dependent variant, TDDFT. Despite having no method available for the systematic improvement of DFT calculations towards the exact answer, in practical calculations on sizeable molecules, DFT and TDDFT approaches can often deliver similar accuracy to their much more computationally expensive ab initio counterparts. DFT can be regularly applied to periodic systems, allowing an alternate approach to modelling defect sites. In molecular-cluster-based approaches, the size of the cluster must be increased until all long-range effects of interest are included, a difficult task if transitions involve the valence and/or conduction bands of the solid, whereas for periodic-solid approaches, the size of the unit cell must be increased until neighboring defect sites do not interfere with each other. Either way presents computational challenges.

An important feature is that DFT and TDDFT can suffer various severe failings depending on the type of density functional used and the nature of the state being considered [36-43], demanding that great care be taken. Since the identification of defects in semi-conductors relies on the ability to calculate ZPL energies within 0.1 eV accuracy. This level of accuracy can be achieved only if both static and dynamic electron correlation effects are taken into consideration. Therefore DFT energies need to be calibrated and benchmarked by performing ab initio calculations using the CCSD(T) [127,128], EOM-CCSD [129,130], and CASPT2 [155] and MRCI [156] methods on a model compound to make realistic predictions of

photoluminescence energies. The in-accuracies in the state energies due to static correlation effects can be predicted efficiently using this approach. However, the dynamic electron correlation effects in periodic structure can be quite different from those in model compounds. An estimate of dynamic correlation effects can be obtained by checking the convergence of state energies with respect to system size i.e. model compound in this instance.

Another group of computational studies focuses on calculating the formation energies of defects in h-BN [78] and argues the probability of formation of a particular defect species under thermal equilibrium. This approach also has important shortcomings; firstly, the standard method of calculation of defect formation energy in 3D materials cannot be applied to charged defects in 2D materials like h-BN. For charged defects, the Coulomb energy arising from the interaction of charges with their periodic images diverges. In calculations, this divergence is removed by introducing a homogeneous counter charge to neutralize the supercell. Converged values can be found in the dilute limit, using a very large supercell. For 2D systems modelled in a 3D cell by introduction of a large vacuum region, however, this approach is problematic as the counter charge gets distributed across the entire cell and is therefore not confined within the material [157]. Ref. [118] has tacked this issue by applying infinite layers of h-BN sheets within the supercell approach and they applied Freysoldt charge correction for charged defective supercells. However, in a few other previous calculations of defect formation energies for h-BN [78,124], this important issue has been ignored. This indeed has been the case for defects in h-BN where an arbitrarily chosen vacuum size results in a wide spread of results for the formation energy [78,124]. In a recent work [122] I have adopted a parameter free approach already applied successfully to h-BN defects [158] to tackle this problem. This approach gives converged ionization energy by extrapolating the asymptotic expression of ionization energy/charge transfer level for a large vacuum size (L_z) back to $L_z = 0$.

Secondly, defects can be under kinetic control rather than being in thermodynamic control i.e. atoms come together during formation of material and bind into a high energy state, but then the barriers to reaction from this are large enough so the defect stays trapped there. Thermodynamic equilibrium then never occurs, e.g. a mixture of H_2 and O_2 gasses. In this case, to use energetics to predict composition, one needs to know all of the reaction intermediates during synthesis. Thus, one cannot exclude a particular defect species based on high formation

energy or vice versa. Indeed the experimentally identified defect species in SiC, InN etc. have high formation energies [159]. I conclude this section by saying that great care must be taken while applying standard DFT approaches perfectly applicable to 3D periodic solids to a 2D system like h-BN, because of different screening in the later. In the next chapter, I describe the computational approaches used in this work with special consideration of the above-described challenges.

Chapter 3 Theoretical methods and Computational details

In this chapter, the computational and theoretical methods used in this thesis are discussed. Firstly, a brief introduction of ab-initio quantum chemistry methods and density functional theory (DFT) is presented.

3.1 Quantum chemistry methods and density functional theory (DFT)

The methods that allow getting the exact answer through some pre-defined route and are derived from first principles quantum mechanics are called ab-initio methods. Ab-initio methods can be categorized into two general classes, i.e., coupled cluster methods e.g. coupled-cluster singles and doubles (CCSD) [127] with perturbation theory corrections for triples excitations (CCSD(T)) [128], related time-dependent approaches such as equations of motion coupled cluster (EOM-CCSD) [129,130] and configuration interaction methods e.g. singles and doubles multi-reference configuration interaction (MRCI) [131], as well as its approximation, complete-active-space self-consistent field (CASSCF) [132] theory with perturbative corrections for singles and doubles excitations (CASPT2) [133].

The wave function for coupled cluster methods is written as an exponential ansatz i.e. $\Psi = e^{T}\Phi_0$, where Φ_0 is the reference wave function and T is the cluster operator acting on Φ_0 and produces a linear combination of Slater determinants. For configuration interaction, methods a linear combination of configuration state functions built from spin orbitals (SO) (complete wavefunction consisting of spatial and spin components) is used i.e. $\Psi = \sum_{I=0} C_I {\Phi_0}_I^{SO}$.

As is apparent from their wave functions, these two types of methods have their own merits and problems in terms of whether they are variational and whether they obey size consistency. Coupled cluster methods in their conventional implementation are not variational while truncated configuration interaction methods are not size consistent and vice versa. Nevertheless, these quantum chemistry methods allow a complete description of a material system and can be made to converge to the exact solution for a given basis set in the limit where all possible configurations are included. An alternative method, which has been applied successfully to systems ranging from the homogeneous electron gas, to atoms, molecules,

solids and clusters is quantum Monte Carlo (QMC). In this method, the Schrödinger equation is transformed to a diffusion equation, which is solved using stochastic methods. These traditional methods in which the wave function is the fundamental descriptor of the system, encounter the curse of rapid growth of computational complexity with system size [160] compared to quantum Monte Carlo method (QMC) e.g. QMC scales as N^2 (N being the relative system size), CCSD scales as N^6 and CCSD(T) as N^7 etc. DFT on the other hand is a reformulation of Schrödinger wave mechanics in terms of the electron density. In principle DFT is exact, but in practice the exact density functional representation of the exchange correlation is not known in analytical form and must be approximated by some empirical functional. Electron correlation is divided into dynamical and non-dynamical (static) correlation. Dynamical correlation is the correlation of the movement of electrons and static correlation is important for systems where the ground state is well described only with more than one (nearly) degenerate determinants. Depending upon the particular functional used, DFT can capture dynamic correlation quite well at a much smaller computational cost compared to ab initio methods. It is for this reason that DFT has been so widely used in electronic structure problems. It is, however, a single configuration method and fails when static correlation becomes important. In the following section, I briefly present the idea of many body problem in quantum mechanics in the context of solids.

3.1.1 Many body problem and quantum mechanics

A physical system can be described by a complete descriptor given by a set of variables that carries all the information about the system and in principle all of it's properties can be determined. In quantum mechanics, such a descriptor is the wavefunction, which carries all the information about the co-ordinates and spin of each particle of the system. For a system consisting of N-particles it's descriptor in Hilbert space $\check{H}_N$ is given by

$$\Psi(\vec{x}) = \Psi(\overrightarrow{r_1}\sigma_1, \overrightarrow{r_2}\sigma_1, \dots\dots, \overrightarrow{r_n}\sigma_n) \qquad (3.1)$$

where

$$\vec{x} = (\vec{x}_1, \vec{x}_2, \dots\dots, \vec{x}_N) \qquad (3.2)$$

gives the space-spin variables of all the particles in the system. The standard model system in physics or chemistry is composed of two types of particles i.e. nuclei and electrons, and the only interaction, which is important between these two types of particles, is either electrostatic interaction or in some cases the magnetic interaction. The behavior of this model system can in principal be described by the Schrödinger wave equation but the only hurdle is what Walter Kohn termed as the exponential wall [161]. To have an idea of the power of this exponential wall consider a simple N_2 molecule consisting of two nuclei and fourteen electrons expressed on a grid of 100 points in each spatial dimension. A wave function of form (3.1) for this simple system is represented by $2^{14} * 100^{3*16} \sim 10^{100}$ complex numbers (for a system of N particles Schrödinger wave equation would have 3N dimensions), which is beyond the capacity of present day computers.

Several approximation however can be made, first one is the adiabatic approximation (a simplification of Born-Oppenheimer approximation), which assumes that electronic and nuclear degrees of freedoms are not coupled based on the large mass differences between these particles and thus allows to significantly simplifying the problem. Another approximation is treating the electrons as non-interacting quasi-particles thus instead of having to represent one wave function in 3N dimensions, one only needs to represent N wave functions in 3-dimensions each. Thus, a dramatic simplification from 10^{100} to 10^7 numbers can be made as a result of making these two approximations. Although the quasi-particle approximation simplifies the problem, the Coulomb interaction between electrons cannot be ignored, so some other form of solution is needed and here comes DFT to our rescue. DFT simplifies the problem by mapping the system of interacting electrons onto a system of non-interacting electron density.

After making the Born-Oppenheimer approximation, a given descriptor of the form (3.1) governed by the Schrödinger wave equation $i\hbar\sigma_t|\Psi\rangle = \hat{H}|\Psi\rangle$ with Hamiltonian

$$\hat{H} = \sum_{J=1}^{N}\left(-\frac{\hbar^2}{2m}\nabla_J^2 + v_{ext}(\vec{r_j})\right) + \frac{1}{2}\sum_{i\neq j}^{N}\frac{e^2}{4\pi\varepsilon_0|\vec{r_i}-\vec{r_j}|} \tag{3.3}$$

can describe the behavior of this system. The first term in equation 3.3 is the kinetic energy of the electrons, second term is the potential energy experienced by the electron while moving in

the external potential of static nuclei, and third term is the potential energy due to the interaction between electrons. Although the Born-Oppenhemier approximation has considerably simplified the problem compared to the original one it still it is too difficult to solve due to the third, non-separable, term.

Several methods exists to reduce equation 3.2 into an approximate but tractable one. A historically very important one is the Hartree-Fock method (HF). It performs reasonably well for atoms and molecules, but is less accurate for solids, as it does not contain dynamic electron correlation. Another one is DFT, which performs very well for both molecules and solids, as it involves dynamic electron correlation effects at about the same computational cost as HF. However, both HF and DFT are single determinant methods and do not include static electron correlation. DFT is based on the theorems of Hohenberg and Kohn. In the next section, I provide a brief description of Hohenberg-Kohn and Kohn-Sham theorems and self-consistent nature of Kohn-Sham scheme.

3.1.2 Hohenberg-Kohn and Kohn-Sham theorems

The central statement of density functional theory is the celebrated Hohenberg and Kohn [162] theorem, which for non-degenerate ground states can be summarized in the following three statements.

- The ground state density $n(r)$ uniquely determines the potential $v(r)$ acting on the electrons and hence all the physical properties of the system.

- The ground state energy E_0 of a system can be obtained from ground state density using the variational principle i.e. the true ground state density minimizes the total energy of the system.

- There exists a universal functional $F[n]$ for all systems such that the energy functional can be expressed as

$$E_{v_0}(n) = F[n] + \int d^3r v_0(r) n(r) \qquad (3.4)$$

The functional $F[n]$ is independent of the potential $v_0(r)$ of a particular system for a given electron-electron interaction. $F[n]$ can be defined formally in the following way

$$F[n] = T[n] + v_{ee}[n] = \langle \Psi[n] | \hat{T} | \Psi[n] \rangle + \langle \Psi[n] \left| \widehat{V_{ee}} \right| \Psi[n] \rangle \qquad (3.5)$$

where T and v_{ee} are the functional for kinetic energy and electron-electron interation, $\Psi[n]$ is that N-electron wavefunction which minimizes the density $n(r)$ w.r. t. the expectation value of $T + v_{ee}$. The explicit density dependence of $F[n]$ remains unknown and hence approximations have to be made. Nevertheless, Hohenberg-Kohn theorem provides the basic theoretical foundation for single particle formulation which allows the calculation of ground state density and hence the ground state energy of system of interacting electrons. The resulting Kohn-Sham equations are at the heart of DFT and have the form of single particle Schrödinger equation.

$$\left[-\frac{\nabla^2}{2} + v_s(r) \right] \varphi_i(r) = \epsilon_i \varphi_i(r) \qquad (3.6)$$

The density $n(r)$ can be computed from *N* single-particle orbitals occupied in the Slater determinant in the following way.

$$n(r) = \sum_i^{occ} |\varphi_i(r)|^2 = \sum_i^{occ} \varphi_i^*(r) \varphi_i(r) \qquad (3.7)$$

The central idea of Kohn-Sham scheme is to construct the single particle potential $v_s(r)$ in a way that matches the density of non-interacting system to the density of interacting system of interest. To this end one can partition $F[n]$ in the following way

$$F[n] = T_s[n] + U[n] + E_{exc}[n] \qquad (3.8)$$

Where $U[n] = \frac{1}{2} \int d^3r \int d^3r' \frac{n(r) n(r')}{|r - r'|}$ is the classical electrostatic energy due to charge distribution $n(r)$ and $E_{exc}[n]$ is the exchange correlation energy formally defined as follows

$$E_{exc}[n] = T[n] + E_{ee}[n] - U[n] - T_s[n] \qquad (3.9)$$

Thus the form of potential entering equation 3.6 is

$$v_s[n](r) = v(r) + \int d^3r' \frac{n(r')}{|r-r'|} + v_{exc}[n](r) \qquad (3.10)$$

where, the exchange correlation potential is defined by

$$v_{exc}[n](r) = \frac{\delta E_{xc}[n]}{\delta n(r)} \qquad (3.11)$$

Since $v_s[n](r)$ depends upon density therefore equations 3.6, 3.7 and 3.11 have to be solved for self-consistent ground state density and this is known as the self-consistent Kohen-sham scheme of DFT, in which an iterative procedure is adopted. An initial density is guessed, Kohn-Sham Hamiltonians are setup with this initial density and Eq. 3.6 is solved for the new density, unless the initial guessed and final densities match. It is worth mentioning here, in the context of this work, that Kohn-Sham theorem is applicable to closed shell wave functions only. However, the lowest state of any other spatial and highest spin symmetry can be calculated by using another theorem called Gunnarsson-Lundqvist [163], which is an extension of Kohn-Sham theorem.

3.1.3 Exchange-Correlational function

The explicit form of exchange correlation potential defined by 3.11 is inexpressible in a general closed analytic form for real systems and some approximation has to be made for this quantity. In this section, I describe some of the common approximations made for this quantity and introduce hybrid functionals that are commonly used. First approximation is the local density approximation (LDA) which postulates that the exchange correlation energy of any system of density $n(r)$ can be constructed by dividing the system into infinitesimally small volumes of constant density each. Each small volume contributes to total exchange-correlation energy by an amount equal to exchange correlation energy of an identical volume filled with uniform electron gas. i.e.

$$E_{xc}^{LDA} = \int n(r)\varepsilon_{XC}(n(r))d^3r \qquad (3.12)$$

In principle, LDA does not perform well for real systems. A natural improvement to this approximation can be made by taking the contribution of exchange correlation energy not only from small infinitesimal volumes but also from neighbouring volumes i.e. by taking into consideration the gradients in electron density in an approximation called generalized gradient approximation (GGA) and is formulated as follows

$$E_{xc}^{GGA} = \int f(n(r), \nabla(n(r))d^3r \qquad (3.13)$$

The fundamental difference between two approximations is that LDA is unique because there is only one definition of $\varepsilon_{XC}(n(r))$, while there are many proposed forms of GGA because there are more than one ways to choose density gradients. One can also feed into a candidate GGA functional, free parameters from a large set of experimental data on atoms and molecules and get good results for a certain class of solids, while worsening it for others or making GGA accurate for a set of physical properties and worsening it for other set. In spite of this GGA has proven to be quite useful in producing accurately the properties of many systems.

Although thousands of functionals have been used in calculations over the last few decades, I will only discuss those that are relevant to this work. One class of GGA's called meta-GGA depend in addition to density and it's gradient on the kinetic energy of Kohn-Sham orbitals as well. Because of this orbital dependence, meta-GGA are also termed as orbital functionals unlike LDA or GGA, which are explicit functionals of electron density only.

$$E_{xc}^{meta-GGA} = \int f(n(r), \nabla(n(r), T(r))d^3r \qquad (3.14)$$

$$\text{Where, } T(r) = \frac{1}{2}\sum_i^{occ}|\nabla\varphi_i(r)|^2$$

The inclusion of extra variables allow for additional flexibility and thus produce accurate results for one class of physical properties without worsening others. Thus, development of orbital functionals or explicit density functionals has been an area of extensive research work. One of the most familiar orbital functional is exact exchange energy functional given by

$$E_x^{E^{XX}} = -\frac{1}{2}\sum_{\sigma}\sum_{i,j}^{OCC}\int\int \frac{\varphi_{i\sigma}(r)\varphi_{i\sigma}^*(r') - \varphi_{j\sigma}(r')\varphi_{j\sigma}^*(r)}{|r-r'|} d^3r d^3r' \qquad (3.15)$$

The exact exchange energy functional (3.14) is similar to Hartree-fock functional if one neglects correlation. The only difference is that in exchange DFT methods the Kohn-Sham orbitals are used rather than Hartree-Fock orbitals. The result is that exact exchange energy spectra are usually closer to the experiment than Hartree-Fock spectra. Therefore, DFT is a much better starting point to include correlation effects than Hartree-Fock.

A new class of approximation to exchange-correlation energy are the hybrid functionals, which include a fraction of exact exchange with GGA exchange

$$E_x^{HYB} = aE_x^{EXX}[n] + (1-a)\,E_x^{GGA}[n] \qquad (3.16)$$

Where, 'a' is the empirical mixing parameter. One such hybrid functional which is widely employed for studying the properties of periodic solids in general and for calculation of excited state properties of defects in crystals in particular is HSE06 [164,165], for which a=0.25. HSE06 has been implemented in many DFT codes e.g. VASP [166,167]. In this thesis, I benchmark the HSE06 results with quantum chemistry approaches and identify the inaccuracies in this otherwise well trusted functional for defect calculations.

Another long-range corrected hybrid functional CAM-B3LYP [168,169] which comprises of 0.19 Hartree–Fock (HF) plus 0.81 Becke 1988 (B88) exchange interaction at short-range, and 0.65 HF plus 0.35 B88 at long-range. This functional is routinely used for molecules in quantum chemistry. In this thesis, I propose on the basis of my calculations on model compound for defect systems in h-BN that CAM-B3LYP suffer less seemingly random anomalies and are generally much more reliable compared to HSE06 when applied to defect states. As the only methods containing correction for the asymptotic potential error should be applied to defect sites owing to their likelihood of involving charge-transfer spectroscopy, practical software limitations may limit current applications in periodic systems to uncorrected functionals like HSE06. The implementation of range-corrected hybrid functionals like CAM-B3LYP into solid-state DFT codes is therefore highly desirable.

3.2 Density functional theory for excited states

The extended Kohn-Sham scheme of DFT is applicable to the lowest state of any given spatial or spin symmetry. For excited state properties many new versions of DFT have been proposed e.g. ΔSCF method [170,171], constrained DFT (CDFT) [172], time dependent DFT (TDDFT) [173] etc. In the following sections, I will very briefly describe TDDFT and ΔSCF versions of DFT since these versions are used frequently in the present work.

3.2.1 Time-dependent density functional theory (TDDFT)

The central statement of TDDFT is that for if Ψ_0 is the ground state of a system with Hamiltonian $\hat{H}$ at some initial time t_0 than there is one to one correspondence between ground state density $n(r,t)$ and external potential $v(r,t)$ at some later time t. In the framework of TDDFT the single particle like Kohn-Sham equation (3.6) can be written in analogy with the time dependent Schrödinger wave equation i.e.

$$\left[-\frac{\nabla^2}{2} + v_s(r,t)\right]\varphi_i(r,t) = i\frac{\partial}{\partial t}\varphi_i(r,t) \qquad (3.17)$$

Hence the expression of density, Kohn-Sham potential and exchange-correlation can be obtained by inserting an additional variable of time in equations 3.6, 3.7 and 3.11 respectively. In this work PBE, HSE06 and CAM-B3LYP exchange correlation functionals are used within TDDFT scheme.

3.2.2 ΔSCF method

Constrained DFT (CDFT) and ΔSCF method are two slightly different approaches and can be considered as small extensions of conventional DFT. In CDFT an additional potential (to Kohn-Sham) is introduced and varied until a particular constraint on the electron is fulfilled. In ΔSCF method, the position of electron is controlled by controlling the occupations of Kohn-Sham orbitals when system reaches self-consistency. For CDFT the expression for electron density can be written [172] in analogy to expression for density (3.6) used in conventional DFT i.e.

$$n(r) = \sum_i^N \varphi_i^*(r)\varphi_i(r) + \sum_i^N \varphi_a^*(r)\varphi_a(r) \qquad (3.18)$$

Where, $\varphi_a(r)$ is the Kohn-Sham orbital corresponding to LUMO from the ground state calculations whose occupancy is being fixed. One can clearly see that the Kohn-Sham orbitals found when solving these modified Kohn-Sham equation will differ from the ordinary DFT because of the change in the Hamiltonian as a result of change in density, effectively raising the total energy of the system and hence giving in return the excited state energy corresponding to that particular occupancy.

3.3 Group theory

Group theory, which describes the abstract mathematics of symmetry operations, is a powerful tool that helps us to obtain fundamentally important information from a physical system e.g. allowed and forbidden transitions, inter-system crossings, spin-orbit couplings, spin-spin interaction etc. without doing any rigorous calculations i.e. purely from symmetry considerations [174]. Since historically, group theoretical analysis has really been useful in exploring the properties of N_V^{-1} centre in diamond [125], therefore I apply this tool to predict the optical cycle of various defects in this thesis. All of the symmetry operations that apply to a molecule or ion or a defect constitute its point group. It is the point group to which the molecule belongs that designates its symmetry. A multiplication table generally contains the result of two symmetry operations and each point group has its own multiplication (character) table. By convention, the rows of a character table correspond to irreducible group representations, and columns correspond to conjugacy classes of group elements. Since the important defects e.g. V_NN_B, V_NC_B and V_BC_N studied in this thesis, transform according to C_{2v} point group symmetry. Therefore, I give below the character table of C_{2v} point group.

Table 3.1 Character table for C_{2v} point group. The two rightmost columns show the functions which transform under a particular irreducible representation. Here, (x, y, z) stand for a polar vector, while (R_x,R_y,R_z) for an axial vector.

C_{2v}	E	C_2	σ_V	σ_V'		
A_1	1	1	1	1	z	x^2,y^2,z^2
A_2	1	1	-1	-1	R_z	xy
B_1	1	-1	1	-1	x, R_y	xz
B_2	1	-1	-1	1	y,R_x	xz

Using the standard axis conventions for planar molecules, the irreducible representations (IR's) of the C_{2v} point group are a_1 and b_2 (of σ type) and b_1 and a_2 (of π type) as shown in Table 3.1.

In C_{2v} point group the electric dipole transforms either as a_1, b_1 or b_2, while each of magnetic sublevels for triplet state transform as a_2, b_1 and b_2. In C_{2v} point group only those transition between states (say 'X' and 'Y') are allowed for which the product $X * \begin{pmatrix} a_1 \\ b_1 \\ b_2 \end{pmatrix} * Y$ transforms as totally symmetric IR i.e A_1.

3.4 Computational parameters

In this section, I present some of the general computational parameters used in this work, more specific parameters and detail of theory behind different calculations would come later in chapters wherever necessary. I surveyed a range of likely defects in h-BN and calculated their ground and excited state (zero phonon energies) properties using PBE [175] version of generalized-gradient approximation (GGA) as is implemented in SIESTA [176,177]. Calculations were performed for periodically replicated defects in 2-D h-BN nano flakes using DFT. For calculation of the total energy, electronic structure and ground state geometry (from a PBE survey) of defects selected according to the criteria in Section 2.4, I used Version 5.3.3 of the Vienna Ab Initio Simulation Package (VASP) [166,167]. For accurate calculation of electron spin density close to the nuclei, the projector augmented wave method (PAW) [178,179], was applied together with a plane wave basis set. I utilized the standard PAW-projectors provided by the VASP package. Pristine single-layer h-BN was first geometrically optimized using the conventional unit cell and a 21×21×1 Monkhorst-Pack reciprocal space grid. A large vacuum region of 30 Å width was used to separate a single layer of h-BN from its periodic images and to ensure that the interactions between periodic images are negligible. The optimized bond length of pristine h-BN is 1.452 Å. All the defects were then realized in a 98 atom supercell and allowed to fully relax using a plane wave cut-off of 350 eV for a maximum force of 0.01 eVÅ^{-1}. I have used the non-local HSE06 functional [164,165] as an approximation to exchange and correlation. Optimized geometries from VASP were used to calculate the wave function coefficients of defect states. Zero-field splitting tensors are evaluated using the method described in Ref. [180]. For the calculation of the spin-spin contribution to the zero-field tensor, a higher cut-off energy of 600 eV and lower force tolerance of 10^{-4} eVÅ^{-1} were used. The normal modes were calculated using an energy cut off

500 eV. Excited state energies in VASP are calculated using constrained ΔSCF method [181] using the "FERDO" and "FERWE" commands. This procedure produces spin-contaminated states that have no first-principles physical interpretation (for states not described by a single Slater determinant and where the calculation breaks symmetry, i.e. spin polarized). The methods developed to map the resulting calculated properties onto physical observables are described in detail later. New software was developed to control the VASP calculations and hence obtain converged results for arbitrary excited states. Huang Rhys(HR) factor for the shortlisting of the defects was calculated using ΔSCF method. HR factor reflect the structural changes in transition from HOMO to LUMO or to conduction bands; the quantity denoted by ΔQ given by equation 3.19 is a good indicator of how much structural re-organisation occurs upon excitation:

$$\Delta Q = \sum_{ai} m_a^{1/2} \left(R_{e,ai} - R_{g,ai}\right) \qquad (3.19)$$

Where 'a' enumerates the atoms, i = x, y, z, m_a is the atomic mass of species a, and $R_{g/e,ai}$ is the position of atom 'a' in the ground/excited state, respectively.

In order to evaluate the performance of HSE06 for calculations of defect excited states, I have undertaken ab initio calculations using the CCSD [127], CCSD(T) [128], EOM-CCSD [129,130], CASPT2 [133], and MRCI [131] methods, performed for a model compound (shown in Fig. 1b) cut from a 98 atom supercell containing one ring of h-BN atoms surrounding the defect. Calculations were performed using MOLPRO [182] and Gaussian16 [183] packages. Additional DFT calculations using the CAM-B3LYP functional [168,169], an asymptotically corrected functional that was the first density functional shown to be able to treat charge-transfer transitions correctly [41,42], have also been performed on the model compound.

The PL line shape for selected transitions were calculated in curvilinear coordinates using the DUSHIN [184] code based on the vibrational analysis obtained from VASP at the Γ-point of the vibrational Brillouin zone; this analysis included explicit projection-out of the three frequencies associated with macroscopic translation of the crystal, providing an improved description of perceived critical low-frequency motions and detection of possible imaginary frequencies associated with transition-state structures.

Chapter 4 A survey of defects in h-BN

4.1 Potential defect in h-BN

In order to identify the origin of ≈ 2 eV emission one needs to first survey the likely defects causing such emission. I performed a survey of many possible defects in h-BN. For sake of brevity in this chapter, I present the theoretical analysis of 35 most likely defects in h-BN, using density functional theory (DFT). In particular, I focus on potential quantum emission candidate defects including intrinsic e.g. vacancies and anti-sites and extrinsic defects e.g. oxygen (O), hydrogen (H), carbon (C), silicon (Si), sulphur (S), fluorine (F) and phosphorus (P) defects. I chose the defects based on the most likely impurities during the h-BN growth and processing. For instance, it is known that intrinsic defects like nitrogen (N_v) and boron (B_v) vacancies exist and act as paramagnetic centres in h-BN [108], carbon and oxygen are readily incorporated into h-BN during growth, while annealing of h-BN is performed on a silicon substrate [113], which may cause silicon diffusion into the h-BN [113]. Annealing h-BN samples in air is shown to increase the number of emitters, which suggests that oxygen related defects are important as potential emitters [185] as well.

The atomic structures of the 35 considered h-BN defects are displayed in Fig. 4.1. I consider several groups of defects: Si/C-defects, Stone–Wales defects (labelled SWC_N), C-based defects, O-based defects, native defects, S-based defects, and complex defects, as well as a few other defects. I have applied the standard defect nomenclature when possible and adhere to this throughout the thesis. For all of these 35 defects, the imaginary component of the dielectric function in Random Phase Approximation (RPA) is calculated, using an optical mesh of 21 x 21 x 1 (generating 147 x 147 x 1 K-points across Brillouin zone (BZ)) and an optical broadening of 0.06 eV with different polarization of the optical vector, to check for linear polarization of the defects (an experimental criterion [11]). Within RPA dielectric function is calculated using the simplest approach based on the dipolar transition matrix elements between different Eigen functions of the self-consistent Hamiltonian in the momentum space. I also calculated the band structure in the ground state (GS) in order to identify promising defects with a HOMO-LUMO gap of around 2 eV (as per experimental observations [11]). Although in these calculations (for a crude survey of defects in h-BN), the

excited states are not relaxed and hence the estimate of defect transition energy is not completely reliable due to the neglect of the relaxation energy. However, one still can have a rough estimate of transition energies as PBE is well known to underestimate the energies and thus underestimation of energy by PBE functional and the neglect of relaxation energy almost cancel each other [11].

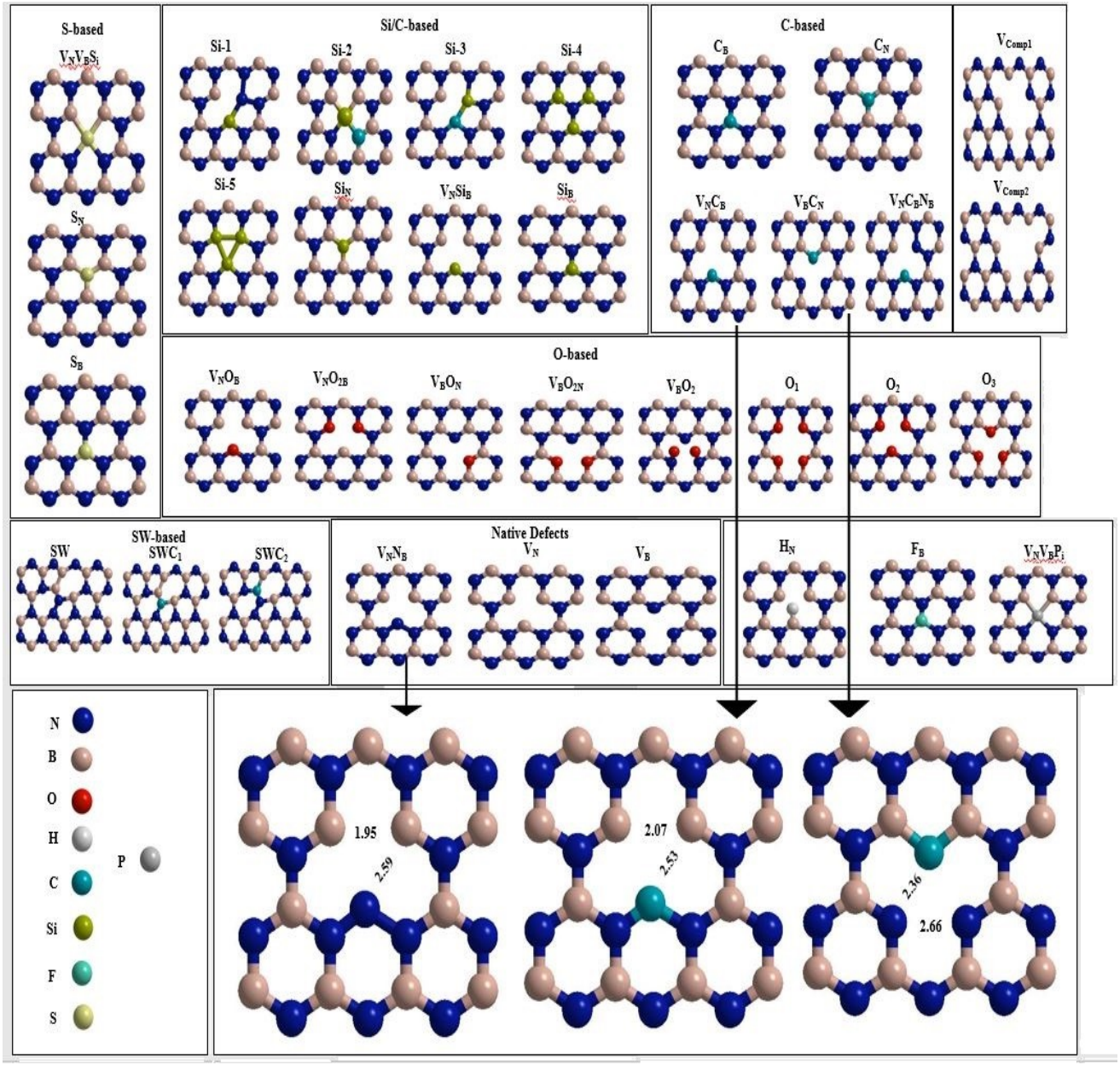

Figure 4.1 Atomic structures of the defects in Table 4.1. SWX denotes Stone–Wales defects, and VCompX denotes complex vacancy defects.

In Table 4.1, the results of the present ground state calculations for these defects are displayed. The values of $E_T^{\uparrow\downarrow}$ correspond to characteristic peaks in the imaginary dielectric function (effectively, peaks in the optical absorption spectrum) for the spin-up and spin-down channels, respectively. One can see from Table 4.1 that although many defects have $E_T^{\uparrow\downarrow} \approx 2$ eV, However some of the defects have bulk bands and are not linearly polarized either.

Table 4.1 The calculated electronic transition energy of the spin-up defect state, $E_T^{\uparrow}$, the spin-down defect state, $E_T^{\downarrow}$, whether the transition is from/to the bulk band, and whether the transition is optically allowed (energy reported wherever transition is allowed), and the polarization of the defects displayed in Fig. 2(a). I determined whether a defect belongs to the bulk bands by inspecting the defect band structure and observing the proximity of the defect level to the conduction or valence band, as well as the defect level dispersion. The polarization of the defect is determined by the optical absorption spectrum of the defect along different polarization axes; an absorption peak that exists in one polarization axis but not in the others is an optically polarized defect. All energies are reported in units of eV.

Defects	$E_T^{\uparrow}$	Bulk bands?	$E_T^{\downarrow}$	Bulk bands?	Polarized
C_B	-		-		
C_N	-		-		
V_BC_N	1.93	No	2.67		Yes
V_NC_B	1.44	No	-		Yes
$V_NC_BN_B$	1.00	No	1.00	No	Yes
V_NV_BPi	3.41		-		
F_B	2.00	No	2.00	No	No
S_B	2.26	No	-		Yes
$V_NV_BS_i$	2.72	No	2.72	No	Yes
S_N	-		-		
V_NN_B	2.02	No	-		Yes
V_B	-		2.31	Yes	
V_N	2.08	No	-		No
V_BO_N	-		-		
V_BO_{2N}	-		-		
V_NO_B	-		-		
V_NO_{2B}	2.39	No	-		Yes
V_BO_2	2.00	Yes	0.87,2.18		Yes
O-1	-		-		
O-2	-		-		
O-3	-		-		
SW	3.55	No	3.55		
SWC_N	2.94	No	-		Yes
SWC_B	2.02	Yes	-		No
V_{Comp1}	-		1.67	Yes	
V_{Comp2}	-		-		
Si_B	-		-		
Si_BV_N	3.28	No	3.28	No	Yes
Si_N	-		-		
Si-1	2.21		2.21		
Si-2	2.20		-		
Si-3	1.83	No	1.99	No	
Si-4	0.42,0.96	No	-		
Si-5	3.44,3.75		-		
HN	1.75, 2.97	No	-		

To select potential emitters, I have applied four criteria (as described above), based on experimental observations, and in order to narrow down the list of potential defects shown in Table 4.1 i.e.

1. The stability of the emitters against high temperature annealing [99] imply that the positions of the defect levels are within the bandgap.

2. The observed emitters are in-plane polarized [11] as discussed earlier.

3. E_{ZPL} reported in different experimental papers for defects in h-BN is between 1.3 eV and 2.2 eV [11,28,32,75,84,86,99,119,120].

4. In addition, since the observed emission from h-BN emitters is sharp with negligible phonon side band, meaning that Huang-Rhys (HR) factor (Eq. 3.19) for these defects is small.

I then relaxed the excited states after fixing the occupancies and calculated the adiabatic excitation energies i.e. ZPL for a few defects. I present the results of shortlisted (as per criteria (1)&(2)) defects in Table 4.2. along with calculated values of ΔQ and energies of ZPL calculated using ΔSCF approach. In the defects in Table 4.2, $E_T^{\uparrow\downarrow}$ lies within the bandgap and criteria (1) and (2) are satisfied. Then, applying criteria (3) and (4) on the defects in Table 4.2, I found that there are three defect structures that could potentially emit single photons i.e. the N-anti-site defect (N_BV_N) (ΔQ = 0.66 $amu^{1/2}$Å), the V_NO_{2B} defect (ΔQ = 0.93 $amu^{1/2}$Å) and the V_NC_B defect for 1^3B_1 to 2^3B_1 transition (ΔQ = 0.53 $amu^{1/2}$Å). The calculations using VASP gave values for E_{ZPL} that are very close to the values obtained using SIESTA: 2.01 eV, 1.85 eV and 1.33 eV for the V_NN_B, V_NO_{2B} and V_NC_B defects, respectively. The S_B, $V_NC_BN_B$, $V_NV_BS_i$, Si-1 and Si-2 defects, although they satisfy the above four criteria, undergo large structural changes as quantified by ΔQ, as defined in eqn. (4.1) (for these defects, ΔQ = 4.18, 4.91, 1.45, 9.91 and 5.00 $amu^{1/2}$Å, respectively). Such large values for ΔQ would correspond to large HR values. The atomic structures of V_NN_B, V_NC_B and V_BC_N defects are zoomed out in Fig. 4.1. The excited state atomic structures for all these defects are only slightly changed, and therefore I do not display them. For N_BV_N, the main difference between the atomic structure of the excited and the ground states is that the B–B bond distance drops by 7.7%; for V_BC_N,

the N–C distance stretches by 6.3%; for V_NC_B (1^3B_1 to 2^3B_1 transition), which undergoes the least atomic displacement, the C–B distance stretches by 3.6%.

Table 4.2 The calculated ZPL energy E_{ZPL} (in eV) and the ΔQ in $amu^{1/2}$Å for the defects (defined in eqn. (4.1))

Defect	ZPL(spin-up) (eV)	ΔQ ($amu^{1/2}$Å)
$V_NV_BS_i$	1.94	1.45
S_B	1.26	4.18
V_NSi_B	0.94	4.00
V_NO_{2B}	1.90	0.93
SWC_N	2.70	0.30
V_BC_N	1.11	1.86
$V_NC_B^*$	1.39	0.53
V_NN_B	2.12	0.66
Si-1	1.86	9.91
Si-2	2.03	5.00
Si-3	0.62	5.02
Si-5	3.81	5.03
$C_BN_BV_N$	2.16	4.91

*The ZPL correpondes to transition between triplet manifold, the true ground state is singlet as is studied in detail in later chapters.

A word on the possiblity of the out of plane distortion of defects V_NN_B and V_NC_B is in order. The defects V_NN_B and V_NC_B were thought to have planar C_{2v} symmetry in agreement with previous calculations [44,73,74,78,118,124]. Although recently a new non-planar ground state of these defects has been predicted [123] with a lower C_1 symmetry. To confirm I have calculated the energy differences between planar and non-planar structures of V_NN_B and V_NC_B. For V_NN_B the non-planar C_1 structure is favoured by only 0.05 eV, while for V_NC_B C_1 structure is lower in energy by 0.4 eV for singlet ground state, while for triplet state the planar structure is lower in energy. Moreover, I have calculated using the computational parameters described earlier the depth of the associated double-well (with details to come in later chapters). In both cases, the absorption spectra can be broadened by the out of plane distortion. However, because of the difficulty in assessing reliability of calculations to determine energy difference between planar and non-planar configuration, I only consider planar geometries. Therefore, I stick with the planar structure thruoghout the rest of this thesis. All the defects in Table 4.2 have either a singlet or a doublet ground state. The only defects with a triplet ground state is V_BC_N and is exploitable for quantum computation. The defects V_NN_B and V_NC_B, for satisfying the criteria's for possible emitters and having small HR factors and the defect V_BC_N having high-spin ground state, are of interest to us and would be the focus of the thesis from now on.

Since the basic reasoning behind the suggestion [186] that defects like V_NN_B, V_NC_B and V_BC_N could be present in h-BN is that impurity atoms will be present in the growth medium, and that impurity and vacancy defects naturally occur and are likely to be correlated. The formation energetics for neutral and charged defect species is important to study, therefore. In the next section, I focus on the formation energetics, thermodynamic and optical transition levels for V_NN_B, V_NC_B and V_BC_N.

4.2 Thermodynamic charge transition levels and optical transition levels for V_NN_B, V_NC_B and V_BC_N.

The theoretical studies intended to identify the origin of emission from h-BN so far have focused on neutral defects [82,186,187]. Consideration of charge states is however, important as they can become stable as the Fermi energy shifts due to doping (intentional or native) in the surrounding lattice. As the Fermi level is raised, defect-induced states within the band gap become filled with electrons and vice versa. In order to check the stability of charge states of V_NN_B, V_NC_B and V_BC_N defects, I have calculated the formation energies and charge transition levels (CTL's) (energies required to oxidize or reduce the defect relative to the Fermi energy of h-BN).

A word on why the defect formation energy is not used as selection criteria in this thesis for most probable emitters in h-BN is in order. Indeed previously high value of absolute formation energy of different defects e.g. V_NN_B (~8 eV) is used to exclude the possibility of occurrence of that species in h-BN [118]. Here I briefly highlight the limitation of this approach. Defects are off course high-energy species however, growth of h-BN and defect formation is not under thermodynamic control but is instead controlled by the kinetics of atom deposition. Thus, the atoms come together during formation and may bind into a high-energy state, but then the barriers to reaction from this may be large enough so the defect stays trapped. Thermodynamic equilibrium then never occurs, e.g. as in a mixture of H_2 and O_2 gasses. In this case, to use energetics to predict composition, one needs to know all of the reaction intermediates during synthesis. Indeed the experimentally identified defect species in SiC, InN etc. all have high formation energies [159]. Even in materials formed by van der Waals heterostructures, kinetically trapped products can dominate, even affording some properties

that mimic equilibrium [188]. Therefore, I argue that mere calculation of absolute formation energy cannot determine the probability of occurrence of V_NN_B, V_NC_B and V_BC_N in h-BN as previously claimed [118]. Therefore, I do not use formation energy as a criteria for predicting the likelihood of a particular defect species in h-BN in this thesis.

Nevertheless the calculation of formation energy and charge transition levels can give useful information about the nature of the defects e.g. whether it is a compensating or recombination center. One should however be careful while applying the standard method of calculation of formation energy for 3D system to defects in 2D systems like h-BN. For charged defects the Coulomb energy due to the interaction of charges with periodic images diverge. In calculations, this divergence is removed by introducing a homogeneous counter charge for 3D systems to neutralize the supercell. Converged values can be found in the dilute limit, using a very large supercell. For 2D systems modelled in a 3D cell by introduction of a large vacuum region, however, this approach is problematic as the counter charge gets distributed across the entire cell and is therefore not confined within the material [157]. In previous calculations of defect formation energies for h-BN [78,118,124], this important issue has been ignored, and an arbitrarily chosen vacuum size leads to errors in values of the charge transition levels or ionization energies. Wang et al., [157] developed an extrapolation approach to overcome this problem and applied it to the calculation of ionization energies of a few native defects in h-BN. In this thesis, I have used the same parameter free approach [158] to overcome this issue of divergence of Coulomb energy with vacuum size and converged charged transition levels (CTL) are obtained by an extrapolation of the asymptotic CTL's expression at large L_Z (with a fixed lateral area S) back to the value at $L_Z = 0$. This approach has previously predicted the formation energy of point defects in h-BN very accurately [158].

While for a neutral defect, the definition of formation energy under the Jellium approximation follows directly from the energy difference between the investigated system and the components in their reference state. Defect formation energies under different charged states and transition levels (thermodynamic and optical) are calculated through the following well established formulism for bulk materials [189].

$$\nabla E(\alpha, q) = E(\alpha, q) - E(host) + \sum n_i \mu_i + q(E_{vbm} + E_F) + E_{corr} \qquad (4.2)$$

where, $\nabla E(\alpha, q)$ is for formation energy of the defect α with net charge q, $E(\alpha, q)$ and $E(host)$ are the total energies of the defect and pristine supercell, respectively. μ_i is the chemical potential of the *i*th species, n_i the number of defects in the supercell, where n_i is negative for number of atoms added to supercell and positive vice versa. In Eq. 4.2 E_F is the Fermi energy relative to the energy at the valence band maxima (E_{vbm}) in the defect free system and corresponds to the energy needed to remove (add) an electron from (to) valence band maxima to (from) a Fermi reservoir. In order to realize different doping conditions, E_F is varied from the VBM to the conduction band minima (CBM), of the defect supercell. The last term of Eq. 4.2 i.e. E_{corr}, has been added in order to cancel the fictitious interactions between the periodic images of defects, which may become significantly large for charged defects [190]. In order to simulate different experimental h-BN growth conditions defect formation energies have been calculated under N-rich conditions, as it is possible that N_2 exists even under typical vacuum conditions during h-BN synthesis.

In general, the defect formation energy $\nabla E(\alpha, q)$ is a function of $E_{vbm} + E_F$. This is owing to the fact that the energy needed to form a positively charged defect (donor) is lower if E_F is close to VBM, as the ejected electrons from defect site has to join electron reservoir whose energy is E_F, while, on the contrary, energy needed to form a negatively charged defect (accepter) is lower if E_F is close to the CBM. Most point defects can be stable in several different charge states, depending on the position of the Fermi level. The stable charge state of the defect is the one with lower formation energy. As the Fermi level is raised; defect-induced states within the band gap become filled with electrons. The Fermi level positions where a transition from one charge state to another occurs is technically referred to as "thermodynamic charged transition levels" given by the following equation,

$$E_{q/q'}(L_X, L_Y, L_Z) = \frac{E^f(q; E_F = 0) - E^f(q'; E_F = 0)}{q' - q} \qquad (4.3)$$

where $E^f(q; E_F = 0)$ and $E^f(q'; E_F = 0)$ represent the formation energy of the q and q' charge states when Fermi level is at 0 eV. These thermodynamic transition levels correspond to the Fermi-level positions where the formation energies of two charge states of a defect are

equal. Due to divergence of E_{corr} with 'L_Z', the formation energy of charged defects diverges and hence the CTL's diverge too. However, a converged value of CTL's is obtained by plotting the quantity $\overline{E_{q/q'}}$ given by the expression

$$\overline{E_{q/q'}} = E_{q/q'}(L_X, L_Y, L_Z) - \frac{\alpha}{\sqrt{L_X \times L_Y}} \qquad (4.4)$$

against the vacuum size and finding the intercept at $L_Z = 0$, as shown in Fig. 4.2 for the $V_N N_B$, $V_N C_B$ and $V_B C_N$ defects. In Eq. 4.4 'α' is a defect-specific Madelung constant. The quantity "$\frac{\alpha}{\sqrt{L_X \times L_Y}}$" remains somewhat constant with different lateral sizes. The converged values of CTL's, obtained by extrapolating the asymptotic function of $\overline{E_{q/q'}}$ at large L_Z and finite $L_X \times L_Y$ back to the $L_Z = 0$ for $V_N N_B$, $V_N C_B$ and $V_B C_N$, are listed in Table 4.3.

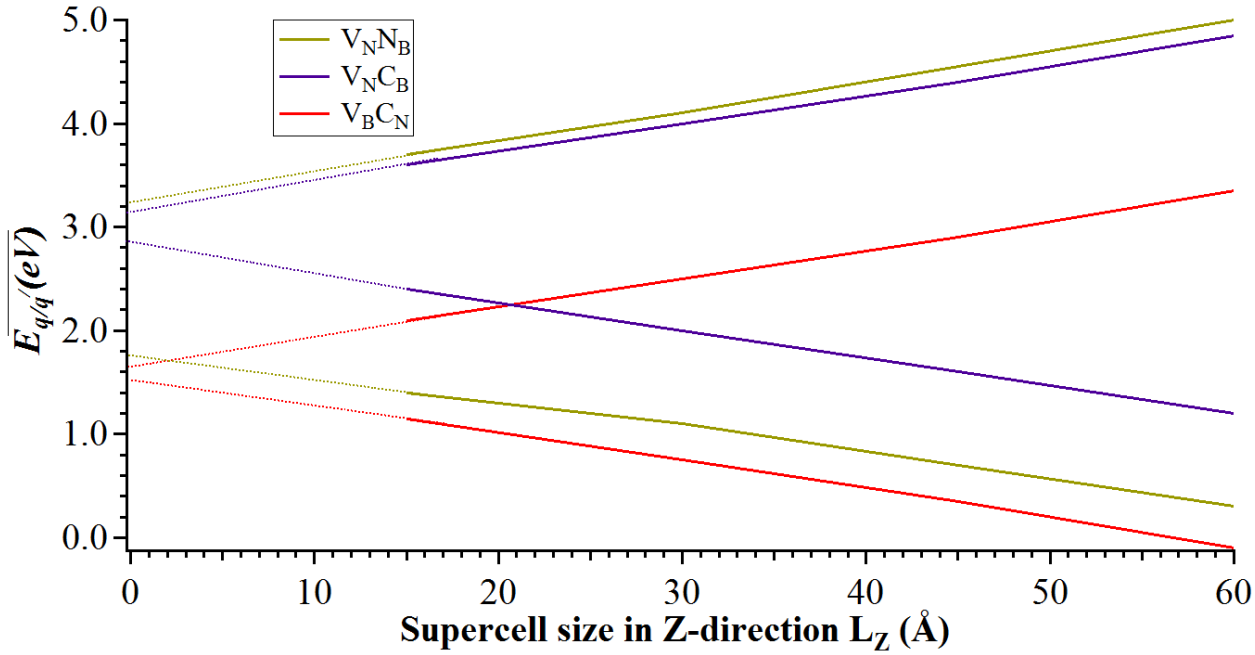

Figure 4.2 $\overline{E_{q/q'}}$ as a function of vacuum size L_Z.

The optical transition energies (either in absorption or emission processes) differ from the thermodynamic transition level by the Franck-Condon (FC) shift or E_{rel} as shown in Fig. 4.3. The FC shift can be approximated by the energy difference between a charged defect in its equilibrium configuration and the same defect when placed in the equilibrium configuration of an excited charge state. The optical transition levels here, refer to the photoelectron process in which light is absorbed and electron ejected into the conduction band, and should not be

confused with the standard defect absorption and emission processes as presented in the later chapters. These transition levels calculated using HSE06 are listed in Table 4.3.

Table 4.3 Thermodynamic transition levels and Optical transition levels of V_NN_B, V_NC_B and V_BC_N calculated at HSE06 levels.

Defect	Transition(q/q')	$E^{Therm.}(q/q')$	$E^{Opt.Absorb.}(q/q')$	$E^{rel.}$	$E^{Opt.\ Emi.}(q/q')$	$E^{rel.}$
V_NC_B	+1/0	2.82	3.38	0.56	2.17	0.65
	0/-1	3.18	3.85	0.67	2.87	0.31
V_NN_B	+1/0	1.80	2.12	0.32	1.28	0.52
	0/-1	3.23	3.45	0.22	2.95	0.28
V_BC_N	+1/0	1.55	2.12	0.57	0.76	0.79
	0/-1	1.64	2.41	0.77	0.88	0.76

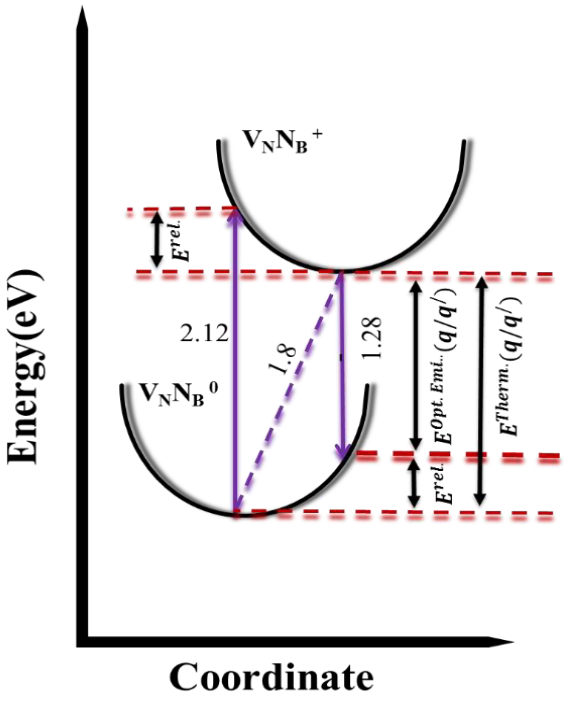

Figure 4.3 Configuration co-ordinate diagram showing transition involving capture of a hole (ejection of an electron) by V_NN_B.

Many of our CTL's differ from previous calculations [118] as they have used used different charged correction scheme as discussed in chapter 2. One can note from Table 4.3 many of CTL'S lie in the energy range of interest e.g. the existence of (+1/0) thermodynamic transition level at 1.8 eV (Fig. 4.3) makes it a potential candidate for observed (˜2 eV) emission. It can be seen from Fig. 4.3 that $V_NN_B^{+1}$ charge states become stable when the Fermi levels

moves closer to the valence band. Thus V_NN_B defect acts as a shallow donor in h-BN, therefore the level structure of V_NN_B defect in '-1' and '+1' charge states is studied in detail in this thesis (later chapters).

In the coming chapters I investigate in detail the defects V_NN_B (in neutral, +1 and -1 charge states) and V_NC_B in neutral charge state for satisfying the criteria's for possible emitters and having small HR factors and the defect V_BC_N for having a triplet ground state. Since a standard method of defect identification is the comparison of calculated hyperfine coupling constants with experimental EPR data, in the next chapter, I present the calculations for hyperfine coupling (HF) constants for V_NN_B, V_NC_B, V_BC_N and some other important defects and make comparisons with available experimental EPR data. Since only a few experimental EPR studies have been reported for h-BN defects. In the next chapters I will also consider the defects which conform to the models reported in the experimental literature and calculate the HF constants for the sake of comparison. Therefore, chapter 5 will serve the purpose of proof of concept and my calculations will fill important gaps in scientific literature and identify the defect species. Since there is no available experimental data for our shortlisted defects i.e. V_NN_B, V_NC_B, V_BC_N, our calculations provide useful theoretical data which can be compared with any possible future experiments.

Chapter 5 Hyperfine Interaction

As discussed earlier, two types of paramagnetic centres have been identified in h-BN: (i) three-boron centres (TBC), in which an unpaired electron interacts with three equivalent boron (B^{11}) nuclei, producing 10-line EPR spectra, and (ii) one-boron centres (OBC), in which oxidative damage at the centre forces the unpaired electron to interact with only a single B^{11}, producing 4-line EPR spectra. The TBC can be deliberately produced either by irradiation [109-111] or by carbon doping [113], but controllable h-BN oxidation to produce OBCs has not yet been achieved. Of particular interest is that carbon-doped centres can give rise to intense photoluminescence [115,116]. Although speculations based on EPR studies have been made about the form of the TBC and OBC centres [109-114], their exact nature remains uncertain.

A-priori calculations using DFT can provide useful tools for the interpretation of EPR data such as observed hyperfine tensors. Indeed, such calculations have been helpful in the identification of point defects in different semiconductors by comparing the experimental and calculated hyperfine constants [100-104].

To the best of my knowledge, there is no comprehensive theoretical study on the hyperfine tensors of defects in h-BN and the prospects for their exploitation in quantum computation. In this chapter, I consider detailed models of the TBC and OBC defects in h-BN, as well as proposing many new defect centres, particularly defects involving introduced carbon impurity atoms. Key known properties of the TBC and OBC defects are reproduced including details of their doublet ground states. Various carbon-related anti-site defects are also considered in which a nitrogen or boron vacancy is accompanied by a neighbouring carbon-atom and/or silicon-atom substitution. In particular, defects with possible ground state conformers of triplet character are searched for, a desirable feature exploitable for quantum computation.

In the following chapter's I will combine group-theoretical analysis to guide how such applications could develop, suggesting new directions for experimental studies for h-BN defects. These results combined with an analyses of PL properties of h-BN defects would allow focus on possible quantum qubit applications.

All the calculations presented in the previous chapter involved defects realized in a 98 atom supercell. However, for the calculation of hyperfine coupling constants I embedded these

optimized supercells in 10x10x1 (136 atoms) supercells using a similar method as described in Ref. [191] for minimizing the computational cost for large calculations and to ensure no interaction in planer directions for the calculation of hyperfine coupling (HF) constants. An increased plane-wave cut-off of 500 eV was used, which was sufficient to obtain a converged spin density and HF coupling constants (A_{xx}, A_{yy}, A_{zz}), where A_{xx}, A_{yy}, A_{zz} are the principle values of the HF coupling tensor. For these supercells, the Γ-point sampling of the first Brillouin zone sufficed. I have used the non-local Heyd-Scuseria-Ernzerh of hybrid functional (HSE06) [164,165], also by taking into account the contribution of the spin polarization of the core electrons to the Fermi-contact term. This has been shown to produce accurate results for HF tensor calculation for point defects in semiconductors [101].

I now present the calculated hyperfine coupling tensor and PL data of various defects in h-BN to make comparisons with the available experimental data. Key results are summarised in Table 5.1 while expanded results are given in Appendix Table 0.I.

Table 5.1 The average principle values of the HF coupling tensor $(A_{xx}+A_{yy}+A_{zz})/3$, in MHz, calculated without (with) core contribution, listing the atoms with dominant spin polarization, for various ground-state (GS) defects in h-BN, with as well as the nature of a related feasible PL state and its transition energy $h\nu$. The Isotope B^{11} and N^{14} have been used in this study.

Defect	Symm.	GS		PL		$h\nu$ (eV)	Atoms	$(A_{xx}+A_{yy}+A_{zz})/3$
		Symm.	Occupancy[h]	Symm.	Occupancy[h]			
V_N	D_{3h}	$^2A_2''$	$(a_2'')^1(e')^0$	$^2E'$	$(a_2'')^0(e')^1$	3.15	B_1-B_3	32(22)[b]
V_N^{-1}	D_{3h}	$^1A_1'$	$(a_1'')^2(a_2'')^2$		-	-	-	-
C_N	D_{3h}	$^2A_1''$	$(a_1'')^1$		-	-	B_1-B_3	-17(-18)[d]
V_NO_{2B}	C_s	$^2A''$	$(a'')^2(1a')^2(a'')^1$	$^2A'$	$(a'')^2(1a')^1(a'')^2$	1.90[f]	B_1	554(506)[c]
V_NN_B	C_{2v}	$^2B_1$	$(a_1)^2(1b_1)^1(2b_1)^0$	$^2B_1$	$(a_1)^2(1b_1)^0(2b_1)^1$	2.12[f]	N_1	66
V_NC_B	C_{2v}	$^1A_1$	$(2a_1)^2(1b_1)^0(2b_1)^0$	$^1B_1$	$(2a_1)^1(1b_1)^1(2b_1)^0$	2.08[g]	-	-
$^3V_NC_B$[a]	C_{2v}	$^3B_1$	$(2a_1)^1(1b_1)^1(2b_1)^0$	$^3B_1$	$(2a_1)^1(1b_1)^0(2b_1)^1$	1.58[g]	C	473
V_BC_N	C_{2v}	$^3B_2$	$(a_2)^1(1b_1)^1(2a_1)^0$	$^3A_2$	$(a_2)^1(1b_1)^0(2a_1)^1$	1.54	C	28
$V_BC_NSi_N$	C_s	$^2A'$	$(a'')^2(1a')^1(2a')^0$	$^2A'$	$(a'')^2(1a')^0(2a')^1$	2.03[f]	B_1	338
$V_NC_BSi_B$	C_s	$^2A''$	$(1a')^2(1a'')^1(2a'')^0$	$^2A''$	$(1a')^2(1a'')^0(2a'')^1$	0.62[f]	Si	66

[a] The ground state is calculated to be $^1A_1$ and here the results presented are for the lowest-energy triplet state, $^3B_1$.
[b] In ref. [114], a signal is observed of magnitude $|A_{xx}+A_{yy}+A_{zz}|/3 = 22.43\pm1.4$ MHz that is attributed to an N_v centre.
[c] In Ref. [109], a signal is observed of magnitude $|A_{xx}+A_{yy}+A_{zz}|/3 = 117.06$ MHz that is attributed to an N_V^{-1} TBC, as well as a signal at 352.70 MHz attributed to an oxygen-containing V_NO_{2B} OBC.
[d] In Ref. [113], a signal is observed of magnitude $|A_{xx}+A_{yy}+A_{zz}|/3 = 20.83$ MHz that is attributed to the B^{11} atoms in a C_N TBC.
[f] From PBE calculations, see ref. [44]; est. maximum difference to HSE06 is 0.5 eV.
[g] HSE06 after correction based on ab initio results, see Figs. 7.1; observed value [11,24,192] of 1.95 eV.
[h] List of all defect orbitals within the h-BN conduction and valence bands, with their occupancy in the dominant wavefunction configuration.

5.1 Three-boron centre defects (TBC)

Three-boron centre defects are associated with the loss of a nitrogen atom from a site in h-BN, a site surrounded by three different boron atoms. They are important as they can act as activation, recombination, absorption, or photosensitivity centres [113,115,116,193]. In

experiments, they have been observed to display 10-line EPR spectra [109-114], but their precise chemical nature remains unknown. I consider three possibilities: a simple neutral defect V_N in which the nitrogen atom is just removed from the h-BN lattice, this with an electron trapped, V_N^{-1}, and its variant in which a carbon atom replaces the nitrogen, C_N. Below I discuss the results for each of these.

5.1.1 Negatively charged nitrogen vacancy V_N^{-1}

It has been proposed that the observed EPR 10-line signal at 117.06 MHz originates from a negatively charged nitrogen vacancy V_N^{-1} that has a triplet ground state [109]. However, present and previous calculations [194] predict that V_N^{-1} has D_{3h} symmetry supporting a closed-shell singlet ground state. Table 5.I lists this result, labelling the ground state as $^1A_1'$ as well as listing the occupancies in the dominant wavefunction configuration of all orbitals found to lie in the band gap between the h-BN valence band (VB) and conduction band (CB). In this case, only two mid-gap orbitals are found in which 4 electrons need be distributed, giving a simple closed-shell structure expressed in terms of them as $(a_1'')^2(a_2'')^2$. All the triplet states are predicted to be of much higher energy than the ground state singlet. As DFT calculations of the type I perform have been found to underestimate the stability of closed shell singlet states compared to triplet states [82], this result is likely to be robust. If V_N^{-1} indeed has a singlet ground state, then it cannot possibly be the source of the observed EPR signal.

5.1.2 Uncharged nitrogen vacancy V_N

This defect has been previously modelled and many key properties determined [195]. In the optimized ground-state structure shown in Fig. 5.1, the three boron atoms surrounding the vacancy relax towards each other, forming a triangular structure with D_{3h} symmetry; details of this structure are given in Appendix Table 0.2. The distance between any two of the boron atoms surrounding the vacancy is optimized to 2.21 Å, significantly shorter than the separation of 2.51 Å found between any two N-N or B-B nearest neighbours in pristine h-BN. Such changes are expected as the atoms surrounding the defect strive to rearrange to eliminate dangling bonds, possibly liberating a lot of energy, opposed by constraint forces coming from the surrounding material. Table 5.I shows the two defect orbitals located within the h-BN band gap, with the ground state (GS) having, an electronic configuration of $(a_2'')^1(e')^0$ with $^2A_2''$ π-type symmetry and a net spin polarization of 1.0. The calculated spin density is shown in Fig.

5.1(a), its major contribution coming from the $2p_z$ orbitals of the three boron atoms surrounding the vacancy (≈ 0.25 μ_B each), with the remaining contributions arise mostly form the B and N atoms in the next coordination shell.

Significantly, the appearance of two defect orbitals in the band gap allows for the possibility of sharp optical absorption and/or emission spectra [44] involving the ground state and the $^2E'$ excited state, of configuration $(a_2'')^0(e')^1$, the emission energy is listed under column PL in Table 5.I. While such transitions are symmetry forbidden, strong vibronic coupling associated with Jahn-Teller distortion could provide useful PL spectra. The calculated PL energy is 3.15 eV as listed in Table 5.I; this value is slightly underestimated as compared with previous GW calculations [196] as GW overestimates the band gap of h-BN. However, the excited state is open shell as it contains one electron distributed amongst the two components of the e' orbital. This is a different type of open-shell character to that considered in the high-level ab initio calculations [82] (considered in later chapters) and hence likely errors in this value are difficult to estimate.

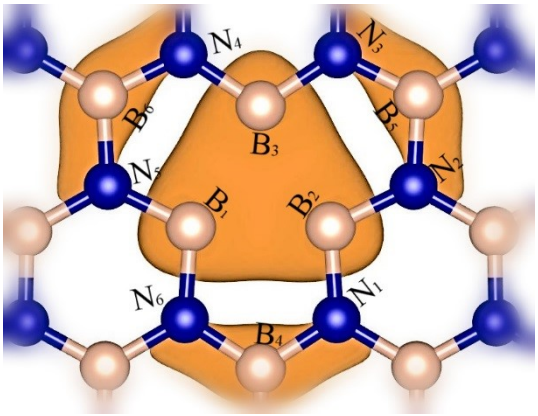

Figure 5.1 Geometrical structure and isosurface of the calculated spin density for the neutral V_N centre in h-BN shown from (001) plane at isovalue 0.001/°Å^3. Spin density is concentrated on the labelled atoms, providing significant hyperfine couplings.
.

Appendix Table 0.I lists calculated HF coupling constants for various atoms surrounding V_N in its ground state. Table 5.I lists the average principle value $(A_{xx}+A_{yy}+A_{zz})/3$ calculated for the HF coupling tensors of the most significant atoms of the defect, B_1-B_3, as 32 MHz when the calculations exclude core contributions and 22 MHz when this effect is added. An h-BN defect signal has been observed in EPR spectra for the average magnitude of the principle values of the HF tensor (the Fermi-contact term) at 22.43±1.4 MHz and attributed [114] to an V_N type defect. Present calculations support this conclusion and indicate that the signal arises from the three boron-defect atoms numbered B_1 - B_3 in Fig. 5.1, as expected.

5.1.3 C_N centre (substitutional carbon impurity)

The optimized structure for the C_N defect obtained when a carbon atom substitutes a nitrogen atom is shown in Fig. 5.2. The structure has D_{3h} symmetry and is very similar to pristine h-BN, with neighbouring B-N bond lengths of 1.437Å compared to 1.443 Å before substitution. The ground-state electronic structure is predicted to be $^2A_1''$with, as previously predicted [194,197] only one orbital in the h-BN band gap. This state has π-type symmetry and net spin-polarization of 1.0. The calculated band gap of a h-BN sheet (HSE06 method) with a C_N defect of 5.73 eV is in good agreement with previous studies [194,197]. Fig. 5.2 shows that the unpaired spin localizes prominently on the p_Z orbital of the carbon atom. Given the wide range of values that HF coupling constants can take, the calculated average value of the hyperfine coupling constant of -17 MHz is close to the observed magnitude of 20.83 MHz (the sign of HF coupling constant cannot be determined in measurements) [113] in C^{13}-enriched carbon doped BN. As only one defect orbital lies in the band gap, sharp PL from this defect is not expected.

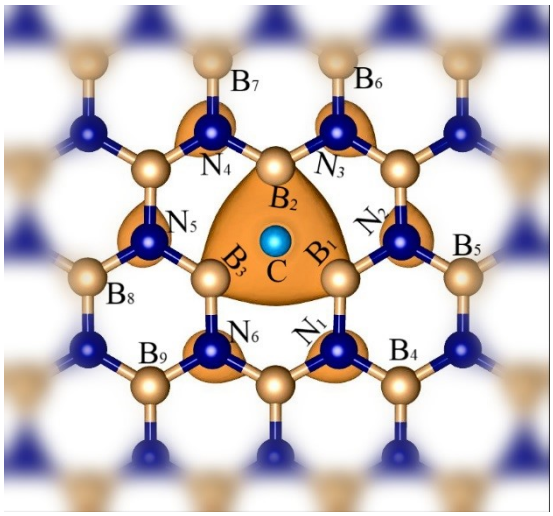

Figure 5.2 Geometrical structure and isosurface of the calculated spin density for C_N centre in h-BN shown from (001) plane at isovalue 0.001/°Å^3. Spin density is concentrated on the labelled atoms, providing significant hyperfine couplings.

5.2 One-Boron centre defect (OBC)

Oxidation of mono-vacancies in h-BN has previously been studied with the aim of investigating the potential degradation of h-BN in the atmosphere and its impact on electronic and magnetic properties [108]. It has been suggested that oxidized species provides the paramagnetic centre producing observed OBC 4-line EPR spectra [111,198].

5.2.1 V_NO_{2B} centre

To understand this effect, I consider a possible V_NO_{2B} structure in which two oxygen atoms substitute boron at the defect site, making the simplest-possible oxidized OBC. The optimized structure for this defect, which has C_s symmetry, is shown along with its calculated spin density in Fig. 5.3. In Table 5.I its electronic structure is reported, there being 3 defect orbitals in the h-BN band gap occupied by 5 electrons in the configuration $(a'')^2(1a')^2(2a'')^1$ to make a $^2A''$ ground state. In this, the unpaired electron is concentrated on atom B_1 and polarizes the oxygen atoms to give them negative hyperfine couplings. The average value of the HF coupling constant is calculated to be rather large, 506 MHz, in qualitative agreement with the observed magnitude [111] of 352.70 MHz for the OBC defect. PL from the $^2A'$ is expected at an energy of 1.90 eV [44]. Although the calculated HF values are not in very close agreement with the experiment, it is worth nothing that the experiments were performed on a 3D samples [111], and values reported are average of three HF constants i.e. A_{XX}, A_{YY} and A_{ZZ}. Therefore, the overestimation of the HF values in calculations (on 2D h-BN) are probably due to the unpaired spin density along the vacuum dimension (as is clear from Appendix Table 0.1), which gives large HF value for A_{ZZ}.

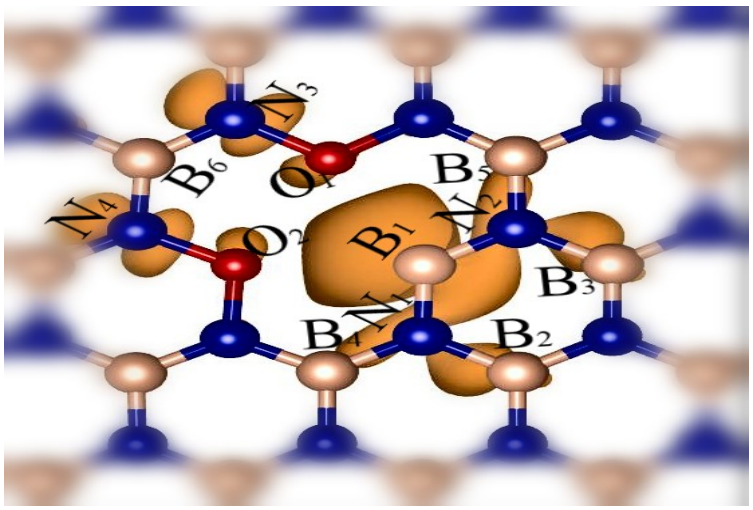

Figure 5.3 Geometrical structure and isosurface of the calculated spin density for V_NO_{2B} centre in h-BN shown from (001) plane at isovalue 0.001/°Å^3. Spin density is concentrated on the labelled atoms, providing significant hyperfine couplings.

5.3 Anti-site defect V_NN_B

Nitrogen vacancies coupled with nitrogen substitution for boron on adjacent "anti" atomic sites have been proposed as a likely source of the observed intense room temperature single

photon emission from 2-D h-BN nano-flakes [11,21]. Recently, very interesting applications of spin mechanics involving cooling of a mechanical resonator by coupling spin-qubits with the V_NN_B defect in h-BN have been proposed. While no experimental EPR data is currently available for this defect, I simulate its properties so as to aid subsequent spectral assignment.

The calculated geometrical structure and spin density are shown in Fig. 5.4. The structure has C_{2v} symmetry with a $^2B_1$ π-type ground state, the unpaired electron density is localized mainly on the p_z orbital of the N_1 atom. The ground state electronic configuration of the orbitals within the h-BN band gap is $(a_1)^2(1b_1)^1(2b_1)^0$ and the PL state also is predicted to have $^2B_1$ symmetry with the $(a_1)^2(1b_1)^0(2b_1)^1$ configuration, as has been previously proposed. PL is thus predicted to be polarized in-plane along the C_{2v} axis, with calculated adiabatic transition energy 2.12 eV [44]. This is in agreement with observations and previous calculations [11].

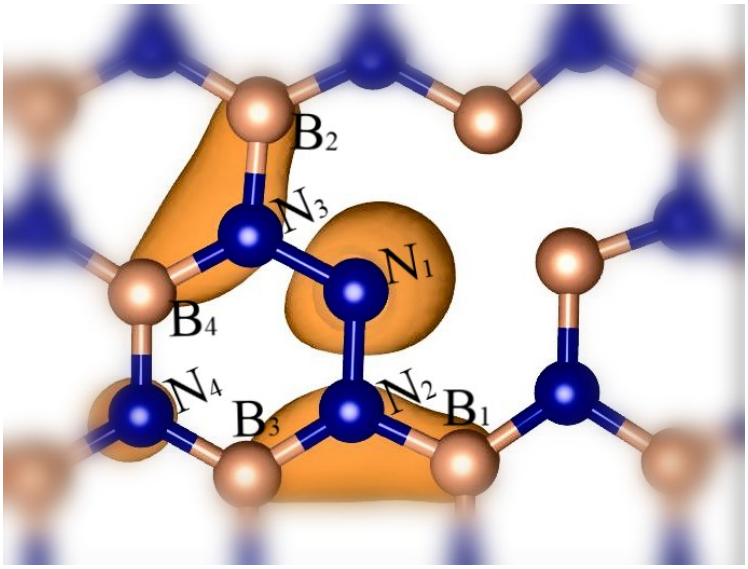

Figure 5.4 Geometrical structure and isosurface of the calculated spin density for V_NN_B centre in h-BN shown from (001) plane at isovalue 0.001/°Å^3. Spin density is concentrated on the labelled atoms, providing significant hyperfine couplings.

5.4 Carbon and silicon related centres at nitrogen and boron vacancies V_NC_B, V_BC_N, $V_BC_NSi_N$ and $V_NC_BSi_B$

While V_NN_B was proposed in the original work [11], many related defects have been postulated later [44] and here I consider the properties of some feasible defect sites. These sites are: V_NC_B (nitrogen vacancy with one of the surrounding borons replaced with a carbon), V_BC_N (boron vacancy with one of the surrounding nitrogens replaced with a carbon), $V_NC_BSi_B$ (nitrogen vacancy with one of surrounding boron replaced with carbon and another replaced

with silicon) and $V_BC_NSi_N$ (boron vacancy with one of the surrounding nitrogen replaced with carbon and another replaced with silicon). For these, optimized structures and ground-state spin densities are shown in Fig. 5.5. Calculated defect bond lengths are provided in Appendix Table 0.2 and indicate partial stabilization of the dangling bonds present in each defect. Calculated adiabatic transition energy, ground state and excited state electronic structures are listed in table 5.I.

The calculated HF coupling constants for each (as well as the $^3B_1$ excited state of V_NC_B) are given in Table 5.I and Appendix Table 0.I. From Fig. 5.5, HF constants are dominated by the spin densities, which for V_NC_B are found to localize on the π orbitals of the carbon and neighbouring atoms. For V_BC_N, the spin density is located mostly on carbon and nitrogen π orbitals, becoming highly delocalized for $V_BC_NSi_B$. Only for $V_BC_NSi_N$, does the spin density reside on σ orbitals, these showing some delocalization.

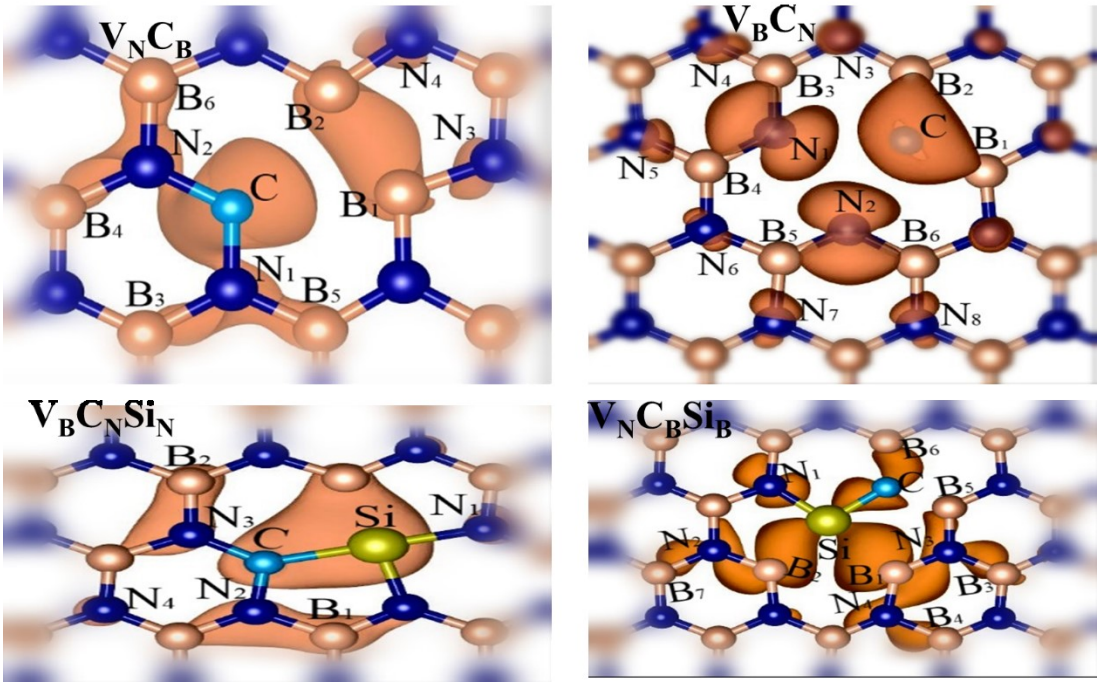

Figure 5.5 Geometrical structure and isosurface of the calculated spin density for V_NC_B (isovalue 0.003/°Å^3), V_BC_N (isovalue 0.004/°Å^3), $V_BC_NSi_N$ (isovalue 0.001/°Å^3) and $V_NC_BSi_B$ (isovalue 0.001/°Å^3) centres in h-BN shown from (001) plane. Spin density is concentrated on the labelled atoms, providing significant hyperfine couplings.

Out of all the defects studied, of particular interest is the structure of V_NC_B which has been previously predicted to be triplet in character [78,124]. However, I find the ground-state geometrical structure to be of C_{2v} symmetry and $^1A_1$ in character. In this thesis (next few chapters), properties of this defect have been the subject of my comprehensive calculations

comparing the results of DFT methods including the ones employed here to both ab initio calculations and various first-principles and empirical DFT calculations using model compounds to mimic the V_NC_B defect [82]. These calculations indicate that the presently used method significantly *underestimates* the stability of the $^1A_1$ compared to the lowest-energy triplet state, $^3B_1$. Hence, it is clear that the actual ground state should indeed be $^1A_1$. The adiabatic energy difference between these states evaluated by DFT is 0.34 eV, but adding the correction terms found for the model compound would suggest an energy difference more like 0.74 eV. However, anticipating the possibility that a triplet state is one day observed for V_NC_B, results for the $^3B_1$ state are also reported in Fig. 5.5 and Table 5.I. For V_BC_N, the ground state is calculated to be of triplet character, whereas for $V_NC_BSi_B$ and $V_BC_NSi_N$, the ground state is calculated to be doublet (see Table 5.I).

In the next few chapters I will present the present calculations and analysis of level strcutrues and optical cycles of the most likey defects for single photon emission i.e. V_NC_B, V_BC_N and V_NN_B. Detailed consideration of the available excited states, allowed spin-orbit couplings, zero-field splitting, and optical transitions will be made and potential application of these defects in quantum computations discussed. The DFT energies calculated using HSE06 will be benchmarked with high level ab-initio calculations on a representative model compounds for V_NC_B and V_NN_B defects. My results for these calculations and correction factors are applicable to wide range of systems with considerable open shell character.

Chapter 6 Benchmarking the applied DFT functionals

Identification of defects in semi-conductors relies on the ability to calculate adiabatic transition energy within 0.1eV accuracy. This level of accuracy can be achieved only if both static (for near degenerate states and states involving multi-reference character) and dynamic electron correlation effects are taken into consideration. In this chapter, I benchmark the DFT calculations (known to poorly handle the static electron correlation being single reference method) [199] for the defects V_NC_B, V_BC_N and V_NN_B embedded in periodic structures with quantum chemistry approaches on a representative model compound.

6.1 Benchmarking the excited states of V_NC_B

In this section, I benchmark the V_NC_B defect in 2-D h-NB nanoflakes that occurs if a nitrogen vacancy has adjacent to it a carbon atom substituting a boron atom. This system is chosen as it satisfies the criteria (described in chapter 4), also this defect shows considerable complexity, with many unresolved issues concerning interpretation of experimental data [73,78,124,200,201], that may form a paradigm for the general understanding of the associated phenomena e.g. non-magnetic ground state, two groups of emitters etc. [11,21,194,195,202-205]. DFT and TDDFT results for 25 states of a model compound and for a periodic molecular layer are compared to each other and to MRCI, CASPT2, CCSD(T), CCSD, and EOM-CCSD calculations, seeking efficient and reliable methodologies. Features considered include: relative state energies at vertical and adiabatic geometries, the band widths of photo-absorption and photoemission spectra, and the effect of choice of density-functional type, all discussed in a context of the chemical forces operative at defect sites and the open-shell nature of defect singlet states.

Most DFT calculations use the HSE06 density functional [164,165] as this hybrid density functional is the highest-rung functional commonly available in periodic-lattice codes (this is the case in VASP [166,167]). It has also been shown to be quite successful at reproducing the bandgap of many semiconductor materials [100,191]. In the present work, I focus on the application of this functional along with the range-corrected hybrid functional, CAM-B3LYP [43,168,169]. This functional represents the entry level for calculating molecular spectroscopy when charge transfer states are important. It is, however, not yet implemented in any periodic boundary condition code such as VASP; I therefore restrict its use

to model compounds. TDDFT calculations need to be performed based on a reference wavefunction and so I focus on the critical importance of this choice.

The structures [124,200] of the V_NC_B defect in a periodic lattice and in a model compound are depicted in Fig. 6.1(a) and Fig. 6.1(b), respectively. These structures have all atoms planar with local C_{2v} symmetry around the defect. Using the standard axis conventions for planar molecules [94,95], the irreducible representations of this point group are a_1 and b_2 (of σ type) and b_1 and a_2 (of π type); note that a variant definition is possible that is sometimes used in which b_1 and b_2 are interchanged. The ground state or any excited state could show distortions from C_{2v} symmetry, with the defect perhaps distorting from planarity, forming structures such as those shown in Fig. 6.1 c-d. Through use of C_{2v} symmetry labels, I present a simple understanding of the basic spectroscopic properties of this defect and its propensity to undergo such distortions.

The model compound shown in Fig. 6.1(b) has one ring of h-BN atoms surrounding the defect. How this ring is terminated determines the overall electronic structure, and in Fig. 6.1(b) hydrogen atoms are used at all sites. Substitution of BH_2 and/or NH_2 for the hydrogens placed on the C_{2v} axis would allow variation between possible quinonoid, semiquinoid, and benzenoid model compounds. This small compound is adequate for the benchmarking studies. Adding additional rings of B-N around the defect would describe long-range effects more robustly but rapidly make the quantum chemical calculations intractable. Nevertheless, I find later that results for the model compound and the periodic structure are reasonably different. Some calculations are also performed on the expanded two-ring model compound shown in Fig. 6.1e and further expanded model compounds with more atoms and are shown in Appendix Table 0.3 (showing that the state energies obtained for the model compound tend to converge to the corresponding 2D energies with increasing the size of model compound).

The electronic structure of the defect is considered in terms of six defect orbitals interacting with the valence and conduction bands of the h-BN layer [124]. These comprise one σ-type orbital and one π-type orbital taken from each of the two defect boron atoms and the defect carbon atom. In Fig. 6.2. are shown the molecular orbitals calculated with HSE06 with highest defect-orbital character, i.e. orbitals with DFT energies that lie within the band gap; a feature of immediate note is that these all embody significant delocalization into the surrounding material and so any classification scheme can be only qualitatively descriptive. The σ molecular orbitals are named $1a_1$, $2a_1$, and b_2, whilst the π orbitals are named $1b_1$, $2b_1$,

and a_2. This notation is adapted, as it is invariant to the number of atoms used to model the defect, applying to both model compounds and model 2D slabs.

Each set of orbitals takes on a form similar to that found in 3-centre 2-electron bonds, usually described in terms of "bonding" orbitals ($1a_1$ and $1b_1$), "non-bonding" orbitals ($2a_1$ and $2b_1$), and "antibonding" orbitals (b_2 and a_2), but delocalization of orbitals into the surrounding material significantly distorts their shapes. Further, those labels are misleading as the C-B and B-B distances are large, possibly beyond the singlet-triplet instability point of the "bonds" that could be driven by occupancy of the "bonding" orbitals. Hence, the energy differences between the various orbital combinations are small. The critical orbitals associated with V_NC_B are shown in Fig. 6.2. HSE06 calculations place three of these six molecular orbitals within the band gap of h-BN, with the lowest-energy orbital ($1a_1$) being within the valence band and the two antibonding orbitals within the conduction band. In neutral V_NC_B, four electrons are available to occupy the six defect-site orbitals. Two electrons always occupy the deep lying $1a_1$ orbital so that the location of the other two electrons typically defines the nature of the low-energy electronic states. However, to describe quantitatively all low-energy states of V_NC_B of possible current interest, the two high-lying h-BN valence-band orbitals and two conduction-band orbitals are also included in Table 6.2. The greater character that a transition has of such orbitals, the less appropriate are defect cluster models. While this situation is quite complex, the issues raised will be apt for general situations involving defects in 2D materials, making V_NC_B a paradigm example.

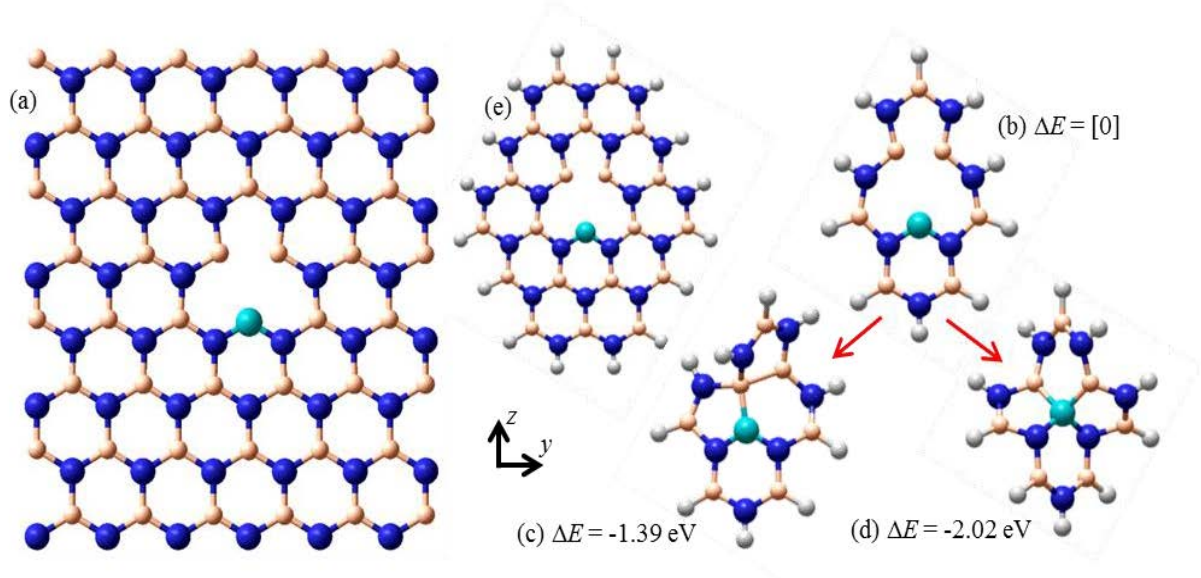

Figure 6.1 The V_NC_B defect in which a nitrogen vacancy is neighboured by a carbon substituting boron is represented as either (a) a lattice of periodic defects or (b) a model compound with C_{2v} symmetry. On relaxation below C_{2v} symmetry, the model compound forms 3-D structures (c) and (d). An expanded model compound is (e). Cyan- carbon, blue- nitrogen, peach- boron, white- hydrogen.

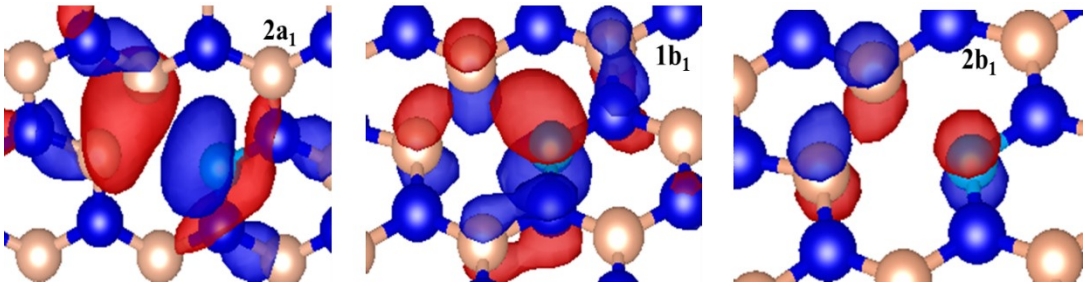

Figure 6.2 Critical orbitals largely associated with the defect site in V_NC_B

The energies of some 25 low-energy electronic states of the model compound are compared in Table 6.1, all evaluated at the same test geometry. This geometry was obtained by optimizing the structure of the 2-D layer for the $(1)^3B_1$ state, cutting out the model compound and then adding and optimizing terminating hydrogen atoms. HSE06 predicts that $(1)^3B_1$ is the lowest-energy state at this geometry whilst CAM-B3LYP, CCSD(T) and MRCI predict instead that $(1)^1A_1$ is lower in energy. In the Table, all energies relate to that of $(1)^1A_1$.

In Table 6.2, the dominant orbital occupancies for the 25 states considered are listed. Proper inclusion of the orbitals listed, as well as other significantly coupled ones, is critical to any calculation. In particular, the choice of active space presents a significant practical issue in performing MRCI and related calculations, particularly in situations such as this where many different orbitals contribute to the low-energy states of interest. As detailed in Table 6.2, 5 different active spaces were used in MRCI calculations, with the results in Table 6.1 being the obtained averages, with the standard deviations of the whole data set being 0.07 eV. This value provides a basic estimate of the precision of the method. Similarly, two active spaces are used in the CASPT2 calculations, with the standard deviation increasing to 0.3 eV. That the difference found between the two methods is so large is indicative of strong electron correlation within the defect.

DFT calculations are also subject to implementation variations; to investigate this, results for 6 states are compared in Table 6.2, obtained using Gaussian-09, applying the cc-PVTZ basis set, and using VASP, applying PAW pseudopotentials and a truncated plane-wave basis set. On average, the cc-pVTZ calculations place the excited states higher in energy by 0.06±0.02 eV. Errors of this order thus represent the basic precision of the DFT calculations and are similar in magnitude to those associated with MRCI active-space choice.

Table 6.3 provides a comparison of average and standard-deviation differences in excited state energies obtained by comparing the various computational results presented in

Table 6.1 to each other. The second column of Table 6.3 crudely summarizes the results, providing an overall estimate of errors expected from various DFT approaches, standardized against the ab initio methods. For some states, these error estimates are within the precisions discussed above for calculation evaluation, whereas in other situations the DFT results differ on average by up to 1 eV from the higher level methods. I proceed by considering the properties of the different electronic states involved, as well as those of the different DFT and ab initio methods used to model them.

Table 6.1 Energies (in eV) of various states of the V_NC_B model compound (Fig. 6.1b) with respect to $(1)^1A_1$, evaluated at the test geometry.[a]

State	MRCI[b]	CASPT2[c]	CCSD	CCSD (T)	EOM-CCSD-S	EOM-CCSD-T	HSE06 VASP	HSE06 G09	HSE06 TD-S	HSE06 TD-T	CAM	CAM TD-S	CAM TD-T
$(2)^1A_1$		2.30	2.73	2.03			2.06	2.11			2.61		
$(1)^1B_1$	1.45	0.94			1.25			0.63	0.62		0.89	0.91	
$(2)^1B_1$		2.98			3.44			2.57	2.61		3.05	3.06	
$(3)^1B_1$		4.24			4.65				3.62			4.28	
$(4)^1B_1$		4.68							4.96			5.53	
$(1)^1B_2$	5.19	4.22			4.79			3.89	3.96		4.36	4.56	
$(2)^1B_2$	5.15	4.37			4.62			3.79	3.84		4.34	4.40	
$(1)^1A_2$	3.28	3.03			3.36			2.34	2.22		2.74	3.01	
$(2)^1A_2$					4.36				3.37			4.02	
$(1)^3A_1$	3.96	3.50	3.97	3.66		4.01	3.09	3.17		3.14	3.63		3.62
$(2)^3A_1$									4.17	4.25		4.87	4.92
$(3)^3A_1$									4.37	4.49		5.16	5.23
$(4)^3A_1$									4.69	4.81		5.19	5.45
$(5)^3A_1$		5.22	5.57	5.15		5.07		4.75		5.05	5.30		5.34
$(1)^3B_1$	0.32	0.02	0.24	0.24	0.25	[0.24]	-0.20	-0.16	-0.59	[-0.16]	0.09	-0.61	[0.09]
$(2)^3B_1$		2.34			2.63	3.01	1.99	2.07	1.80	2.10	2.52	2.20	2.62
$(3)^3B_1$		4.33							3.49	3.57		4.16	4.16
$(4)^3B_1$										4.49		5.00	5.04
$(5)^3B_1$		5.22							4.49			5.26	5.33
$(1)^3B_2$			4.19	4.01	4.21	4.59		3.55	3.35	3.57	3.91	3.75	4.21
$(2)^3B_2$	4.96	4.66	4.74	4.42	4.60			3.91	3.76	3.95	4.46	4.32	4.97
$(1)^3A_2$	3.27	2.42	3.01	2.85	3.32	3.18	2.23	2.29	2.15	2.26	2.70	2.94	2.83
$(2)^3A_2$					4.33	4.29			3.29	3.38		3.94	3.89
$(3)^3A_2$		3.96	5.25	4.65				4.05		3.96	4.78		4.76

CAM ≡ CAM-B3LYP; EOM-CCSD and TDDFT calculations are preformed from both the $(1)^1A_1$ reference state ("-S") and the $(1)^3B_1$ reference state ("-T"). [b] Average of 5 calculations using different active spaces, ±0.07 eV. [c] Average of 2 calculations using different active spaces, ±0.3 eV.

Table 6.2 Dominant state occupancies and details of CASPT2 and MRCIC calculations.

State	Dominant orbital occupancy[a]										CASPT2			MRCIC					
	V_{b1}	V_{a2}	$1a_1$	$2a_1$	$1b_1$	$2b_1$	b_2	a_2	C_{a2}	C_{b1}	(8,8)	(6,9)	ave.	(6,9)	(8,8)	(8,10)	(10,10a)	(10,10b)	ave.
$(1)^1A_1$	2	2	2	2	0	0	0	0	0	0	[0]	[0]		[0]		[0]	[0]	[0]	[0]
$(2)^1A_1$	2	2	2	0	2	0	0	0	0	0	2.33	2.26	2.30						
$(1)^1B_1$	2	2	2	1	1	0	0	0	0	0	0.96	0.91	0.94	1.57	1.51	1.54	1.45	1.44	1.45
$(2)^1B_1$	2	2	2	1	0	1	0	0	0	0	3.08	2.88	2.98						
$(3)^1B_1$	2	2	2	1	0	0	0	0	0	1	4.24		4.24						
$(4)^1B_1$	1	2	2	1	2	0	0	0	0	0		4.68	4.68						
$(1)^1B_2$	2	2	2	1	0	0	1	0	0	0	4.07	4.36	4.22	5.44			5.27	5.11	5.19
$(2)^1B_2$	2	1	2	2	1	0	0	0	0	0	4.29	4.44	4.37		5.14	5.15			5.15
$(1)^1A_2$	2	2	2	1	0	0	0	1	0	0	3.04	3.01	3.03	3.41	3.37	3.42	3.28	3.27	3.28
$(2)^1A_2$	2	2	2	1	0	0	0	0	1	0									
$(1)^3A_1$	2	2	2	0	1	1	0	0	0	0	3.51	3.49	3.50	3.98	3.97	3.96	3.96	3.96	3.96
$(5)^3A_1$	2	2	1	1	2	0	0	0	0	0	5.23	5.20	5.22						
$(1)^3B_1$	2	2	2	1	1	0	0	0	0	0	-0.03	0.07	0.02	0.40	0.37	0.41	0.35	0.28	0.32
$(2)^3B_1$	2	2	2	1	0	1	0	0	0	0	2.34	2.34	2.34						
$(3)^3B_1$	2	2	2	1	0	0	0	0	0	1	4.33		4.33						
$(5)^3B_1$	2	2	1	2	0	0	0	0	0	1		5.22	5.22						
$(1)^3B_2$	2	2	2	1	0	0	1	0	0	0									
$(2)^3B_2$	2	1	2	2	1	0	0	0	0	0	4.43	4.88	4.66±0.25	5.25	4.96	4.97	4.92	5.00	4.96
$(3)^3B_2$	2	1	2	2	0	0	0	0	1	0	6.76	7.05							
$(1)^3A_2$	2	2	2	1	0	0	0	1	0	0	2.69	2.14	2.4±0.3	3.62	3.63	3.60	3.27	3.26	3.27
$(2)^3A_2$	2	2	2	1	0	0	0	0	1	0									
$(3)^3A_2$	2	1	2	1	2	0	0	0	0	0	3.66	4.25	3.9±0.4						
$(4)^3A_2$	2	1	2	1	1	0	0	0	1	0		4.35	4.35						

[a] The critical defect-dominant orbitals are shown in Fig. 6.2; to describe the above states, to these are added the highest-energy valence band (V) orbitals of b_1 and a_2 symmetry, as well as the lowest-energy conduction-band (C) orbitals of a_2 and b_1 symmetry.

6.1.1 Triplet states

Calculations of energy differences within the triplet-state manifold are perhaps the ones that are least prone to systematic errors, and one would expect the CCSD(T) and DFT results both to be reliable. For triplet states, according to the Gunnarsson-Lundqvist (extended Kohn-Sham [206]) theorem [163], DFT energies can be evaluated directly for the lowest-energy state of any given spin or spatial symmetry. Sometimes higher-energy states can also be identified, provided that convergence criteria are set course enough. Higher energy states of the triplet manifold are evaluated using the ΔSCF approach.

While Tables 6.1 and 6.3 presents state energies relative to $(1)^1A_1$, Table 6.4 depicts the higher-energy triplet states relative to $(1)^3B_1$ triplet ground state to focus only on properties of the triplet-state manifold. Comparisons are made for ΔSCF calculations using the PBE, HSE06, and CAM-B3LYP density functionals. HSE06 performs best with an average difference to CCSD(T) of -0.10±0.07 eV; CAM-B3LYP shows its customary over-estimation

[42,43] of energies by ca. 0.2 eV, with an average difference of 0.16±0.12 eV, while PBE results are very poor at -0.90±0.29 eV. Clearly, PBE is inappropriate to the study of defect sites and I do not investigate this method further. In addition, comparisons are also made to TDDFT results obtained using direct calculations with $(1)^3B_1$ as the reference state, returning similar differences of -0.07±0.20 eV for HSE06 and 0.32±0.21 eV for CAM-B3LYP, with the variability of the results increasing somewhat compared to ΔSCF calculations for each individual state.

In addition, Table 6.2 also compares results within the triplet manifold for MRCI, CASPT2, CCSD, and EOM-CCSD to those from CCSD(T). Average differences are of order 0.3 eV, indicating variability in the quality of the treatments of the 6 excited states considered. In principle, the CCSD(T) calculations are expected to perform well as they contain a consistent treatment of triples excitations, but the MRCI and CASPT2 approaches better include any multi-reference character. In the absence of MRCI calculations including full inclusion of triples excitations, it is difficult to make an estimate of likely errors based on convergence of the ab initio results towards the exact answer for the basis set used, but combining the ab initio and DFT results is suggestive that triples excitations are more important than multi-reference character amongst the triplet manifold. A conservative analysis is that the CCSD, MRCI and EOM-CCSD methods can only determine state energies to an accuracy of on average 0.3 eV. EOM-CCSD(T) is an additional method that should prove useful in these applications [135].

Table 6.3 Corrections to add to DFT calculated transition energies from $(1)^1A_1$ (second column, in eV), determined from averaged differences in transition energies predicted by the methods listed in the rows compared to those in the later columns, for the V_NC_B model compound (Fig. 6.1b), evaluated at a test geometry.

method	Corr.	MRCI	CASPT2	CCSD	CCSD (T)	EOM-CCSD-S	EOM-CCSD-T	HSE06 closed	HSE06 open	HSE06 trip.
CASPT2		8 −0.6±0.3								
CCSD		4 −0.1±0.1	7 0.5±0.4							
CCSD(T)		4 −0.3±0.2	7 0.1±0.3	8 −0.3±0.2						
EOM-CCSD-S		7 −0.2±0.2	10 0.4±0.2	4 0.1±0.2	4 0.2±0.2					
EOM-CCSD-T		3 −0.0±0.1	5 0.4±0.3	5 0.0±0.3	5 0.2±0.2	5 0.1±0.2				
HSE06 closed	0.0		1 −0.2	1 −0.6	1 0.1					
HSE06 open	1.0	4 −1.1±0.2	5 −0.5±0.1			5 −0.8±0.1				
HSE06 trip	0.7	4 −0.8±0.2	7 −0.3±0.2	7 −0.8±0.2	7 −0.5±0.1	5 −0.7±0.2	6 −0.7±0.3			
HSE06 TD-S	0.9	7 −1.1±0.2	13 −0.5±0.3	4 −0.9±0.1	4 −0.7±0.1	13 −0.9±0.1	6 −1.1±0.2		5 0.0±0.1	5 −0.2±0.1
HSE06 TD-T	0.7	4 −0.8±0.2	8 −0.3±0.3	7 −0.7±0.3	7 −0.5±0.2	6 −0.7±0.2	8 −0.8±0.4			8 0.0±0.1
CAM	0.3	8 −0.5±0.2	13 0.1±0.3	8 −0.3±0.1	8 0.1±0.2	10 −0.3±0.2	6 −0.3±0.3	1 0.5	5 0.4±0.1	8 0.5±0.1
CAM TD-S	0.5	7 −0.6±0.2	13 0.0±0.4	4 −0.4±0.3	4 −0.3±0.4	13 −0.4±0.2	6 −0.6±0.2		5 0.5±0.1	5 0.2±0.4
CAM TD-T	-0.2	4 −0.3±0.2	9 0.2±0.3	7 −0.2±0.2	7 0.1±0.2	6 −0.1±0.3	8 −0.3±0.2			8 0.6±0.2

	HSE06 TD-S	HSE09 TD-T	CAM	CAM TD-S
HSE06 TD-T	10 0.2±0.1			
CAM	10 0.5±0.1	8 0.4±0.2		
CAM TD-S	19 0.6±0.2	11 0.4±0.3	10 −0.1±0.3	
CAM TD-T	11 0.8±0.2	14 0.6±0.2	8 0.1±0.2	12 0.2±0.3

Listed are the number of states used in each comparison, the average difference (in eV), and its standard deviation (in eV). CAM ≡ CAM-B3LYP; HSE06 direct energy calculations for closed-shell singlets, open-shell singlets, and triplet states are shown separately; EOM-CCSD and TDDFT calculations are preformed from both the $(1)^1A_1$ reference state ("-S") and the $(1)^3B_1$ reference state ("-T").

Table 6.4 At the reference geometry, the second column shows the CCST(T) calculated triplet-state energy differences ΔE compared to $(1)^3B_1$, in eV, adapted from Table 6.1, while the remaining columns show the differences from these results obtained using other computational methods, again in eV.

state	CCSD (T) ΔE	MRCI	CASPT2	CCSD	EOM-S	EOM-T	HSE06 G09	HSE06 TD-S	HSE06 TD-T	CAM	CAM TD-S	CAM TD-T	PBE
$(1)^3A_1$	3.42	0.22	0.06	0.31		0.35	-0.09		-0.12	0.12		0.11	-0.59
$(5)^3A_1$	4.91		0.29	0.42		-0.08	0		0.3	0.3		0.34	-1.42
$(1)^3B_2$	3.77			0.18	0.19	0.58	-0.06	0.17	-0.04	0.05	0.59	0.35	-0.82
$(2)^3B_2$	4.18	0.46	0.46	0.32	0.17		-0.11	0.17	-0.07	0.19	0.75	0.7	-0.97
$(1)^3A_2$	2.61	0.34	-0.21	0.16	0.46	0.33	-0.16	0.13	-0.19	0	0.94	0.13	-0.67
$(3)^3A_2$	4.41		-0.47	0.6			-0.2		-0.29	0.28		0.26	-0.95
average		0.34	0.03	0.33	0.27	0.30	-0.10	0.16	-0.07	0.16	0.76	0.32	-0.90
standard deviation		0.12	0.37	0.16	0.16	0.27	0.07	0.02	0.20	0.12	0.18	0.21	0.29

6.1.2 Closed-shell singlet states

Only two closed-shell singlet states are considered, $(1)^1A_1$ and $(2)^1A_1$. Of these, $(1)^1A_1$ is of critical importance as most calculations predict it to be the ground state. Typically, closed-shell singlet states are the easiest to calculate as they are often dominated by single-reference character and lead to chemical stability, but this scenario is unlikely to apply to defect states. In $(1)^1A_1$, the $2a_1$ orbital (see Fig. 6.2 and table 6.2) is doubly occupied, whereas, in $(2)^1A_1$, $2b_1$ is doubly occupied instead. Both involve electron delocalization over atomic centers that are a long way apart, an unusual property that inherently introduces multi-reference character into wavefunctions. The inter-atomic interactions are barely strong enough to support this delocalization; to allow the electrons to localize on individual atomic centers, the mixing in of double excitations, from amongst in particular the critical defect orbitals shown in Fig. 6.2, must occur. In general in molecules, this issue becomes critical at bond-broken geometries beyond the singlet-triplet instability point [38], leading to poor results for DFT ground states and catastrophic failure of TDDFT for excited states. This effect is known as "static electron correlation" and is a distinctly different phenomenon to the dynamical correlation effects addressed in different ways by the DFT and ab initio calculations.

Whereas Table 6.4 shows excellent agreement between DFT results and CCSD(T) calculations for energy gaps within the triplet manifold, Tables 6.1 and 6.3 report energy gaps with reference to $(1)^1A_1$. For HSE06, the average deviation from CCSD(T) for the triplet-state energies relative to the singlet ground state becomes -0.5±0.1 eV (Table 6.2) compared to -0.10±0.07 (Table 6.4) for relative energies within the triplet manifold. This is indicative of the serious issues involved in obtaining a realistic electronic structure for $(1)^1A_1$. CAM-B3LYP performs much better, however, the error with respect to $(1)^1A_1$ being just 0.1±0.2 eV (Table 6.2).

All of the CCSD(T) and the DFT calculations are based on single-reference wavefunctions and so are subject to errors associated with the multi-reference nature of $(1)^1A_1$. Insight into the process is obtained by comparing CCSD(T) results to CCSD in Table 6.3: CCSD(T) systematically includes much more of the multi-reference character than does CCSD, with CCSD transition energies being on average 0.3±0.2 eV higher in energy.

While CCSD and more so CCSD(T) (asymmetrically) include static electron correlation to some extent, DFT largely misses it. If the effect is too severe then DFT

calculations yield open-shell singlet states with lower energies than analogous closed-shell states. I tested for this effect and found it not to occur, meaning that DFT and TDDFT should deliver qualitatively useful results, as I find; the question then becomes one of quantitative accuracy.

An alternative ab initio computational method to CCSD(T) giving results independent in quality of the degree of multi-reference character is MRCI and its approximation CASPT2. These method embodies exact treatment of exchange and correlation within selected key orbitals, coupled to either variational or perturbation treatments of the dynamic electron correlation. The MRCI calculations that are performed here are truncated at the level of singles and doubles expansion and hence do not include the triples contributions identified as significant for the relative energies of the triplet-state manifold, however. The errors listed in Table 6.3 for HSE06 compared to MRCI are -0.8±0.2 eV, being also -0.6±0.2 eV for CAM-B3LYP; these are very much larger than the ca. 0.3 eV magnitude errors associated with neglect of triples excitations and emphasize the failure of DFT for the closed-shell $(1)^1A_1$ state.

Indeed, HSE06 predicts that $(1)^3B_1$ should be the ground state at an energy 0.16 eV lower than that of $(1)^1A_1$, owing to its poor treatment of $(1)^1A_1$, whereas MRCI, CCSD, CCSD(T), and EOM-CCSD all predict it to be ca. 0.25 eV higher in energy. For this result, of significant immediate concern regarding interpretation of spectral data for h-BN [201], the ab initio methods yield robust results while the DFT calculations suffer from significant systematic errors. CAM-B3LYP more realistically predicts the triplet state is less favored by 0.09 eV (Table 6.1), whereas PBE predicts it to be more stable by 0.59 eV (Table 6.3); these results form a basis for a first-principles understanding of the nature of the density functionals involved [42,43].

TDDFT calculations based on the $(1)^1A_1$ reference state provide another way of calculating properties of the triplet-state manifold. Table 6.4 highlights these in terms of their ability to predict properties from purely within the triplet-state manifold: HSE06 performs very well, with average errors compared to CCSD(T) of 0.16±0.2 eV, similar to the ΔSCF results of -0.10±0.07 eV and the $(1)^3B_1$-reference TDDFT results of -0.07±0.20 eV. However, analogous CAM-B3LYP result fail badly, the error being 0.76±0.18 eV compared to 0.16±0.12 eV (direct) and 0.32±0.21 eV (triplet reference). The results serve to stress the great danger in performing TDDFT calculations based on closed-shell reference functions when the ground

state is actually multi-reference in nature [38]. Such approaches should not be applied to model defect-state spectroscopy.

Associated with strong multi-reference ground-state character is often the presence of low-energy doubly excited electronic states. Indeed, $(2)^1A_1$ is predicted by all computational methods to be the second-lowest energy singlet excited state, the lowest-energy singlet excited state being the open-shell state $(1)^1B_1$ for which $(2)^1A_1$ is the associated doubly excited state from $(1)^1A_1$ (see Table 6.4). The difference between the CCSD(T) energy of 2.03 eV and the CCSD energy of 2.73 eV (Table 6.1) is very large and suggestive of the much better treatment of static electron correlation that CCSD(T) affords. HSE06 and CAM-B3LYP predict 2.11 eV and 2.61 eV, respectively. TDDFT and EOM-CCSD inherently misrepresent doubly excited states and are not suitable for their search.

6.1.3 Open-shell singlet states

Many examples of open-shell singlets are reported in Table 6.1. Calculation for these states are even more complex than those for closed-shell singlets as they are *intrinsically* open-shell in nature, being represented at the simplest level as an equally weighted sum of two Slater determinants. This minimalistic treatment of static electronic correlation is provided by the MRCI, CASPT2, EOM-CCSD, and TDDFT methods but not but by CCSD, CCSD(T), or ΔSCF approaches. An ab initio extension of CCSD(T) to include multi-reference effects is available [141,142], as is a successful empirical extension of DFT[143]; also, methods that merge the two approaches that are applicable to periodic materials are being introduced [144-154]. However, such approaches are poorly available and rarely applied in practice, despite their desirability.

In lieu of a first-principles approach, ΔSCF calculations of open-shell singlet states are usually performed using an empirical multi-reference ansatz: the energy of spin-contaminated states calculated by setting the number of spin-up and spin-down electrons to be the same whilst setting the orbital occupancy (see Table 6.2) of an open-shell excited state is assumed to be the *average* energy of the singlet and triplet states [207]. By also calculating the energy of the triplet state at the same geometry, the energy of the singlet state can thus be estimated. In principle, forces can be determined using the same ansatz and hence geometries optimized, but in practice often only the energy of the spin-contaminated state is optimized. As spin contaminated states violate the Gunnarsson-Lundqvist theorem [163], they are not valid

solutions to DFT and hence any meaning associated to them is purely empirical. The possible consequences of this for the complex states manifest at defect sites remains unknown.

Tables 6.1 and 6.2 depict relatively good agreement between MRCI and EOM-CCSD calculations for all states, but specifically, for the 4 open-shell singlet states treated by both methods, the average EOM-CCSD difference to MRCI is only –0.26±0.27 eV, despite the multi-reference nature of the states. This is small compared to the differences between ab initio and DFT results: 1.2±0.2 eV (ΔSCF) and 1.1±0.2 eV (TDDFT) for HSE06, with also 0.6±0.2 eV (ΔSCF) and 0.7±0.2 eV (TDDFT) for CAM-B3LYP. For both density functionals, the use of empirical ΔSCF schemes yields results very similar to TDDFT (0.0±0.1 eV for HSE06 and 0.1±0.3 eV for CAM-B3LYP from Table 6.3), so this approach is not the cause of the problem. Rather, the problems are intrinsic ones associated with the poor treatment of multi-reference character in traditional DFT.

6.1.4 Geometry optimization and chemical forces

Some other issues concerning calculation of the properties of defect states are presented in Table 6.5. In this table, all energies are reported at geometries individually optimized with most columns referring to the model compound whilst the last two columns are for the 2-D material. CAM-B3LYP, CCSD(T) and EOM-CCSD single-point energies are also evaluated at these structures. Geometry optimization is seen to enhance the effects found previously at the reference geometry. ΔSCF calculations, TDDFT, and CCSD(T) tell a consistent story for the triplet manifold, whilst empirical DFT and TDDFT give similar results for the open-shell singlet states that are far removed from the EOM-CCSD ones. As the ground state of a defect is determined by the adiabatic differences in state energies evaluated at fully optimized geometries, reliable DFT predictions of defect properties becomes difficult and human-intuition dependent. Understanding how the errors in the DFT calculations change with geometry requires understanding the operational chemical forces and their consequences concerning the shapes of the potential-energy surface manifolds.

Table 6.5 Energies (in eV) of various states of the V_NC_B model compound and related periodic 2-D material (Fig. 6.1), evaluated at their adiabatic minimum-energy geometries, as well as the HSE06 free-energy correction *ΔGcorr*, in eV at 298 K, the nature of any imaginary frequencies, the reorganization energies λ depicting the width, in eV, of spin-allowed photoabsorption (and approximately PL) spectra from either the $(1)^1A_1$ (singlet) ground state or the $(1)^3B_1$ (triplet) ground state.

	Model compound											2-D	
State	HSE06 G09	HSE06 VASP	HSE06 TDDFT[a]	HSE06 Est.[b]	CCSD(T)[c]	EOM-CCSD[c]	ΔG_{corr}	Imag. Freq.	λ HSE06[ad]	λ CCSD[ce]	λ CAM-B3LYP[a]	HSE06 VASP	λ HSE06
$(1)^1A_1$	[0]	[0]	[0]	-1.2	[0]	[0]	[0]	b_1[g]	[0]	[0]	[0]	[0]	[0]
$(2)^1A_1$	1.93	2.50		4.28	2.21		-0.04	a_2,b_1[h]	3.32	2.46	2.41	2.46	1.15
$(1)^1B_1$		1.59	1.54	[1.54]		2.30	0.00	none	0.50	0.43	0.47	1.08	
$(2)^1B_1$			3.00	2.82		3.97	0.02	b_1	0.56	0.34	0.35		
$(1)^1B_2$			4.55	4.36		5.91	-0.20	b_2	0.76	0.14	0.25		
$(2)^1B_2$			3.82	3.53		4.40	-0.11	b_1	0.41	0.35	0.31		
$(1)^1A_2$			2.41	2.47		3.35	-0.05	none	0.72	0.84	0.81		
$(2)^1A_2$			3.83	4.01		4.82	-0.17	b_1	0.77	0.80	0.80		
$(1)^3A_1$	4.01	4.27	4.00	4.79	4.61		-0.11	a_2,b_1,b_2	0.68	0.75	0.69	3.00	
$(1)^3B_1$	0.77[f]	0.71	[0.77]	[0.77]			-0.04	none	[0]	[0]	[0]	0.34	[0]
$(2)^3B_1$		2.47	2.70	2.05	1.21		-0.18	b_1,b_2	0.19		0.30	1.92	0.18
$(1)^3B_2$	3.81		4.02	3.59	4.18		-0.02	a_2,b_1	1.03	1.65	1.40		
$(2)^3B_2$	3.70		4.24	2.76	4.04		-0.16	b_1	0.63	0.81	0.39		
$(1)^3A_2$	2.38		2.28	1.7	2.91		-0.18	none	0.59	0.56	0.59		
$(2)^3A_2$			3.11	3.24			-0.25	a_2,b_1,b_2	0.41		0.48		
$(3)^3A_2$	4.48		4.47	5.5			-0.13	b_1	0.46	0.54	0.38		

[a] singlet states from $(1)^1A_1$ reference state, triplet states from $(1)^3B_1$ reference state. [b] Crude estimate based on DFT orbital energy differences at the $(1)^1A_1$ geometry added to the TDDFT energies of $(1)^1B_1$ and $(1)^3B_1$. [c] evaluated at HSE06 geometries optimized using DFT or TDDFT. [d] TDDFT except ΔSCF for $(2)^1A_1$. [e] EOM-CCSD for open-shell singlets else CCSD(T). [f] 0.72 eV using 2-ring structure Fig. 6.1e. [g] also imaginary for the 2-ring compound in Fig. 6.1e. [h] local minimum for 2-ring compound in Fig. 6.1e.

Normal-mode analyses were performed at all HSE06 excited-state structures optimized by TDDFT, with the nature of the optimized stationary points determined. Not all optimized structures are found to be local minima on the potential-energy surface, and the symmetry of modes found to break C_{2v} symmetry are listed in Table 6.5. These modes are mostly out of plane modes that lead to a variety of low-symmetry structures, with most acting to try to rejoin bonds to heal the defect. Most significantly, the lowest-energy state found at C_{2v} symmetry, $(1)^1A_1$, undergoes a displacement in a b_1 model leading to a structure of C_s symmetry with a HSE06 energy change of ΔE = -0.27 eV, followed by a second displacement to a C_1 symmetry (Fig. 6.1c) at ΔE = -1.39 eV. However, relaxation of $(2)^1A_1$ leads instead to a lower-energy structure at ΔE = -2.02 eV (Fig. 6.1d) that is the lowest-energy structure found by HSE06 for the model compound. In these structures, the molecular plane buckles to bring defect atoms close enough together to form bonds.

The chemical forces driving these transformations will also occur for V_NC_B defects in 2-D and 3-D materials but will be opposed by constraining forces coming from the h-BN layer

and the surrounding environment. In considering defect sites, in general, strong chemical forces of this nature will arise and the strength by which they are opposed will control the structural and spectroscopic properties of the defect. Optimization of 2-D layers containing the V_NC_B defect results in various states all of which display C_{2v} symmetry, indicating that in this case the restoring forces overpower the bond formation forces to lock in the defect. Under such circumstances, calculations on model compounds are best performed using the full symmetry of the 2-D material, as is done herein.

Some test calculations performed using the expanded 2-ring compound shown in Fig. 6.1e indicate that the $(2)^1A_1$ state becomes stable to both a_2 and b_1 distortions compared to the one-ring model, but even in the expanded system $(1)^1A_1$ remains unstable to b_1 distortion. How large a model compound needs to be thus remains a key question. In practical calculations on 2-ring models, it may be advantageous to freeze the outer ring atoms at their geometry extracted from a periodic model.

Another feature of note is that real 2D monolayers are subject to buckling that is not represented in small-scale periodic models (e.g., Fig. 6.1a). How such buckling interacts with the restorative chemical forces will always be a question of interest concerning defect modeling. Nevertheless, a consequence of the action of restoring forces is that the wide variation in the quality of DFT results as a function of geometry reported for the one-ring model compound in Table 6.3 will be reduced somewhat. As the reference structure used in the calculations reported in Tables 6.1 and 6.2 is typical of that found in other defects [200], I anticipate that the perceived errors in DFT found at this structure will be typical of what could be expected in general applications to defect spectroscopy.

How the chemical forces act to heal the defect in its various electronic states is revealed through measurements of photoabsorption and photoluminescence spectra. To model such spectra, calculations need to properly represent both these forces and the restoring ones operating in 2-D and 3-D structures.

While high-resolution spectra provide detailed information concerning the motion of all atoms, the width of the spectral band alone provides the most important qualitative information, specifying the reorganization energy associated with the transition. Large atomic motions in high-frequency modes results in broad bands; alternatively, if the bonding is insensitive to nuclear motion, then the spectra will be sharp. Broad spectra are also produced

if orbitals from the valence or conduction bands of the h-BN are involved as interactions within these bands create a multitude of electronic transitions out of a single one. Sharp transitions are typically easier to observe and hence dominate experimental studies. Amongst defects, there is a search for those that have defect orbitals lying within the bandgap that have allowed spectroscopic transitions [200]. Photoluminescence usually becomes the focus as it easier to observe than photoabsorption as defects are usually present only in low concentration, with an added bonus often arising if the emitting state is different to the absorbing state and has different symmetry such that the absorption and emission polarizations vary [75].

Using the harmonic-oscillator approximation to the ground-state and excited-state potential-energy surfaces, the reorganization energy λ corresponds to the difference between the average absorption frequency and ZPL. It is specified by

$$\lambda = h\nu_{00} - \frac{\int h\nu\sigma(\nu)d\nu}{\int \sigma(\nu)d\nu} \qquad (6.1)$$

Table 3 compares results from TDDFT (HSE06 and CAM-B3LYP functionals) with those form EOM-CCSD (singlet states) and CCSD(T) (triplet states) for the bandwidths of photoabsorption spectra originating from either $(1)^1A_1$ or $(1)^3B_1$. These widths are given as the reorganization energies λ calculated as the energy change of the excited state in going from its adiabatic minimum-energy geometry to that when vertically excited from the ground state. This corresponds to the second moment of observed absorption spectra. In the harmonic approximation to the ground-state and excited-state potential energy surfaces, if the form of the normal modes does not change then the bandwidth for photoemission corresponds to that for photo-absorption, a commonly good approximation in molecular spectroscopy but one that can also fail badly, e.g., for chlorophylls [208,209]. In practice, reorganization energies become susceptible to vibronic coupling effects that can dramatically change the shapes of excited-state potential-energy surfaces. This occurs as the influence of vibronic coupling depends strongly on the energy gaps between excited states, demanding global accuracy across the excited state manifold if computational methods are to satisfactorily predict absorption and emission bandwidths [210].

The results presented in Table 6.5 show wide variations between reorganization energies calculated using HSE06 and either EOM-CCSD/CCSD(T) or CAM-B3LYP. Small numbers occur whenever the singlet/triplet excited state has a similar geometry to the singlet/triplet ground state. For $(2)^1B_2$, the difference is stark: 0.76 eV for HSE06 vs. 0.25 eV

for CAM-B3LYP and 0.14 eV for EOM-CCSD, indicating that the vibronic environments of this state is being perceived very differently by HSE06. For $(1)^3B_2$, HSE06 deviates by the same magnitude but opposite sign, with the largest deviation for HSE06 being 0.9 eV for $(2)^1A_1$. For HSE06, averaging 12 states gives an error of 0.06±0.38 eV whereas for CAM-B3LYP this is only -0.07±0.14 eV.

Most significantly, agreement between all 3 methods within 0.1 eV is found for the low-energy states $(1)^1B_1$, $(2)^3B_1$, and $(1)^3A_2$ of greatest relevance to the interpretation of observed PL spectra [200]. Further, the neglect of restoring forces in these calculations on a model cluster means that the calculated reorganization energies and their sensitivities to the global details of the electronic structure will be overestimated. To explore these effects, HSE06 reorganization energies calculated for the 2-D material are also shown in Table 6.5. For $(2)^3B_1$, the model compound and the 2-D material have reorganization energies of 0.19 eV and 0.18 eV, respectively, indicating the similarity of the chemical properties of these two model systems.

Insight into the difficulties in modelling the widths of higher-energy transitions comes from noting that, for $(2)^1A_1$, the 2-D material has a large HSE06 reorganization energy of 1.15 eV, indicating that strong chemical forces come into play, but in the model compound this increases to 3.32 eV! Understanding the shapes of excited-state potential-energy surfaces comes down to understanding the conical intersections that these surfaces have with other surfaces. The nature and location of these conical intersections are controlled by subtle differences in energy gaps and state orderings [210,211]. A serious problem with GGA density functionals like PBE and hybrid functionals like HSE06 is that they are incorrect in the asymptotic limit [212]. The error in the asymptotic potential is state dependent and adds to the transition energy, with errors becoming large when significant charge-transfer occurs during an electronic transition. In general, excited-state charge-transfer band energies are predicted to be much too low in energy compared to the charge-neutral states, with this effect having severe consequences as the transition energy increases. Consequences include the prediction by GGA and hybrid functionals that polyacetylene has a triplet ground state [41], as well as their inability to describe the spectra of porphyrins, chlorophylls, and other systems allowing for extensive charge transfer [41]. Movement of charge to/from defect sites can indeed induce significant long-range charge transfer and so defect sites are susceptible to it. Functionals like CAM-B3LYP correct for the errors in the asymptotic potential and hence do not suffer from

the chaos that sets in at (nominally) high energies when GGA or hybrid functionals are used, allowing spectral properties of charge-transfer systems to be determined using DFT [42,43].

I conclude this section on the following note: Hybrid functionals like HSE06 work very well for excitations within the triplet manifold of the V_NC_B defect, with an accuracy equivalent to or perhaps exceeding the accuracy of the ab initio methods used. However, HSE06 underestimates triplet state energies by on average 0.7 eV compared to closed-shell singlet states, while open-shell singlet states are predicted to be too low in energy by 1.0 eV. Since V_BC_N has a triple ground state and, as discussed for triplets, HSE06 work well, therefore I tentatively assign the correction factors deduced for V_NC_B for closed and open shell singlets to V_BC_N to save the computational time. The level structures of both V_NC_B and V_BC_N with the correction factors applied are discussed in Chapter 7. In the next section, I benchmark the excited states of V_NN_B.

6.2 Benchmarking the excited states of V_NN_B

In this section, the spectroscopy of the V_NN_B defect in h-BN is studied in detail. V_NN_B could, in principle, account for the observed emission if it existed naturally in h-BN in either its neutral, cationic, or anionic forms. The recent experimental evidence showing insensitivity of the spectra to external Stark effects, coupled with extreme shifts of 1 eV found in different h-BN centres, seems difficult to reconcile, but one possibility is that the defect actually involves two oppositely charged defects that are closely paired. This puts focus on the possibility that one or more charged V_NN_B defects could be involved.

Two other observed properties of the spectra of h-BN defects are also relevant to the assessment of proposed defect sites. As discussed earlier, polarized in-plane emission is observed after in-plane polarized light absorption, but the absorption can be either polarized parallel or else in-plane at some angle, e.g., 60° [75]. In principle, this could arise following, for one polarization, Franck-Condon allowed [91] transitions, and for the other polarization, Herzberg-Teller-allowed [92] vibronic transitions, all within the same electronic state [93]. However, the wide and variable energy spacing between the absorptions of different polarization imply that instead two states are involved, supporting Franck-Condon allowed, differently polarized, in-plane absorptions. This places strict requirements on the properties of defect states, especially those that are nominally of high symmetry such as V_NN_B.

In its most symmetric form, V_NN_B would display C_{2v} symmetry, with all spectroscopic processes then restricted to those that this symmetry allows. Using the standard axis conventions for planar molecules [94,95], the irreducible representations of the C_{2v} point group are a_1 and b_2 (of σ type) and b_1 and a_2 (of π type). Electronic excitations of A_1 symmetry are polarized in-plane along the defect C_2 axis, while those of B_2 symmetry are polarized in-plane orthogonal to this and allowed out-of-plane transitions have B_1 symmetry. Hence the observed properties demand of V_NN_B that its two lowest transitions be of A_1 and B_2 symmetry. Either spectral overlap of the two states, or else vibronic coupling between them, could modify the expected C_{2v}-based pure orthogonal polarization of the second state into some mixed polarization, accounting for the observed 60°-polarized absorption [75].

Second, the observed emission is very sharp with strong ZPL and weak PSB's, indicating that the emitting excited state has almost the same geometry as does the ground state. This effect can be quantified by determining the spectral reorganization energy from observed spectra. Some representative spectra [75,200] are shown in Fig. 6.3. Using the harmonic-oscillator approximation to the ground-state and excited-state potential-energy surfaces, the reorganization energy λ (Eq. 6.1) corresponds to the difference between the average absorption frequency and the spectroscopic origin. Assuming that absorption and emission spectra are symmetric, the same reorganization is expected in emission as in absorption. It is sensitive to assumptions made concerning the baseline, the availability of the slow vibrational band structure, and isolation from interfering spectra. For a typical Group-1 emitter (Jungwirth and Fuchs [75] Fig. 2b), reproduced in Fig. 6.3a, this yields $\lambda = 1400\ cm^{-1} = 0.17$ eV; slightly larger values are also feasible based on variations in the apparent emission baseline and the low-frequency cutoff for the integration. However, for the Group-2 emitter shown in Fig. 6.3b (Tawfik et al. [200], Fig 3(b)), λ reduces to 0.09 eV, with other examples returning values as low as 0.04 eV. All of the numbers are very small, given that calculated reorganization energies for proposed h-BN defects can be as large as 2 eV.

Note that only the emitting state is required to have such a low reorganization energy. This state presumably corresponds to the lowest-energy of the two orthogonally polarized states to which absorption occurs, but in principle, the higher-energy state could have a much larger reorganization energy. Detailed mapping of fluorescence excitation spectra would allow the absorption reorganization energies of both states to be measured.

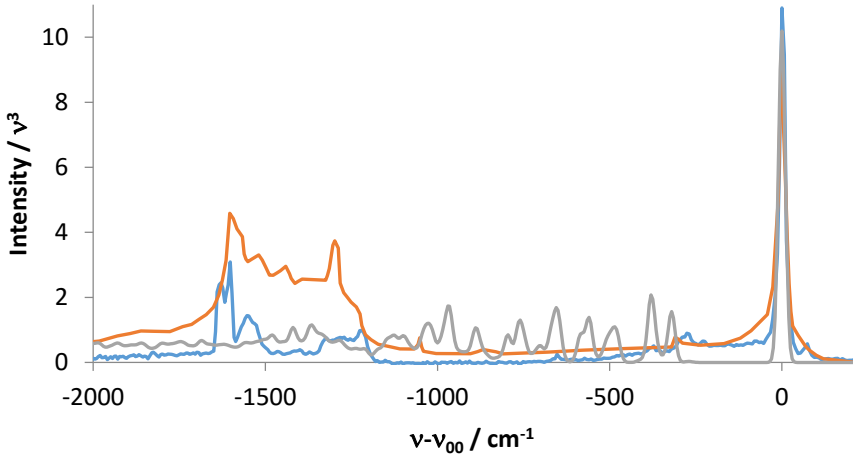

Figure 6.3 Some of the observed emission spectra [75,200] of defect sites in h-BN used to estimate reorganization energies λ: (a) red- from Jungwirth and Fuchs [75], λ = 0.17 eV, (b) blue- from Tawfik et al. [200], λ = 0.09 eV, and (c) green- simulated for the $(2)^1A_1 \rightarrow (1)^1A_1$ calculated transition of $V_NN_B^{-1}$, λ = 0.11 eV.

To date, calculations have only been performed considering neutral V_NN_B defects [123]. A critical result was the prediction that the ground-state of this defect distorts out of plane via a mode of b_1 symmetry [123]. Using the present computational methods, I predict that the depth of the associated double-well is 0.05 eV. While this result seems small, the well is deeper than the zero-point vibrational level and hence it is indicative of significant geometrical distortion. Naively [210,213], this distortion would add four times the well depth, or 0.2 eV, to the reorganization energy of any transition involving a planar excited state; in most circumstances, this contribution would be expected to be much more for a transition to any non-planar excited state. In either case, this contribution would make the state out of the realms of feasibility for accounting for the observed h-BN spectra, given that observed total reorganization energies range from 0.04 – 0.17 eV (see Fig. 6.3).

To put his result in context, one must be able to estimate the reliability of the computational predictions-are these results expected to be robust. They depend on how accurately a computational method is likely to be able to describe conical-intersection seams amongst the excited-state manifold, a complex property indeed. Of relevance, it is found that for the V_NC_B defect, errors of many eV can be made using standard approaches to estimate excited state energies and the reorganization energies associated with their in-plane and out-of-plane relaxations [82]. These errors were extremely dependent on the nature of the state considered. One conclusion from the V_NC_B work [82] is that it is difficult to estimate computational uncertainties by considering just a single state; rather one should consider properties of the excited state manifold, focusing on states of analogous type to the state of

greatest interest. Considering the excited-state manifold will also allow other independent criteria to be used in judging the suitability of any proposed state.

Most investigations are best performed constraining the system to high symmetry, in this case C_{2v}, as this provides a broad qualitative overview and makes calculations much easier [11,78,124,200,214]. The geometrical structure of the V_NN_B [22,32,200] defect in the considered model compound and periodic lattice are depicted in Fig. 6.4a and Fig. 6.4b, respectively.

The model compound shown in Fig. 6.4a has one ring of h-BN atoms surrounding the defect. A similar approach adopted for V_NC_B [82] has proven to be adequate for benchmarking. However, cluster results approach those for 2D samples only slowly as the cluster size is increased [82], and both cluster models and small periodic models like that shown in Fig. 6.4 will not be able to include long-range screening effects to any charge-transfer band energies arising from the somewhat unique nature of infinite 2D materials [215].

The basic electronic orbital structure of V_NN_B has been discussed elsewhere [214], with the key features being generically characteristic of most h-BN defects in C_{2v} symmetry: at each defect site, one σ and one π orbital produce dangling bonds. For the case of neutral V_NN_B, five electrons need be distributed in these six orbitals, reducing to four for $V_NN_B^{+1}$ but increasing to six for $V_NN_B^{-1}$. The three σ atomic defect orbitals combine to make molecular orbitals that are represented in Fig. 6.5, one of an apparently "bonding" nature (named $1a_1$), one of a "non-bonding" nature (named $2a_1$), and one of an "antibonding" nature (named b_2). Similarly, the three π orbitals combine to make the orbitals $1b_1$, $2b_1$, and a_2, respectively. The "bonding" orbitals are typical of 3-center 2-electron bonds but the interatomic distances are so large that in reality no bond exists (Fig. 6.5), and it is this feature that DFT methods find difficult to accurately model [38,82]. I find that $1a_1$ lies below the valence-band (VB) maximum of h-BN and so is always doubly occupied, $2a_1$, $1b_1$ and then $2b_1$, shown pictorially in Fig. 6.5, fall in the VB to conduction band (CB) gap becoming the primary focus of attention, while a_2 and b_2 fall inside the CB. Transitions amongst these orbitals dominate the low-energy spectroscopy of the defect, with transitions involving orbitals localized within the h-BN valence-conduction band gap being the most likely ones for producing sharp absorption and emission spectra. I consider up to 14 electronic states for neutral V_NN_B, 13 for $V_NN_B^{+1}$, and 13 for $V_NN_B^{-1}$. These states are listed in Table 6.6 in terms of their dominant configuration in terms of the key defect, valence-band (V), and conduction band (C) orbitals.

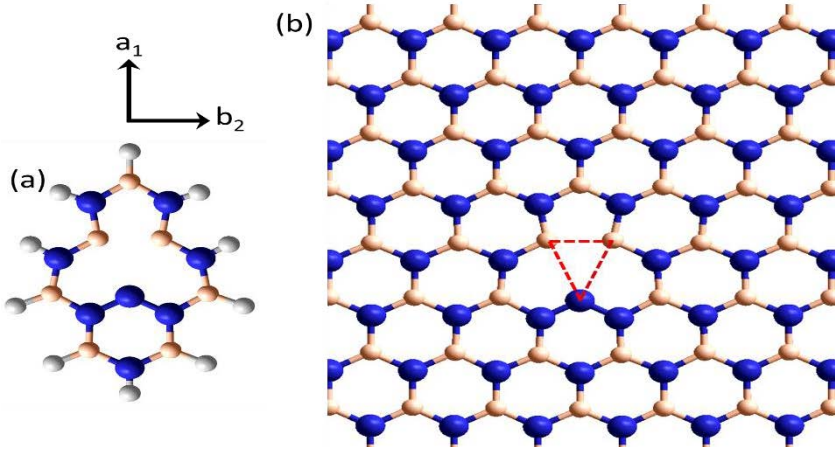

Figure 6.4 The geometrical structure of the V_NN_B defect, in which a nitrogen vacancy is neighbored by a nitrogen substituting boron, is represented as either (a) a model compound constrained to C_{2v} symmetry or (b) a rectangular (6 x 4√3)R30° unit cell representing a periodic 2D lattice of such defects; N- blue, B- peach, H- white. Allowed in-plane spectroscopic transitions may be polarized along the indicated a_1 and b_2 axes, while b_1 transitions are polarized out-of-plane and a_2 transitions are forbidden. Dashed red lines indicate defect B-B distances of 1.92 Å and 2.53 Å, respectively, for its $(1)^2B_1$ ground state, both much larger than the BN bond length of 1.44 Å.

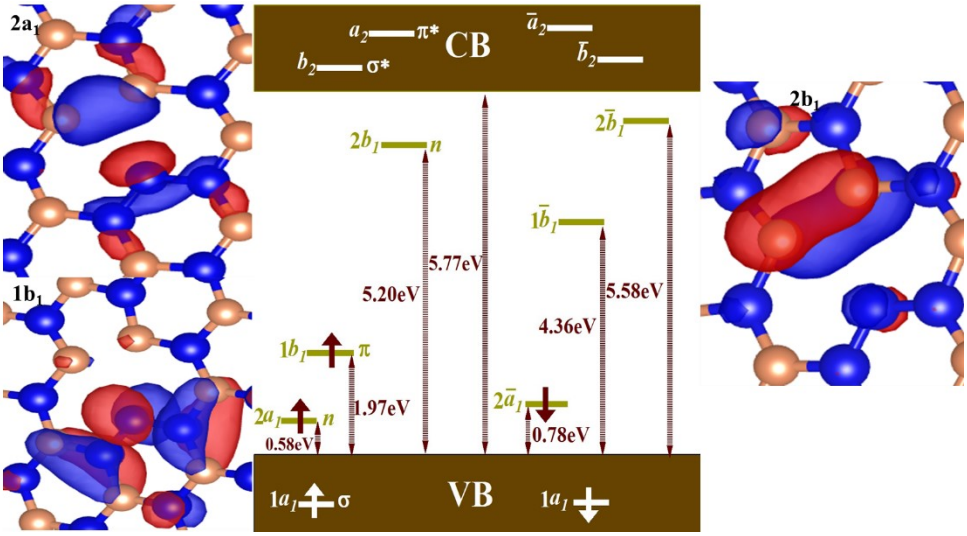

Figure 6.5 Shown for the example of neutral V_NN_B in 2D h-BN are: (central) defect orbitals localized within the h-BN valence-conduction band gap, and (flanks) key DFT orbitals from the $(1)^2B_1$ ground-state electronic structure of V_NN_B, constrained to planar C_{2v} symmetry.

Table 6.6 Considered state symmetries, their dominant orbital occupancies, and their transition polarizations from the ground state.

	State	Trans. pol.[a]	Dominant orbital occupancy																Spin comp.[b]
			V_{2a1}	V_{2b1}	V_{1a1}	$1a_1$	V_{2a2}	V_{1b1}	$2a_1$	V_{1a2}	$1b_1$	$2b_1$	C_{1a2}	C_{2a2}	C_{b1}	C_{1a1}	C_{2a1}	C_{b2}	
V_NN_B	$(1)^2B_1$	-	2	2	2	2	2	2	2	2	1	0	0	0	0	0	0	0	
	$(2)^2B_1$	A_1	2	2	2	2	2	2	2	2	0	1	0	0	0	0	0	0	
	$(1)^2A_1$	B_1	2	2	2	2	2	2	1	2	2	0	0	0	0	0	0	0	
	$(1)^2A_2$	B_2	2	2	2	2	2	2	2	2	0	0	1	0	0	0	0	0	
	$(2)^2A_2$	B_2	2	2	2	2	2	2	2	1	2	0	0	0	0	0	0	0	
	$(2)^2A_1$	B_1	2	2	2	2	2	2	1	2	1	1	0	0	0	0	0	0	D3
	$(3)^2A_2$	B_2	2	2	2	2	2	2	2	1	1	1	0	0	0	0	0	0	D3
	$(4)^2A_2$	B_2	2	2	2	2	2	2	2	2	0	0	0	1	0	0	0	0	
	$(1)^4A_1$	-	2	2	2	2	2	2	1	2	1	1	0	0	0	0	0	0	
	$(3)^2B_1$	B_1	2	2	2	2	2	2	2	2	0	0	0	0	1	0	0	0	
	$(3)^2A_1$	A_1	2	2	2	2	2	2	1	2	1	1	0	0	0	0	0	0	D1
	$(5)^2A_2$	A_2	2	2	2	2	2	2	2	1	1	1	0	0	0	0	0	0	D1
	$(4)^2A_1$	A_1	2	2	2	2	2	2	2	2	0	0	0	0	0	1	0	0	
	$(6)^2A_2$	A_2	2	2	2	2	2	2	2	0	2	0	1	0	0	0	0	0	
$V_NN_B^+$	$(1)^1A_1$	-	2	2	2	2	2	2	2	2	0	0	0	0	0	0	0	0	
	$(1)^1B_2$	B_2	2	2	2	2	2	2	2	1	1	0	0	0	0	0	0	0	S
	$(1)^1B_1$	B_1	2	2	2	2	2	2	1	2	1	0	0	0	0	0	0	0	S
	$(2)^1A_1$	A_1	2	2	2	2	2	1	2	2	1	0	0	0	0	0	0	0	S
	$(2)^1B_1$	B_1	2	2	1	2	2	2	2	2	1	0	0	0	0	0	0	0	S
	$(2)^1B_2$	B_2	2	2	2	2	1	2	2	2	1	0	0	0	0	0	0	0	S
	$(3)^1B_1$	B_1	1	2	2	2	2	2	2	2	1	0	0	0	0	0	0	0	S
	$(3)^1A_1$	A_1	2	1	2	2	2	2	2	2	1	0	0	0	0	0	0	0	S
	$(1)^3B_1$	-	2	2	2	2	2	2	1	2	1	0	0	0	0	0	0	0	
	$(1)^3B_2$	A_2	2	2	2	2	2	2	2	1	1	0	0	0	0	0	0	0	
	$(1)^3A_1$	B_1	2	2	2	2	2	1	2	2	1	0	0	0	0	0	0	0	
	$(2)^3B_2$	A_2	2	2	2	2	1	2	2	2	1	0	0	0	0	0	0	0	
	$(2)^3B_1$	A_1	2	2	2	1	2	2	2	2	1	0	0	0	0	0	0	0	
	$(2)^3A_1$	B_1	2	2	2	2	2	2	2	1	2	0	1	0	0	0	0	0	
$V_NN_B^-$	$(1)^1A_1$	-	2	2	2	2	2	2	2	2	2	0	0	0	0	0	0	0	
	$(1)^1B_2$	B_2	2	2	2	2	2	2	2	2	1	0	1	0	0	0	0	0	S
	$(2)^1A_1$	A_1	2	2	2	2	2	2	2	2	1	1	0	0	0	0	0	0	S
	$(1)^1B_1$	B_1	2	2	2	2	2	2	2	2	1	0	0	0	0	1	0	0	S
	$(1)^1A_2$	A_2	2	2	2	2	2	2	2	2	1	0	0	0	1	0	0	0	S
	$(2)^1B_1$	B_1	2	2	2	2	2	2	2	2	1	0	0	0	0	0	1	0	S
	$(2)^1B_2$	B_2	2	2	2	2	2	2	2	2	1	0	0	1	0	0	0	0	S
	$(1)^3A_1$	-	2	2	2	2	2	2	2	2	1	1	0	0	0	0	0	0	
	$(1)^3B_2$	B_2	2	2	2	2	2	2	2	2	1	0	1	0	0	0	0	0	
	$(1)^3B_1$	B_1	2	2	2	2	2	2	2	2	1	0	0	0	0	1	0	0	
	$(2)^3B_2$	B_2	2	2	2	2	2	2	2	2	1	0	0	1	0	0	0	0	
	$(2)^3A_1$	A_1	2	2	2	2	2	2	2	2	1	0	0	0	1	0	0	0	
	$(1)^3A_2$	A_2	2	2	2	2	2	2	2	2	1	0	0	0	0	0	0	1	

[a]: A_1 transitions are polarized in-plane along the symmetry axis, A_2 transitions are forbidden, B_1 transitions are polarized perpendicular to the layer, while B_2 transitions are polarized in plane and orthogonal to the symmetry axis. Transition symmetries to/from the lowest-energy state of each spin multiplicity and ionization level are listed.

[b]: Spin components for open-shell calculations not satisfying the Gunnarsson-Lundqvist theorem [163]: S- singlet energy from Eqn. (3), D3 and D1- tripdoublet and singdoublet energies from Eqn. (6).

While TDDFT methods allow for the first-principles determination of all of the excited states listed in Table 6.6, more computationally feasible approaches, especially for 2D materials, involve the direct solution of the DFT equations with the electron occupation

constrained to match the dominant configurations listed in the table i.e. ΔSCF method [181]. This approach is well defined for the lowest-energy state of each possible spatial symmetry for the highest spin multiplicity available for any set of open-shell orbitals [163].

For neutral V_NN_B, the states $(2)^2A_1$, $(3)^2A_1$, $(3)^2A_2$ and $(5)^2A_2$ listed in Table 6.6 involve three unpaired electrons in three different orbitals, with the spin multiplicity (doublet) being less than the highest-possible value (quartet). For each of these, 8 determinants contribute to the various states involved, as sketched in Fig. 6.6a. Four determinants, named 1a-4a, have more spin-up electrons than spin-down ones, while the others named 1b-4b, are symmetrically equivalent determinants obtained by interchanging spin-up and spin-down. In the absence of an applied magnetic field, the two sets of determinants have equal energies and are non-interacting, meaning that just one set, here taken as 1a-4a, need be explicitly considered in most discussions. The 8 determinants depict 3 electronic states, one quartet state with four spin components, and two doublet states each with two spin components. Within a state, all spin components have the same energy. Two components 1a and 1b of the quartet state are immediately apparent in Fig. 6.6a, but the other two components and all components of the doublet states arise from complex linear combinations of determinants 2a-4a and 2b-4b.

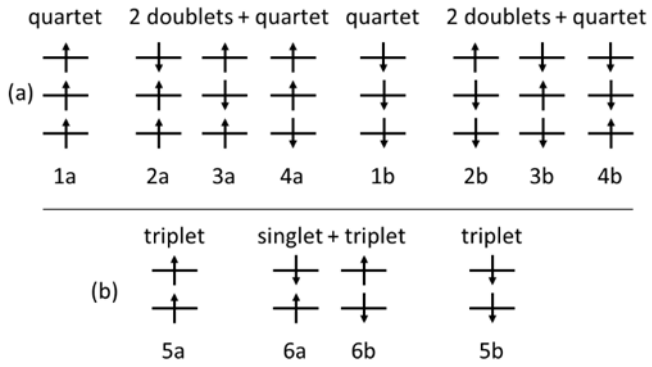

Figure 6.6 Possible occupancies (a) when 3 unpaired electrons distribute into 3 orbitals (resulting in two doublet states and one quartet), and (b) when 2 unpaired electrons distribute into 2 orbitals (resulting in one singlet state and one triplet).

Determining energies for this type of state involves severe challenges to DFT as it involves strong static electron correlation, something not provided for by the Kohn-Sham theorem [206] or its enhancement to non-singlet states, the Gunnarsson-Lundqvist theorem [163]. Determinants 1a and 1b decouple from the others and satisfy the Gunnarsson-Lundqvist theorem, meaning that DFT calculations setting these occupancies return properties that correspond to physical observables, properties of the quartet state. However, the other determinants are strongly coupled and have no first-principles relationship to observables. In

multi-configurational DFT approaches [215,216] (MC-DFT), empirical schemes are devised that facilitate use of these states in calculations of observable properties. They are designed to be universal approaches that show consistency with DFT treatment of dynamical electron correlation. However, such approaches are under development and are currently not available for application to defect-site spectroscopy.

This situation also arises in DFT descriptions of systems involving two unpaired electrons in two orbitals (Fig. 6.6b), as occurs during allowed optical excitations from closed-shell ground state molecules and materials (see Table 6.6 for examples involving V_NN_B ions). It also is involved in antiferromagnetic couplings in molecules and materials. As Fig. 6.6b shows, four determinants can be constructed depicting one singlet state and one triplet state. Determinants 5a and 5b each have two electrons of the same spin and so provide easy computational access to the properties of the triplet state. In contrast, determinants 6a and 6b with one electron of each spin do not satisfy the Gunnarsson-Lundqvist theorem and need to be coupled together to make singlet and triplet state components. Ignoring dynamic electron correlation between these electrons and the others, the energy of the mixed-spin determinants must be the average of the energies of the triplet and singlet states:

$$E_S + E_T = E_{6a} + E_{6b} \qquad (6.2)$$

where E_S and E_T are the observable energies of the singlet and triplet states, while E_{6a} and E_{6b} are the energies coming from DFT calculations made by setting occupancies to correspond to each individual determinant. As $E_{6a} = E_{6b}$ in the absence of a magnetic field, and as the Gunnarsson-Lundqvist theorem yields $E_T = E_{5a} = E_{5b}$, this allows the singlet state energy to be approximated by

$$E_S = 2E_{6a} - E_{5a} \qquad (6.3)$$

Such an approach could be thought of as being the simplest-possible empirical MC-DFT scheme. When considering antiferromagnetic interactions in materials, the electrons being correlated are typically large distances apart making dynamical electron correlation small, and this approximation has successfully led to vary many important results in the field. In defects, the neglect of dynamic electron correlation is questionable, but I have found that in V_NC_B model compounds, the associated errors are small compared to the accuracy required in order to make qualitative assignment of defect properties [82]. While gradients for geometry

optimizations should be taken from E_S, instead I simply optimize E_{6a} and then apply the correction from Eqn. (6.3) as the computations are much more likely to complete successfully.

An analogous approach applied to the case of three electrons in three orbitals is insufficient to convert calculated properties into experimental observables, however. This is because two doublet states and one quartet arise from the 8 calculable determinants, whereas only one equation is available that links them. This equation, like before, conserves the total energy (trace of the Hamiltonian matrix) for the states:

$$E_{D1} + E_{D3} + E_Q = E_{2a} + E_{3a} + E_{4a} = E_{2b} + E_{3b} + E_{4b} \qquad (6.4)$$

where E_{D1}, E_{D3}, and E_Q are the physically observable energies of the two doubled states and the quartet state, respectively, in the absence of a magnetic field. The labels "D1" and "D3" indicate singlet-coupled "singdoublet" and triplet-coupled "tripdoublet" states, respectively [217]. As the Gunnarsson-Lundqvist theorem yields $E_Q = E_{1a} = E_{1b}$, this allows the average energy of the two doublet state to be approximated by

$$E_{D1} + E_{D3} = E_{2a} + E_{3a} + E_{4a} - E_{1a} \qquad (6.5)$$

Performing standard DFT calculations on the single determinants in Fig. 6.6a therefore cannot reveal the energies of the two doublet states, only their average. TDDFT calculations explicitly embody all terms in a first-principles way and hence do not suffer from this problem, but they are currently not feasible to apply to large periodic solids containing defects. Hence, I proceed by evaluating the energy splitting ∇E_{D1D3} using TDDFT calculations for the model compound, applying this to ΔSCF calculations for both it and the analogous state in the 2D defect model. The state energies are then approximated by:

$$E_{D3} = (E_{2a} + E_{3a} + E_{4a} - E_{1a} - \nabla E_{D1D3})/2$$

$$E_{D1} = (E_{2a} + E_{3a} + E_{4a} - E_{1a} + \nabla E_{D1D3})/2 \qquad (6.6)$$

Table 6.7 shows all of the quantities required to evaluate the energies of tripdoublet and singdoublet state pairs $(2)^2A_1$ and $(3)^2A_1$ (singly occupied orbitals $1a_1$, $1b_1$, and $2b_1$), as well as for the pairs $(3)^2A_2$ and $(5)^2A_2$ (singly occupied orbitals V_{1a2}, $1b_1$, and $2b_1$). The approximation

$$E_{D3} \approx \min(E_{2a}, E_{3a}, E_{4a}) \qquad (6.7)$$

provides an uncontrolled upper bound to the state energy. It has previously been applied to consider properties of $(2)^2A_1$ for the 2-D material using HSE06 [73], yielding results close enough to those from Eqn. (6.6) that are hence useful for assigning observed defect spectroscopy. Such an approach needs to be applied with extreme caution, however.

Gradients for geometry optimization should be taken from E_{D3} or E_{D1}. However, I take the simpler approach of optimizing the three individual configuration energies E_{2a}, E_{3a}, and E_{4a}, applying Eqn. (6.6) after the optimizations complete. This yields three different approximations for the state energies E_{D3} or E_{D1} and their associated optimized geometries. I find that the different results are all in good agreement, suggesting that this approach is successful, showing the minimum energy obtained at any geometry in Table 6.7. The same interpretations of ΔSCF calculations are applied independent of whether the calculations are performed on the model compound or on the 2D material.

Table 6.7 Energies of the singdoublet state E_{D1}, tripdoublet state E_{D3}, and quartet state E_Q extracted from combinations (Eqn. 6.4) of energies determined for single-configurational wavefunctions specified in Fig. 6.6, E_{1a}, E_{2a}, E_{3a}, and E_{4a}. Geometries are obtained by optimizing the energy of the single determinants only, with the final results for the singdoublet and tripdoublet states taken to be those for the minimum found at the three structures.

geometry	energy	$(2)^2A_1$ and $(3)^2A_1$				$(3)^2A_2$ & $(5)^2A_2$			
		model		2D		model		2D	
		PBE	HSE06	PBE	HSE06	PBE	HSE06	PBE	HSE06
2a	E_{2a}	3.62	4.34	2.85	3.37	3.79	4.80	3.77	4.47
	E_{3a}	3.66	5.37	2.78	3.40	4.08	5.77	4.04	5.16
	E_{4a}	3.72	4.52	2.89	3.64	4.49	4.70	4.03	5.19
	$E_Q = E_{1a}$	3.28	3.97	2.46	2.95	3.97	5.17	3.75	4.42
	E_{D1D3}	0.66	0.50	0.66	0.50	0.10	0.60	0.10	0.60
	E_{D3}	3.53	4.88	2.70	3.48	4.15	4.75	4.00	4.90
	E_{D1}	4.19	5.38	3.36	3.98	4.25	5.35	4.10	5.50
3a	E_{2a}	3.62	5.21	3.03	3.39	3.80	4.92	3.79	4.55
	E_{3a}	3.65	4.22	2.78	3.38	4.40	5.73	4.02	4.99
	E_{4a}	3.72	4.32	2.89	3.64	4.16	4.97	4.01	5.08
	$E_Q = E_{1a}$	3.28	3.57	2.47	2.96	3.74	5.18	3.77	4.51
	E_{D1D3}	0.66	0.50	0.66	0.50	0.10	0.60	0.10	0.60
	E_{D3}	3.53	4.84	2.79	3.48	4.26	4.92	3.98	4.76
	E_{D1}	4.19	5.34	3.45	3.98	4.36	5.52	4.08	5.36
4a	E_{2a}	3.71	4.70	2.85	3.49	3.69	5.03	3.79	4.56
	E_{3a}	3.62	4.24	2.79	3.53	4.40	6.04	4.02	5.04
	E_{4a}	3.66	4.31	2.89	3.68	4.01	4.35	4.01	5.08
	$E_Q = E_{1a}$	3.28	3.55	2.46	3.06	3.94	5.47	3.77	4.52
	E_{D1D3}	0.66	0.50	0.66	0.50	0.10	0.60	0.10	0.60
	E_{D3}	3.53	4.60	2.71	3.57	4.03	4.68	3.98	4.78
	E_{D1}	4.19	5.10	3.37	4.07	4.13	5.28	4.08	5.38
Final	E_{D3}	3.53	4.60	2.70	3.48	4.03	4.68	3.98	4.76
	E_{D1}	4.19	5.10	3.36	3.98	4.13	5.28	4.08	5.36

6.2.1 New methods for determining defect excited state geometries and energies using VASP.

Many of the states listed in Table 6.6 involve orbital occupancies that differ from Fermi distribution or Aufbau distribution produced by default in VASP. To access such states, VASP implements the “FERDO” and “FERWE” commands that allow the occupation of each spin orbital to be individually set. These settings apply to not only the initial wavefunction but also to all subsequent wavefunctions obtained during the SCF procedure, as well as during geometry

optimization. As they are not updated to match the changing nature of the orbitals during these procedures, extreme care needs to be taken using this approach to ensure that the calculation converges to the desired electronic state.

To help with this, VASP allows the "LDIAG = FALSE" command to be used to override the default ("LDIAG = TRUE") protocol to ensure that the final wavefunction has similar form to the starting wavefunction. However, the wavefunction so produced becomes distorted and the energy reported is not actually the true energy for that wavefunction. As a result, VASP results can be misleading, as for the case of the V_NN_B defect in h-BN where the second excited state was missed entirely [73]. Also, states can appear normal both in terms of their electronic and geometric structure, yet are really just unconverged mimics of lower-energy states [82].

A software is developed in the present work that allows VASP to be automatically controlled and its output analyzed to produce a mostly reliable computational method. The centerpiece in this involves the processing of the VASP "WAVECAR" file to determine the point-group symmetry of each orbital of each spin. This embodies code taken from a MRCI package based on semi-empirical HF theory [217,218]. The wavefunctions are first transformed from their intrinsic momentum-representation into the position-space representation using WaveTransPlot [219]. Standard projection methods are then applied to determine the symmetry operators and hence the point group that underpins the space or plane group of the 2D or 3D sample considered. Poorly converged wavefunctions may be identified and rejected based on the accuracy with which they depict expected symmetry relationships.

Besides plotting of the orbitals, another feature of this code is that it can form the overlap between the wavefunction calculated at one state and geometry with that obtained for another state and/or geometry. Wavefunctions for different states at the same geometry must be orthogonal. States that VASP may converge using the "LDIAG = FALSE" option that may just be misrepresented versions of lower-energy states can be readily recognized by their strong overlap with the lower-energy state. In principle, any high-energy state that display non-zero overlap with a lower energy state of the same spin and symmetry occupancy can, as the SCF procedure proceeds, transform smoothly to the lower-energy state. Most of the time, the standard termination conditions of the SCF loop in VASP stop the procedure well before such a transformation occurs, giving excited states having little overlap with lower-energy states. However, I did find some states for which the adiabatic transformation proceeded too quickly, making the desired state inaccessible (e.g., $(2)^1B_2$ for $V_NN_B^{-1}$, see later in Table 6.12). While

the computational procedure does not guarantee that all desired states can be found, it provides full knowledge of the properties of any state that is actually optimized.

Armed with this facility, the second program is used to control VASP calculations. Its input is the description of the excited state in terms of spin and symmetry dependent orbital occupancies. Table 6.6 lists the inputs required to generate optimized states for $V_N N_B^{-1}$ and $V_N N_B^{+1}$.

A starting WAVECAR file is required to run the procedure. This may be obtained in many ways, setting orbital occupancies for any state that may be useful; it does not have to depict the state of final interest. The program first runs a cycle of "LDIAG = FALSE" calculations, to set the desired state, followed by "LDIAG = TRUE" calculations, to get a realistic energy for that state. Each time through this loop, the FERDO and FERWE inputs are set to reflect the current WAVECAR file. This procedure is terminated either when the "LDIAG= TRUE" calculation delivers the required state, or else the wavefunction diverges to something unphysical. Indeed, states of very high multiplicity and open-shell character can result from this procedure. While their energies seem to be a few eV higher than typical states of interest, that this can happen indicates the extremely complex nature of the excited-state manifold of defects. Failure of the procedure to converge demands that a new starting wavefunction, or, if possible, geometry, is found.

If geometry optimization is required, it is then commenced. During this, "LDIAG = FALSE" is used to ensure that the calculations always refer to the desired state. However, the wavefunction at the end of this procedure will be distorted and the reported energy too high. So the calculation then returns to its beginning, seeking a wavefunction and energy depicting the desired state obtained using "LDIAG = TRUE". The procedure is then repeated, performing new geometry optimizations, until this energy converges.

Normal completion of the procedure ensures that an optimized geometry and valid energy is obtained pertaining to the initially specified excited state. Most significantly, I find that, for all the test cases studied, the final results are independent of starting geometry and wavefunction. This provides a significant and widely applicable advance to VASP methodology for investigating excited states.

6.2.2 Ab Initio and DFT calculations for the neutral V_NN_B model compound.

The relative energies to the ground state, obtained using 11 computational methods for 13 low energy excited states, of the model compound (Fig. 6.4a) are compared in Table 6.8 evaluated, at a test geometry. This test geometry was obtained by optimizing the structure of the $(1)^2B_1$ ground state of the V_NN_B defect embedded in a 2-D layer of h-BN, then cutting out the model compound (Fig. 6.4a), adding and optimizing terminating hydrogen atoms. In Table 6.6, the dominant orbital occupancies of all involved states are listed. The included states were chosen based on TDDFT and EOM-CCSD evaluations, selecting all low-energy states plus also a few other of particular relevance. Note that this systematic search procedure identified some low-energy states such as $(2)^2B_1$ and $(1)^2A_2$ that have not previously been considered [73].

Application of the CASPT2 and MRCI methods requires specification of active spaces. A range of active spaces are used, as listed in Table 6.11, where results for each are compared; only the most reliable results obtained are listed in Table 6.8. In principle, the smallest active space used, with 9 electrons distributed fully amongst 8 orbitals, is sufficient to embody all key features of interest. Expanded active spaces up to 13 electrons in 13 orbitals are used to include more effects and increase accuracy. However, as a guide to the convergence of the calculations with respect to active-space expansion, I calculate the standard deviations between the results listed in Table 6.11. For the entire data set, I obtain 0.13 eV for MRCI and 0.15 eV for CASPT2, using these as precision estimates for the methods. These values are small and indicate that electron correlation effects are less important for this defect than they are in V_NC_B (described earlier) [82], a system with an even number of electrons for which much larger variability was found.

The basic precision of the DFT methods is also considered in Table 6.11 where results obtained using very different implementations, Gaussian-09 applying the cc-PVTZ basis set, and VASP applying PAW pseudopotentials, is reflected by an average difference of 0.04 ± 0.01 eV in the state energies. This result is similar to that found for V_NC_B [82] and reflects the high quality of the different computational approaches.

Table 6.9 provides a comparison of average differences and standard-deviation in excited state energies obtained by comparing the various computational results presented in Table 6.8 to each other. First I consider comparisons between results obtained using the ab

initio MRCI, CASPT2, CCSD, EOM-CCSD and CCSD(T) methods. Each method has its own set of advantages and disadvantages in terms of feasibility and comprehensiveness. MRCI treats static electron correlation the best with CASPT2 providing a more computationally efficient approximation, CCSD(T) includes static electron correlation in an asymmetric fashion but contains the best description of dynamic electron correlation, while CCSD is a more computationally efficient alternative that in this application will be more approximate than MRCI. EOM-CCSD embodies any deficiency in the treatment of its reference state (here $(1)^2B_1$) and has a less accurate treatment of dynamic electron correlation, but it properly includes the static electron-correlation effects addressed empirically through Eqns. (6.2)-(6.7).

The results show excellent agreement between the best methods, MRCI and CCSD(T), predicting an average excited-state energy difference of 0.0±0.3 eV. The CCSD, and EOM-CCSD results differ from these by 0.3 eV, suggesting that the enhanced treatment of dynamic correlation present in CCSD(T) is able to include the enhanced treatments of static correlation present in MRCI, with other correlation effects not being important. That CASPT2 agree well with MRCI and CCSD(T) results supports this conclusion, suggesting that it provides an efficient and accurate ab initio approach for studying the spectroscopy of this defect. This situation is very different to that found for the V_NC_B [82]. Its singlet ground state leads to dramatic effects associated with static electron correlation, with reduced internal consistency between the different ab initio results. This result here suggests that, for V_NC_B, the MRCI results provide the most reliable description of the spectroscopy.

Next, I compare those ab initio results to analogous ones from DFT, with the second column of Table 6.9 providing correction energy shifts for each method in a crude summary. HSE06 preforms very well, with an average error of -0.3±0.2 eV compared to MRCI and -0.3±0.1 eV compared to CCSD(T) and hence has an accuracy similar to that of CCSD. PBE performs poorly in absolute terms, with related errors of 0.8±0.3 eV and 1.0±0.3 eV, respectively, but the standard deviations remain low and hence relative state orderings are maintained. CAM-B3LYP, which contains corrections affecting the charge-transfer contributions to the states, performs best with related errors of 0.0±0.3 eV and 0.1±0.2 eV, respectively. These DFT results parallel those for V_NC_B [82], except that the errors here are much reduced in magnitude: for V_NC_B, only CAM-B3LYP provided a realistic description, with large errors reported for HSE06 and PBE.

As CAM-B3LYP is not available for periodic solids, I focus on the HSE06 results. For V_NN_B, from Table 6.9 it would seem that a simple shift of all calculated HSE06 energies by 0.3 eV should lead to accurate predictions of excited-state energies. Note that this correction applies to both one-unpaired-electron in one-orbital traditional doublet states, states for which first-principles DFT calculations can be routinely applied, as well as for the three-unpaired-electrons in three-orbitals situations that I empirically approximate using Eqn. (6.6). Also, a general feature of relevance, for aromatic molecules with traditional closed-shell ground states, is that CAM-B3LYP typically uniformly overestimates excited-state energies [42,43,82].

Table 6.8 Energies (in eV) of various excited states of the V_NN_B model compound (Fig. 6.4a) with respect to $(1)^2B_1$, performed at a reference geometry determined for $(1)^2B_1$, depicting calculated vertical excitation energies.

State	MRCI	CASPT2	CCSD (T)	CCSD	EOM-CCSD	CAM-B3LYP TD	HSE06 TD	PBE TD	HSE06 G09	PBE VASP	HSE06 VASP
$(2)^2B_1$		3.35			3.99	3.69	3.04	2.23		2.46	3.38
$(1)^2A_1$	3.19	3.50	3.26	3.35	3.34	3.18	3.00	2.47	2.96	2.54	2.93
$(1)^2A_2$	3.61	3.15	3.15	3.43	3.57	3.48	3.10	2.38	3.06	2.55	3.00
$(2)^2A_2$	3.81	3.89	4.21	4.88	4.59	4.34	3.84	2.74	3.87	3.10	3.60
$(2)^2A_1$	4.37	4.10			4.48	4.16	4.82	3.99			
$(3)^2A_2$		4.31			4.98	4.78	4.46	4.19			
$(4)^2A_2$		4.58			5.21	5.05	4.61	3.84	4.42	3.74	4.39
$(1)^4A_1$	4.36	4.20	4.38	4.48		4.28	3.89	3.52	3.94	3.55	3.88
$(3)^2B_1$		5.03			5.57	5.31	4.76	3.87		4.17	
$(3)^2A_1$		4.95	5.25	5.54	5.43	5.12	5.32	4.18		4.48	5.17
$(5)^2A_2$		4.83			5.52	5.35	5.06	4.29			
$(4)^2A_1$		5.27			5.57	5.63	5.21	4.36			4.59
$(6)^2A_2$		4.52				6.25	5.31	5.53			

Table 6.9 Corrections to add to DFT calculated transition energies from $(1)^2B_1$ (second column, in eV), determined from averaged differences in transition energies predicted by the methods listed in the rows compared to those in the later columns, for the V_NN_B model compound (Fig. 6.4a), evaluated at a test geometry.[a]

method	Corr.	MRCIC (13,13)	CCSD(T)	CCSD	EOM-CCSD	CASPT2	CAM-B3LYP TD	HSE06	PBE TD
CCSD(T)		4 0.0±0.3							
CCSD		4 0.3±0.5	5 0.3±0.2						
EOM-CCSD		4 0.3±0.3	4 0.3±0.1	4 -0.0±0.2					
CASPT2		5 -0.1±0.3	5 -0.0±0.2	5 -0.3±0.4	11 -0.5±0.2				
CAM-B3LYP TD	0.0±0.3	5 0.0±0.3	5 0.1±0.2	5 -0.2±0.2	11 -0.2±0.1	13 0.4±0.4			
HSE06	-0.3±0.2	4 -0.3±0.2	4 -0.3±0.1	4 -0.6±0.3	3 -0.5±0.1	4 -0.2±0.2	4 -0.4±0.1		
HSE06 TD	-0.2±0.4	5 -0.1±0.4	5 -0.2±0.2	5 -0.5±0.3	11 -0.5±0.3	13 0.1±0.4	13 -0.3±0.4	4 0.0±0.0	
PBE TD	-0.9±0.3	5 -0.8±0.3	5 -1.0±0.3	5 -1.2±0.5	11 -1.2±0.4	13 - 0.6±0.6	13 -1.0±0.4	4 -0.7±0.3	13 -0.7±0.4

[a] calculations are performed at a geometry optimized for the $(1)^2B_1$ reference state, see text.

Table 6.10 Energies with respect to the $(1)^1B_1$ ground state of various excited states of the V_NN_B model compound and related periodic 2-D material (Fig. 6.4), evaluated at their adiabatic minimum-energy geometries, oscillator strengths in absorption calculated using TDDFT, and the absorption reorganization energies λ depicting the width of the bands.

State	Adiabatic excitation energy[a] / eV						Osc. Strength		reorganization energy[a] λ / eV					
	model				2D material		model		model				2D material	
	PBE	HSE06 G09	HSE06 VASP	CAM TD	PBE	HSE06	HSE06	CAM	PBE	HSE06 G09	HSE06 VASP	CAM TD	PBE	HSE06
$(2)^2B_1$	2.14		2.86	2.37	2.04	2.39	0.0877	0.0985	0.31		0.52	0.54	0.49	0.73
$(1)^2A_1$	2.03	2.44	2.41	1.93	1.29	1.81	0.0001	0.0002	0.52	0.53	0.52	0.48	0.60	0.53
$(1)^2A_2$	2.17	2.50	2.51	2.23	2.80	3.36	0.0023	0.0019	0.38	0.56	0.51	0.47	0.32	0.45
$(2)^2A_2$	2.84	3.55	3.27	2.25	2.85	3.82	0.0003	0.0007	0.26	0.32	0.33	0.15	0.21	0.24
$(2)^2A_1$	3.53		4.60	3.63	2.70	3.48	0.0001	0.0002				0.25		
$(3)^2A_2$	4.03		4.68	4.12	3.98	4.76	0.0126	0.0066				0.12		
$(4)^2A_2$	3.43	4.06	4.00	3.70	3.02	4.14	0.0564	0.0639	0.31	0.36	0.39	0.57	0.39	0.62
$(1)^4A_1$	3.27	3.60	3.54		2.46	2.77	0	0	0.28	0.34	0.34		0.29	0.26
$(3)^2B_1$	3.80		4.47	4.40	2.99	3.95	0.0121	0.0388	0.37		0.19	0.13	0.36	0.16
$(3)^2A_1$	4.19		5.10	4.28	3.36	3.98	0.0066	0.0085				0.06		
$(5)^2A_2$	4.13		5.28	4.99	4.08	5.36	0.0460	0.0601				0.42		
$(4)^2A_1$	3.72		4.56		2.96	3.56	0.0006	0.0012			0.03			

a: Observed values in a V_NN_B defect[75] are transitions of A_1 and B_2 symmetry, often near = 2 eV but found over 1 range of 1 eV in energy, with the emission reorganization energy of 0.04 to 0.17 eV, see Fig. 1 and text; calculated reorganization energies are for absorption.

Table 6.11 Energies (in eV) of various states of neutral V_NN_B (both the 2D periodic structure and the model compound, see Fig. 6.4a) with respect to $(1)^2B_1$.

State	Dominant orbital occupancy[a]												CASPT2			MRCI			HSE06 G09[a]	HSE VASP[a]
	V_{2b1}	V_{1a1}	V_{2a2}	V_{1b1}	$2a_1$	V_{1a2}	$1b_1$	$2b_1$	C_{1a2}	C_{2a2}	C_{b1}	C_{a1}	(9,8)	(11,11)	(13,13)	(9,8)	(11,11)	(13,13)		
$(1)^2B_1$	2	2	2	2	2	2	1	0	0	0	0	0	[0]	[0]	[0]	[0]	[0]	[0]	[0]	[0]
$(2)^2B_1$	2	2	2	2	2	2	0	1	0	0	0	0	3.49		3.35					3.21
$(1)^2A_1$	2	2	2	2	1	2	2	0	0	0	0	0	3.39	3.09	3.50	3.07	3.22	3.19	2.96	2.93
$(1)^2A_2$	2	2	2	2	2	2	0	0	1	0	0	0	2.95	2.78	3.15	3.83	3.53	3.61	3.06	3.01
$(2)^2A_2$	2	2	2	2	2	1	2	0	0	0	0	0	4.14	3.72	3.89	3.96	3.57	3.81	3.87	3.84
$(2)^2A_1$	2	2	2	2	1	2	1	1	0	0	0	0	4.41	4.17	4.10	4.15	4.42	4.37		
$(3)^2A_2$	2	2	2	2	2	1	1	1	0	0	0	0		4.25	4.31					
$(4)^2A_2$	2	2	2	2	2	2	0	0	0	1	0	0		4.27	4.58					4.39
$(1)^4A_1$	2	2	2	2	1	2	1	1	0	0	0	0		4.50	4.20	4.45	4.54	4.36	3.94	3.88
$(3)^2B_1$	2	2	2	2	2	2	0	0	0	0	1	0	5.07		5.03					4.66
$(3)^2A_1$	2	2	2	2	1	2	1	1	0	0	0	0		5.14	4.95					
$(5)^2A_2$	2	2	2	2	2	1	1	1	0	0	0	0			4.83					
$(4)^2A_1$	2	2	2	2	2	2	0	0	0	0	0	1		5.14	5.27					4.59
$(6)^2A_2$	2	2	2	2	2	0	2	0	1	0	0	0		4.81	4.52					

[a] calculations are preformed from $(1)^2B_1$ reference state.

Table 6.10 lists the HSE06 adiabatic energies of 13 excited state of V_NN_B, along with the reorganization energies λ depicting the band spectroscopic width, for both the model compound and the 2D material. Some results are also presented using the PBE and CAM-B3LYP density functionals. Large differences are predicted between the excitation energies of the model compound and the 2D material of up to ± 1 eV. This occurs for both PBE and HSE06 calculations, though the magnitudes sometimes differ. Using HSE06, the low-lying excited states $(1)^2A_1$ and $(2)^2B_1$ relevant to the interpretation of h-BN spectra, are predicted to be stabilized by ca. 0.7 eV in the periodic solid, while for the other relevant low lying states $(1)^2A_2$ and $(2)^2A_2$, destabilizations by 0.6 eV are predicted. For V_NN_B, the used model compound is clearly too small to be realistic, and the errors associated with its use well exceed the errors associated with the use of DFT. I will discuss the key low-energy states of interest for V_NN_B in Chapter 7.

6.2.3 The +1 and -1 charged states of V_NN_B.

Consideration of charge states is important as they can become stable as the Fermi energy shifts due to doping (intentional or native) in the surrounding lattice. As the Fermi level

is raised, defect-induced states within the band gap become filled with electrons and vice versa. In order to check the stability of charge states of the V_NN_B defect, I have calculated the formation energies and charge transition levels (Chapters 4). I found that V_NN_B charged states become stable when the Fermi level moves closer to the valence or conduction band. Thus, the V_NN_B defect acts as a shallow charge donor or acceptor in h-BN. I found [189,190] that the oxidation potential needed to form $V_NN_B^{+1}$ is 1.8 eV (see Fig. 4.3 & Table 4.3), with the reduction potential needed to make $V_NN_B^{-1}$ being 3.23 eV (see Table 4.3).

Table 6.12 shows properties of the $V_NN_B^{+1}$ and $V_NN_B^{-1}$ defect states, evaluated on the model compound using HSE06 and CAM-B3LYP, as well as on the 2D material using HSE06 ΔSCF calculations. Both ions are predicted to have $(1)^1A_1$ ground states in both the model compound and the 2D material, arising from closed-shell electronic configurations. A $(1)^1A_1$ ground state was also previously predicted for V_NC_B, a system isoelectronic to $V_NN_B^{+1}$ that also has C_{2v} symmetry [201]. These closed-shell ground states depict covalent bonds forming between defect atoms, but the associated bond lengths far exceed those typical of covalent bonding (see Fig. 6.4). As a result, the ground state has in reality large open-shell character, meaning that single-reference computational approaches such as those applied in Table 6.12 can introduce large errors.

For V_NC_B (earlier discussion in this chapter), I found that CAM-B3LYP calculations appeared to give the most reliable results, but computational methods are presently not available to allow this to be applied to 2D materials [201]. For HSE06, I found that the corrections of 0.7 eV are needed for triplet states compared to closed-shell singlet states and 1.0 eV for open-shell singlet states. For the isoelectronic species $V_NN_B^{+1}$, applying these corrections bring the HSE06 and CAM-B3LYP results in Table 6.12 into line, whereas they already agree well for $V_NN_B^{-1}$ without correction. These corrections therefore do not appear universal but rather depend on the nature of the frontier orbitals. The tentative level structure of $V_NN_B^{+1}$ and $V_NN_B^{-1}$ calculated at HSE06 level is presented in the next chapter.

Table 6.12 Energies of various excited states of the $V_NN_B^{+1}$ and $V_NN_B^{-1}$ model compound and related periodic 2-D material (Fig. 6.4a), with respect to their $(1)^1A_1$ ground states, evaluated at their adiabatic minimum-energy geometries, oscillator strengths in absorption, and the reorganization energies λ depicting the width of the bands.

Defect	State	Adiabatic excitation energy / eV			Osc. Strength		reorganization energy[a] λ / eV		
		model		2D material	model TD		model		2D material
		HSE06 TD	CAM TD	HSE06	CAM	HSE06	HSE06 TD	CAM TD	HSE06
$V_NN_B^{+1}$	$(1)^1B_2$	0.72	1.84	2.32	0.0014	0.0006	0.81	0.83	0.48
	$(1)^1B_1$	1.9	3.27	0.86	0	0	0.82	0.53	1.82
	$(2)^1A_1$	2.68	3.35	2.44	0.0886	0.0552	0.60	0.68	0.25
	$(2)^1B_1$	3.33	3.6	3.70	0.0046	0.0029	0.21	0.26	0.32
	$(2)^1B_2$	3.11	3.88	2.75	0.0454	0.0116	0.36	0.35	0.45
	$(3)^1B_1$	4	4.42	4.27	0.0057	0	0.19	0.20	0.24
	$(1)^3B_1$	1.55	2.13	0.60	-	-	-	0.31	-
	$(1)^3B_2$	1.09	1.96	2.20	0	0	0.66	0.77	0.54
	$(1)^3A_1$	2.24	2.99	2.33	0.0000	0.0000	0.75	0.93	1.31
	$(2)^3B_2$	2.71	3.48	2.76	0.0000	0.0000	0.29	0.28	1.36
	$(2)^3B_1$	2.770	32.17	3.78	0.1038	0.0760	0.54	0.75	0.51
	$(2)^3A_1$	2.93	3.96	2.78	0.0001	0.0001	0.45	0.55	1.24
$V_NN_B^{-1}$	$(1)^1B_2$	1.27	1.53	1.66	0.0001	0.0014	0.74	0.73	0.79
	$(2)^1A_1$	2.13	2.24	1.66	0.2766	0.2689	0.27	0.31	0.11
	$(1)^1B_1$	2.73	2.76	1.10	0.0011	0.0008	0.21	0.22	0.27
	$(1)^1A_2$	2.8	3.23	1.71	0	0	0.42	0.48	0.26
	$(2)^1B_1$	2.93	3.44	1.52	0.0006	0.0001	0.37	0.39	0.29
	$(2)^1B_2$	3.29	3.39	collapsed	0.2237	0.2070	0.32	0.35	
	$(1)^3A_1$	1.67	1.11	0.76	-	-	-	-	-
	$(1)^3B_2$	1.48	1.06	1.89	0.0095	0.0018	0.33	0.69	0.67
	$(1)^3B_1$		-0.13	1.10	0	0.0001		0.85	0.39
	$(2)^3B_2$	3.08	2.66	1.98	0.0347	0.0364	0.21	0.15	0.47
	$(2)^3A_1$	3.59	3.08	1.50	0.1306	0.1515	0.15	0.17	0.39
	$(1)^3A_2$	3.46	2.99	1.71	0	0	0.22	0.21	0.34

a: for relaxation from the $(1)^1A_1$ ground state for all singlet states and for the lowest triplet state, $(1)^3B_1$ for $V_NN_B^{+1}$ and $(1)^3A_1$ for $V_NN_B^{-1}$, else for excited triplet states for relaxation from the lowest triplet state, as is appropriate for triplet to triplet spectroscopy.

A brief discussion on the limitation of the model compound approach is in order, the benchmarking approach adopted in this chapter is carried on a small model compound of h-BN flake and the errors in the static correlation by DFT functional are tested. The small model compounds might not completely embed the point defect. Indeed the TDDFT calculations performed on larger model compounds (Appendix Table 0.3) clearly reflect this. One problem of using small model compound is that dynamic correlation effects of the periodic systems might not be fully in cooperated. Another problem with this treatment is that the electrons of larger h-BN flakes would interact with these localized electrons via exchange and correlation effects that can effectively screen the static correlation interaction. Therefore, the error estimate might not be that accurate. It is very difficult to estimate the strength of this screening effect. This issue can be sorted by applying larger and larger models, however,

this can be computationally prohibitive (and therefore beyond the scope of this thesis, but is a subject of future studies).

Chapter 7 Level Structure of V_NC_B, V_BC_N and V_NN_B

In h-BN, a narrow emission band has been observed with a ZPL transition at 1.95 eV [11,24,192] but the origin of this emission is unclear. In the previous chapters based on a broad examination of possible defect sites in h-BN using DFT with the PBE functional, I have reasoned that V_NC_B, V_BC_N and V_NN_B form likely candidates as the origin of this emission and benchmarked the HSE06 calculations against exact quantum chemistry approaches. In this chapter, I present my calculations for the detailed level structures of V_NC_B, V_BC_N and V_NN_B. I use group theoretical analysis to predict the optical cycles of these defects. The calculated PL line shape (best matched with experimental PL spectra) of dipole allowed transition $(2)^3B_1 \rightarrow (1)^3B_1$ for the defect V_NC_B is presented and a comparison with available experimental literature is made.

7.1 Level structure of V_NC_B and V_BC_N

In this section, I discuss the detailed level structure of two related defects i.e. V_NC_B and V_BC_N. The electronic structure of V_NC_B has been discussed in detail elsewhere [124], with the effects seen being generically characteristic of most h-BN defects. Basically, at the defect site one σ and one π orbital on the two defect boron atoms and the carbon atom are left with dangling bonds. For the case of V_NC_B, four electrons need be distributed in these orbitals. The three σ atomic defect orbitals combine to make the molecular orbitals depicted in Fig. 7.1(a), one of an apparently "bonding" nature (named $1a_1$), one of a "non-bonding" nature (named $2a_1$), and one of an "antibonding" nature (named b_2). Similarly, the three π orbitals combine to make analogous orbitals named $1b_1$, $2b_1$, and a_2, respectively. The "bonding" orbitals have the shape of bonding orbitals found in say 3-centre 2-electron bonds but the interatomic distances are so large that in reality no bond exists, and it is this feature that DFT methods find difficult to accurately model [38]. It is seen here that $1a_1$ lies below the VB and so is always doubly occupied, $2a_1$, $1b_1$ and then $2b_1$ fall in the VB-CB gap of h-BN, while a_2 and b_2 fall inside the CB. Transitions amongst these 6 orbitals dominate the spectroscopy of the defect, with transitions involving orbitals localized within the h-BN valence-conduction band gap being the most likely to produce sharp absorption and emission spectra. Visualizations of wave functions

corresponding to key molecular orbitals (MOs) are shown in Fig. 7.1(a) (mid band-gap orbitals for the 2-D layer).

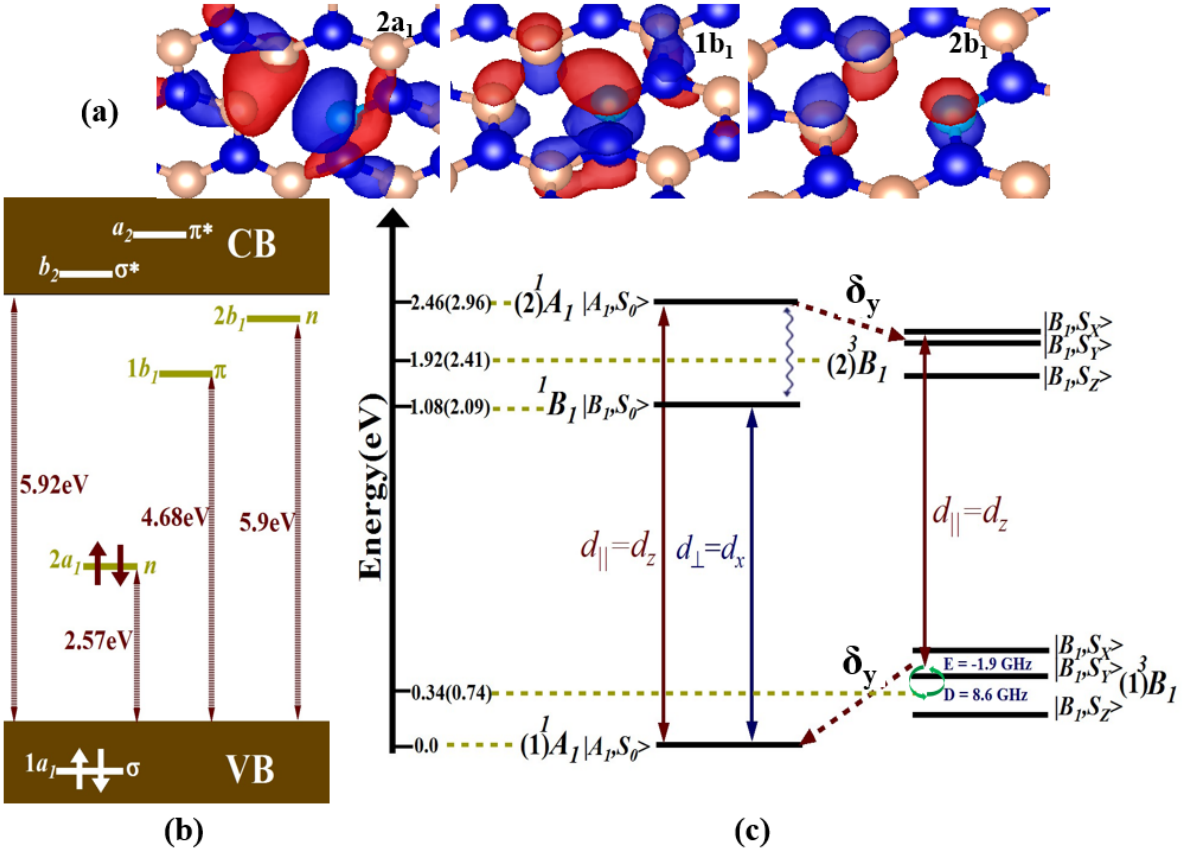

Figure 7.1 (a) Orbitals localized within the h-BN valence-conduction band gap from the periodic V_NC_B. (b) Key DFT orbitals from the $(1)^1A_1$ closed-shell ground-state electronic structure of V_NC_B. The states are labelled according to the symmetry of Irreducible representation as per C_{2v} point group. x(y,z)-axis are perpendicular(in the) to the plane of defect. (b) HSE06 adiabatic energies of low lying states of V_NC_B as calculated by DFT, with, in (), these energies corrected according to ab initio CCSD(T), EOM-CCSD, and CASPT2 calculations for a model compound [82]. Allowed transition polarizations d, spin-orbit couplings λ driving non-radiative transitions and zero-field splittings are also indicated.

In the light of the ab initio calculations (presented in the Chapter 6) using the CCSD(T) [127,128], EOM-CCSD [129,130], and CASPT2 [155] and MRCI [156] methods to calibrate the calculated HSE06 energies for the states of V_NC_B [82], I discuss its level structure here and make realistic predictions of photoluminescence energies.

A search of 18 excited states of V_NC_B [82] identified the only ones likely to contribute to the observed 1.95 eV photoluminescence to be $(1)^1B_1$ and $(2)^1A_1$ if the luminescence occurs within the singlet manifold, and $(1)^3B_1$ and $(2)^3B_1$ if intersystem crossing leads to population

of the triplet-state manifold. These states and their properties are sketched in Fig. 7.1 (b) and are interpreted in terms of the orbital energies for the $(1)^1A_1$ ground state shown in Fig. 7.1 (a). The energies shown in this figure include those calculated using DFT, as well as those corrected using ab initio calculated corrections [82]. The lowest-energy adiabatic transition within the singlet manifold is predicted to be $(1)^1B_1 \rightarrow (1)^1A_1$ at 2.08 eV, close to the observed value, while the lowest-energy transition within the triplet manifold is predicted to be about the same, $(2)^3B_1 \rightarrow (1)^3B_1$ at 1.58 eV. The singlet-manifold transition is very weakly allowed with an oscillator strength calculated by TDDFT for a model compound to be 0.0002 [82]. By symmetry, this transition will have its dipole-oriented perpendicular to the plane of the h-BN layer and emission would therefore be in the plane. There is also a singlet manifold transition with its dipole in the plane at 2.46 eV involving the doubly excited $(2)^1A_1$ state. While its dipole strength will be very small, emission with a reasonable lifetime could result following intersystem crossing to $(1)^3B_1$ state. While the best estimate of the state energies after correction has this process endothermic by 0.16 eV, it is feasible that the reaction is exothermic instead, making it also feasible that this transition produces the observed photoemission.

As the observed single photon emission from h-BN defects [75] is thought to be in the plane of h-BN sheet. Therefore, I have calculated the photoluminescence line shape of $(1)^3B_1 \rightarrow (2)^3B_1$, as it is the only electric-dipole allowed in-plane transition with an energy lying within experimental window as shown in Fig 7.1. I have used normal modes produced by VASP and used the methodology implemented in Dushin [184] code to calculate the line shape. A general feature is that no negative frequencies are found for ground and excited state triplets, hence the structure remains planar and C_{2V} symmetry is preserved. The calculated reorganization energy is 0.17 eV, which matches well the experimental reorganization energy of 0.14 eV. The calculated spectrum does not follow the fine details of the experimental spectrum, however high energy feature around peaks A, B and C in Fig 7.2 are somewhat reproduced. Thus, V_NC_B can be a possible emitter in h-BN.

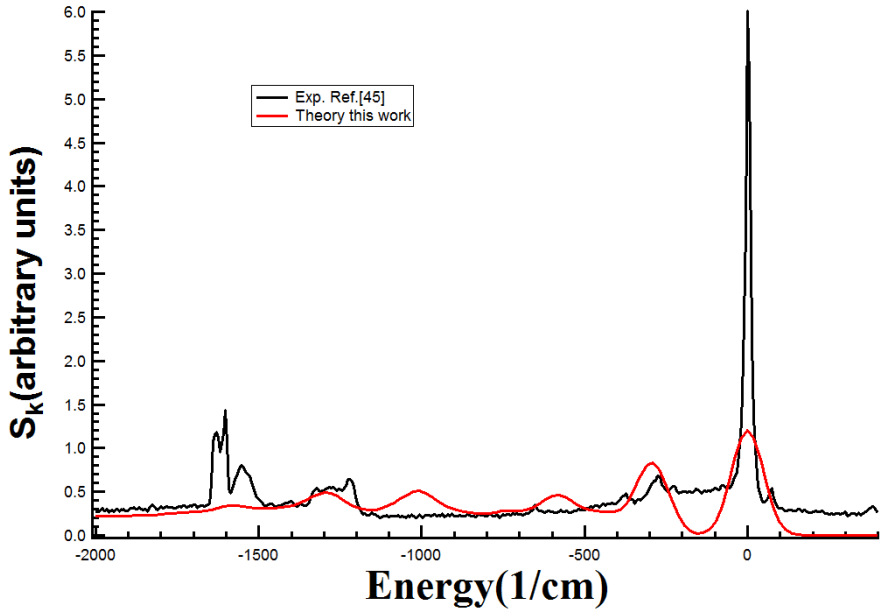

Figure 7.2 The calculated line shape for $(1)^3B_1 \rightarrow (2)^3B_1$ transition for V_NC_B superimposed on exp. Line shape for ref. [44].

Now I present the results for V_BC_N, which is the only defect predicted to have a triplet ground state, making it feasible for use in quantum spin devices. The electronic orbitals energies of this defect are shown in Fig. 7.3 and are analogous to those shown in Fig. 7.1 for V_NC_B, except that the involved σ orbitals are now ordered $1a_1 < b_2 < 2a_1$, while the π orbitals are ordered $1b_1 < a_2 < 2b_1$. Its ground state is $^3B_2$ with the lowest-energy singlet state calculated to be $^1A_1$ at an adiabatic transition energy of 1.23 eV as calculated by DFT, changing to 0.53 eV applying likely corrections based on the ab initio calculations for V_NC_B. This energy difference is sufficiently high such that the prediction of a triplet ground state is likely to be robust. For V_BC_N, three defect orbitals (Fig 7.3(b)) fall within the VB of h-BN, making them doubly occupied, while the remaining three orbitals fall in the band gap between VB and CB and are occupied by two electrons.

Although there is not a very good resemblance between the experimental and theoretical line shapes, and non-reproduced features may imply that, this defect might not have any relationship with emitting sources of h-BN. The non-reproduced features may be due to substrate effects or coupling of the vibrational modes with impurities or other defects centres etc which have not been considered in the calculations. Nevertheless, out of all the defect studied in this work only the PL line shape of V_NC_B for the $(1)^3B_1 \rightarrow (2)^3B_1$ transition have

some resemblance with experimental PL line shape. Therefore, this result is not ideal but still is quite a significant achievement.

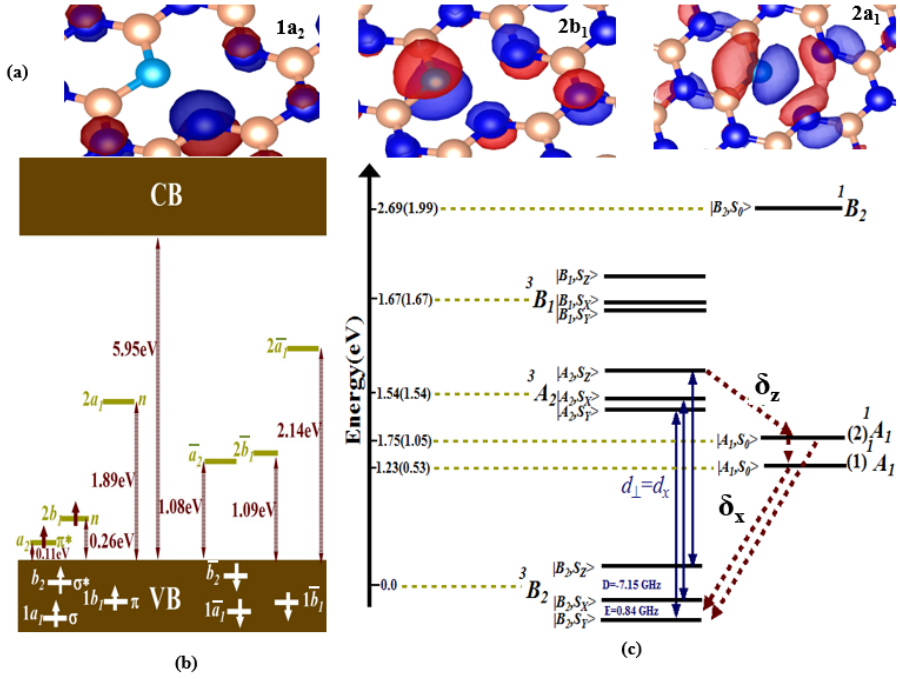

Figure 7.3 (a) Orbitals localized within the h-BN valence-conduction band gap from the periodic V_NC_B. (b) Key DFT orbitals from the $(1)^3B_2$ ground-state electronic structure of V_BC_N (the axis conventions are same as for V_NC_B). (c) HSE06 adiabatic energies of low lying states of V_BC_N as calculated by DFT, with, in (), these energies corrected according to ab initio CCSD(T), EOM-CCSD, and CASPT2 calculations for a model compound of V_NC_B. Allowed transition polarizations d, spin-orbit couplings λ driving non-radiative transitions, and zero-field splittings are also indicated.

Now I discuss in detail the nature of the spin-orbit interactions [220], zero-field splitting, and allowed intersystem crossing and optical transitions for defect V_NC_B and V_BC_N. A summary of the results is presented in Fig.7.1 & Fig. 7.3, highlighting the allowed in-plane and out of plane transitions, corresponding HSE06 adiabatic energies of these transitions and the possible paths of relaxation to the ground state. The key conclusion reached is that through appropriate optical pumping and relaxation cycles, ground-triplet-state spin polarization can be achieved for the V_BC_N defect in h-BN, making it of possible use in quantum information devices [221,222]. Thus, I discuss below how long-lived quantum memory in h-BN can be achieved for V_NC_B owing to the lifetime differences of the first and second order transitions from different triplet sub-states to the singlet ground state. The result for V_BC_N is most significant as for this defect the triplet state is predicted to be the ground-state of the system.

Thus in subsequent optical cycles ground state spin-polarization can be achieved for the V_BC_N as inter-system crossing results in preferential filling of $m_s = \pm 1$ spin sub-levels of triplet ground state.

Finally, a word on the possible electron-phonon coupling which can cause inter-system crossing is in order. The electron-phonon coupling is a very important aspect of studying the optical cycle of defects. However, because of lack of clear experimental evidence about inter-system crossing and the corresponding rates, only qualitative analysis of defect's optical cycles is made.

7.1.1 The spin-orbit Hamiltonian

The spin-orbit interaction is expressed in terms of the Hamiltonian [220]

$$H_{so} = \sum_k {}^1\!/_2 \frac{\hbar}{c^2 {m_e}^2} (\nabla_k V \times P_K).\left(\frac{S_K}{\hbar}\right) \qquad (7.1)$$

where, $V = e\phi$ is the nuclear potential, m_e the mass of electron and $P_K(S_K)$ is the momentum (spin) of the electron. Since the potential transforms as the totally symmetric representation (a_1 in C_{2v} symmetry), $\nabla_k V \times P_K$ transforms as a vector $V(V_x, V_y, V_z)$. Since P_K also transforms as a vector, it is possible to find the irreducible representation to which orbital operator $\vec{O} = \nabla_k V \times P_K$ belong and, using group theory, predict the non-vanishing elements of spin-orbit Hamiltonian. The only non-vanishing element of $\vec{O}$ is that for which $\langle \varphi_f | \vec{O} | \varphi_i \rangle \supset A_1$. For the ground and excited states of V_NC_B, the spatial part of the wave function transform like either B_1 or A_1. Similarly, for V_BC_N, the spin-orbit interaction occurs between the ground state triplet and the first higher energy singlet with spatial symmetries of B_2 and A_1, respectively. The non-vanishing elements of $\vec{O}$ can therefore, be determined and are summarized in Table 7.1 for both V_NC_B and V_BC_N.

Table 7.1 The Non-vanishing components of spin-orbit interaction for V_NC_B and V_BC_N. The quantities in rows and columns represent the symmetry of the spatial part of wave function for ground and first excited states of V_NC_B and V_BC_N.

V_NC_B	$\vec{O}^{A_1}$	A_1	B_1	$\vec{O}^{A_2}$	A_1	B_1	$\vec{O}^{B_1}$	A_1	B_1	$\vec{O}^{B_2}$	A_1	B_1
	A_1	×	0	A_1	0	0	A_1	0	×	A_1	0	0
	B_1	0	×	B_1	0	0	B_1	×	0	B_1	0	0
V_BC_N	$\vec{O}^{A_1}$	A_1	B_2	$\vec{O}^{A_2}$	A_1	B_2	$\vec{O}^{B_1}$	A_1	B_2	$\vec{O}^{B_2}$	A_1	B_2
	A_1	×	0	A_1	0	0	A_1	0	0	A_1	0	×
	B_2	0	×	B_2	0	0	B_2	0	0	B_2	×	0

Since angular momentum transforms like an axial vector and has no A_1 component, one can conclude from the above table that the only non-vanishing component of $\vec{O}$ for ground and first excited state of V_NC_B (V_BC_N) is the *y(x)*-component. Therefore the simplified form of the spin-orbit Hamiltonian can be written like

$$H_{so(V_NC_B)} = \sum_k \delta_y S_K^y l_K^y$$

$$H_{so(V_BC_N)} = \sum_k \delta_x S_K^x l_K^x$$

Where $\delta_y(\delta_x)$ is the strength of interaction. By the same argument as stated above spin mixing of the triplet and singlet $(2)\ ^3B_1 \Leftrightarrow (2)\ ^1A_1$($^3A_2 \Leftrightarrow (1)\ ^1A_1$) for V_NC_B (V_BC_N) is caused by $\delta_y(\delta_z)$ component of spin-orbit interactions as shown in Fig.7.1(c) (Fig.7.3(c)).

7.1.2 Spin-Spin interactions

In general, a $S = 1$ electron spin system is described by a spin Hamiltonian of the following form: $H = g_e\beta \boldsymbol{B}\hat{S} + \hat{S}D\hat{S}$. Here g_e is the electronic g-factor ($g_e = 2.0028 \pm 0.0003$); $\boldsymbol{B}$ is the external magnetic field and D is the zero field splitting tensor. This tensor comprises the anisotropic dipolar interaction of the two electron spins forming the triplet state averaged over their wave function. This tensor is traceless and thus characterized by two parameters, D and E, i.e. the axial and rhombic zero-field splitting parameters, respectively. This spin-spin interaction arising owing to the non-spherical shape of molecular orbitals lifts the degeneracy of multiplets. Therefore, I have calculated the spin-spin contribution towards zero field splitting parameters (D *and* E) for high spin ground states of V_NC_B (V_BC_N) as shown in Fig.7.1(c) and Fig.7.3(c). As spin-orbit coupling links these singlets and triplets states, which possess same total wave function symmetry. Therefore, a large value of D for V_NC_B (V_BC_N) means that spin selective intersystem crossing $(1)\ ^3B_1 \Leftrightarrow (1)\ ^1A_1$($^3B_2 \Leftrightarrow (1)\ ^1A_1$) can preferentially fill state of $m_s = 0$ ($m_s = \pm 1$) spin projection. In addition, the first order spin-orbit interaction would link states of $m_s = \pm 1$ ($m_s = 0$) spin projection of $(2)\ ^3B_1$($^3A_2$) with singlets $(2)\ ^1A_1$(($1)\ ^1A_1$) for V_NC_B (V_BC_N) as shown in Fig.7.1(c) (Fig.7.3 (c)). Based on these arguments I discuss the possibility of achieving spin dependent photo luminescence and ground state spin-polarization for V_NC_B (V_BC_N).

7.1.3 Dipole allowed transitions and ground Triplet-State spin Polarization

In this section, I first study the effect of dipole allowed spin-preserved transitions. Such transitions may happen via dipole interaction. $H_{di} = \sum_j \sum_\alpha d_j^\alpha E_j^\alpha$, where $d = e(x,y,z)$ is the dipole moment of the electron and $\vec{E}$ is the electric field vector. These allowed transitions are induced either by the axial component of the dipole moment $d_\parallel = d_z, d_y$ or it's out of plane component, i.e. $d_\perp = d_x$. For the V_NC_B ground (excited) state triplet $(1)\ ^3B_1((2)\ ^3B_1)$ is split by virtue of spin-spin zero field splitting and transformed into sub-states $|B_1, S_Z\rangle$ with symmetry B_2 and $|B_1, S_Y\rangle$, $|B_1, S_X\rangle$ with symmetries $A_1$and A_2 respectively. For V_BC_N, the ground (excited) state triplet $^3B_2(\ ^3A_2)$ is transformed into sub-states $|B_2, S_Z\rangle(|A_2, S_Z\rangle)$ with symmetry $B_1(A_1)$ and sub-states $|B_2, S_Y\rangle(|A_2, S_Y\rangle)$, $|B_2, S_X\rangle(|A_2, S_Y\rangle)$ with symmetries $A_2(B_2)$ and $A_1(B_1)$, respectively. For V_NC_B (V_BC_N), the spin preserved transition $(1)\ ^3B_1 \Leftrightarrow (2)\ ^3B_1$ $(\ ^3B_2 \Leftrightarrow\ ^3A_2)$ between respective magnetic sublevels occurs for the in-plane, i.e. $d_\parallel = d_z$ (out of plane i.e. $d_\perp = d_x$) component of the dipole moment. For V_NC_B after excitation from singlet ground state $((1)\ ^1A_1)$ to the phonon sideband of the optically allowed $(2)\ ^1A_1$ state, the system can relax directly to $(1)\ ^1A_1$ or vibronically to $^1B_1$ and then to $(1)\ ^1A_1$ with the emission of a photon. Alternatively, the inter-system crossing due to spin-orbit mixing (δ_y) as a first order endothermic process can take place resulting in relaxation of $(2)\ ^1A_1$ population to $(2)\ ^3B_1$. The transition to $m_s = \pm 1$ spin sub-states of $(2)\ ^3B_1$ is a spin selective process as only *y*-component of spin-orbit mixing can couple these states. One can note that the spin sublevels of the triplet split even at zero magnetic field that is caused by the electron spin - electron spin dipolar interaction (zero-field splitting) because of the low-symmetry crystal field. The population of $(2)\ ^3B_1$ can decay to $(1)\ ^3B_1$ and then inter-system crossing can result in preferential emptying of $m_s = \pm 1$ sub-states of $(1)\ ^3B_1$ to singlet ground state. On the other hand decay of the $m_s = 0$ spin sublevel of $(1)\ ^3B_1$ to the singlet ground state is a second-order process. Therefore, in subsequent optical cycles, ODMR contrast can be achieved by microwave excitation (green arrows), owing to the lifetime differences of first and second order transitions from the different triplet sub-states to the singlet ground state. This behaviour is similar to N_2V defect in diamond [223]. Thus V_NC_B, can be exploited to realize a long-lived quantum memory in h-BN, as has also been proposed for the N_2V defect in diamond. This is

an exciting result, as in our recent DFT computational work, several potential single photons emitting defects in h-BN are studied and, amongst them, the V_NC_B defect is shown to best fit the experimental photoluminescence (PL) line shape [200]. Also, as the energies of the two ZPL's for V_NC_B (i.e. (1) $^1A_1 \leftrightarrow$ (2) $^1A_1$ and (1) $^1A_1 \leftrightarrow$ $^1B_1$) are matched to the energies of the group-1 and group-2 emitters reported in recent experimental work [21]. Therefore, present results might trigger many future studies on V_NC_B in h-BN for exploring its spin-physics.

For V_BC_N the excitation from the ground state triplet $^3B_2$ to the 2nd excited state triplet $^3A_2$ is forbidden due to symmetry constraints. However, not only spin dependent photo-luminescence can be achieved for V_BC_N for excitation to $^3A_2$ excited state but also in addition ground state spin polarization can be realized as shown in Fig.7.3. As *z*-component of spin-orbit coupling would link states of $m_s = 0$ spin projection with singlet (1) $^1A_1$ and then relaxation takes place to (2) $^1A_1$, followed by relaxation allowed by inter-system crossing (ISC) to the ($m_s = \pm 1$) sub-state of $^3B_2$. Thus one can have preferential filling of ($m_s = \pm 1$) sub-state of $^3B_2$ for excitation from $m_s = 0$ of the same in subsequent optical cycles. Therefore, ground state spin polarization can be achieved for V_BC_N. Thus, one can conclude that both V_NC_B and V_BC_N can potentially be exploited for spin qubit operation [221,222].

7.2 The level structure of V_NN_B defect (neutral, +1 and -1 charge state)

In this section, I present the calculated level structure of V_NN_B in its neutral, +1 and -1 charge states and argue on the basis of experimental observations (e.g. ZPL energies, re-organization energy, paired in-plane emission with orthogonal dipole moments etc.) the possibility of single photon emission from this defect.

7.2.1 V_NN_B defect

In Fig. 7.4(c), I depict the key low-energy states of interest, showing their adiabatic transition energies as determined by HSE06 for the 2D model, and those adjusted by the appropriate correction identified above for the model compound. Relevant transition intensities predicted for the model compound are shown in Table 6.10 (previous chapter). Independent of the application of these model-compound corrections, under experimental conditions, only the

$(1)^2A_1$ and $(2)^2B_1$ states appear relevant to the interpretation of observations. The predicted excited state energies and intensities are inconsistent with the observation of two close-lying intense absorptions of, by necessity, A_1 and B_2 symmetry [21,22,75].

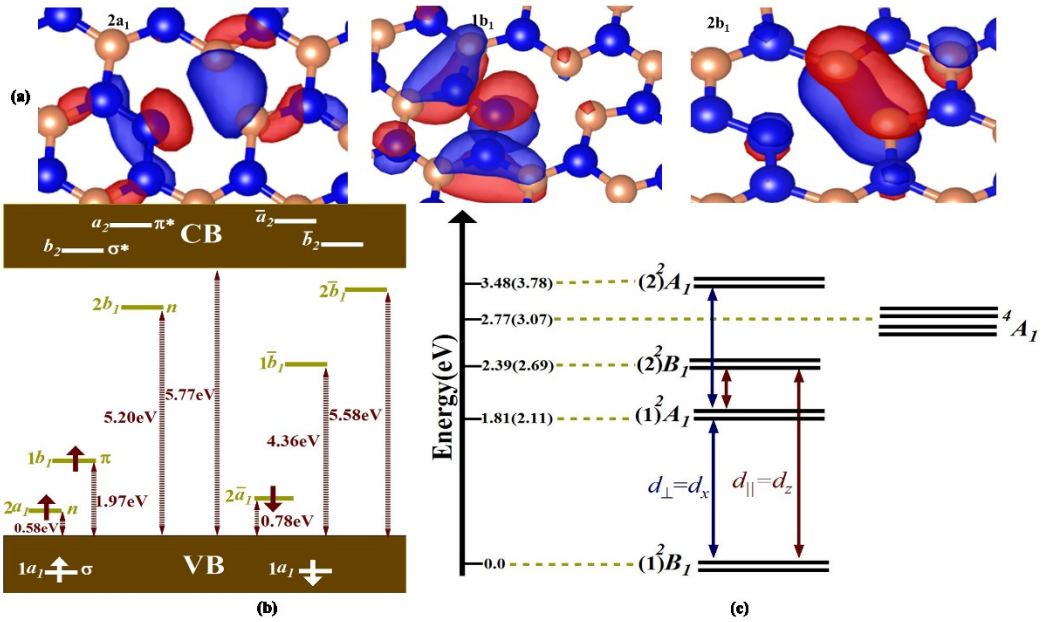

Figure 7.4 (a) Orbitals localized within the h-BN valence-conduction band gap from the periodic (b) Key DFT orbitals from the $(1)^2B_1$ ground-state electronic structure of V_NN_B. The states are labelled according to the symmetry of Irreducible representation as per C_{2v} point group. x(y,z)-axis are perpendicular to (in the) plane of defect. (c) HSE06 adiabatic energies of low lying states of V_NN_B as calculated by DFT, with, in (), these energies corrected according to ab initio CCSD(T), EOM-CCSD, and CASPT2 calculations for a model compound. Allowed transition polarizations d are also indicated.

In principle in-plane excitation can result in a PL peak at an energy of 2.69 eV, moreover UV excitation at energy of 3.78eV can populate 2^1A_1 state and then intersystem crossing can result in filling of the quartet 1^4A_1 state.

I hereby, consider the calculated reorganization energies listed in Table 6.9 for relaxation within C_{2v} symmetry to make comparison with experiment. The HSE06 values for the reorganization energies of $(1)^2A_1$ and $(1)^4A_1$ in the 2D material match well with previous calculations [73]. Values obtained for the model compound typically agree with those for the 2D material to within 0.2 eV, a much smaller difference than that found for V_NC_B; also the reorganization energies are at most 0.7 eV, smaller than the largest values found for V_NC_B. Comparing calculated results for the neutral V_NN_B defect in the 2D material to experimental observations for h-BN, I see that only the $(2)^2A_2 \rightarrow (2)^1A_1$ transition is likely to have a calculated

reorganization energy (0.21 eV) small enough to be feasible in describing the experimental data. However, this state is predicted to be far too high in energy, far too weak in intensity, and to incorrectly emit with out-of-plane polarization. Of the low-energy states of appropriate polarization and intensity, the $(2)^2B_1 \rightarrow (1)^1B_1$ transition has a very large reorganization energy (0.73 eV), as calculated by HSE06, even larger than that found here and previously [200] for PBE.

The reorganization energies listed in Table 6.9 include only the contributions from in-plane relaxation within C_{2v}, excluding any that may arise from in-plane or out-of-plane distortions. As is known [123], the $(1)^1B_1$ ground state is predicted by HSE06 to undergo a distortion in a b_1 mode, and I find that the same also applies to $(2)^1B_1$ by normal-mode analysis of its Hessian matrix at C_{2v} symmetry.

Earlier, concerns were raised as to whether the prediction of out-of-plane distortion to a well depth of just 0.05 eV is sufficiently robust to, in itself, eliminate neutral V_NN_B as a serious contender for explaining the observed h-BN emission. The prediction of a distortion of a B_1 state by a b_1 mode indicates strong vibronic coupling between the B_1 state and an A_1 state [93], presumably here the close-lying $(1)^2A_1$ state. Clearly, the presence of a double-well in a b_1 mode depends strongly on how a particular computational method perceives the conical intersection between the $(1)^2B_1$ and $(1)^2A_1$ states [213]. In this case, spectral predictions cannot be made with confidence using standard approaches, even those utilizing curvilinear coordinates [224], as the strong vibronic coupling will invalidate the Born-Oppenheimer approximation upon which these methods are based, demanding full quantum treatment of the coupled electron-vibration problem [213]. Tables 6.9 provide enough information to access how reliable HSE06 is expected to perceive the conical intersection seam. If it yields similar vertical and adiabatic excitation energies, and therefore reorganization energies, as does the reference methods used, then realistic predictions of the presence and depth of the double well may be expected. While Table 6.10 shows good agreement at relaxed geometries, Table 6.8 indicates large differences for vertical excitation, leading to large reorganization energy differences in Table 6.10. Hence, the prediction of a shallow double well by HSE06 may not to be robust to improvements in methodology.

However, through a consideration of a wide range of properties of the excited-state manifold of V_NN_B, it is clear that this defect cannot account for the observed emission. Nevertheless, the reliance of the prediction of an out-of-plane distortion may not, in itself, be sufficient to eliminate this and other possible defects.

7.2.2 The +1 and -1 charged states of V_NN_B.

For $V_NN_B^{+1}$, the calculations predict the lowest-energy singlet excited state to be $(1)^1B_1$. This state would have an out-of-plane transition with the ground state that is inconsistent with observed h-BN defect spectra. It is predicted to have a very large reorganization energy of λ = 1.82 eV in the 2D material, and hence an extremely broad spectrum, with very low calculated oscillator strength, additional features all inconsistent with experiment. Within the triplet manifold, the low energy transitions are predicted to be either forbidden or else very weak and out-of-plane polarized, again inconsistent with experiment.

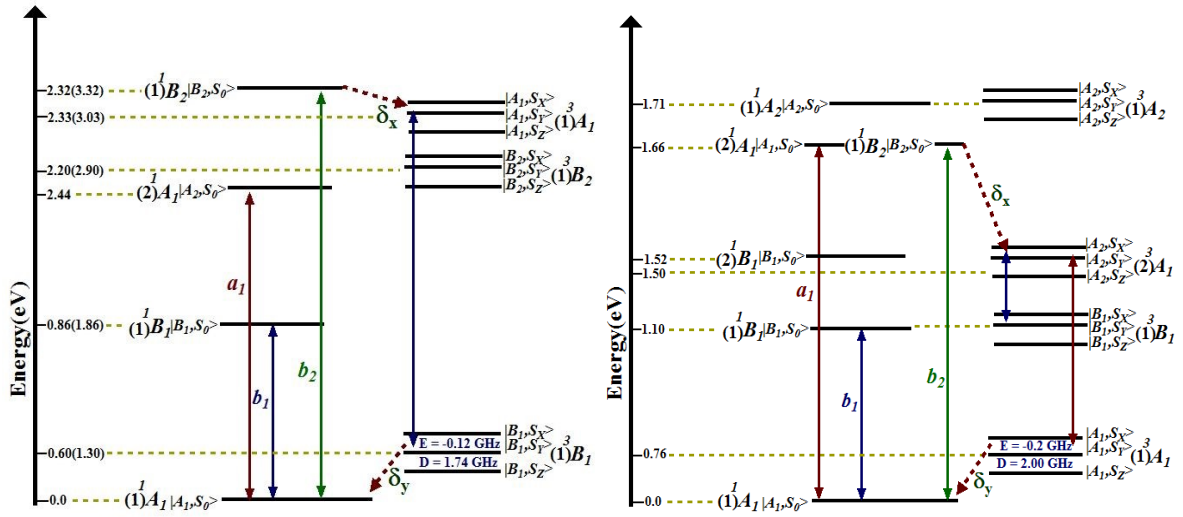

Figure 7.5 HSE06 adiabatic energies of low lying states of 2D $V_NN_B^{+1}$ (left) and $V_NN_B^{-1}$ (right), as calculated by DFT, with, in () for $V_NN_B^{+1}$, these energies corrected according to ab initio CCSD(T), EOM-CCSD, and CASPT2 calculations for the model compound. Allowed transition polarizations in the a_1, b_1, and b_2 directions (see Fig. 6.4) are also indicated.

For $V_NN_B^{-1}$, the calculations again predict the lowest-energy singlet excited state to be $(1)^1B_1$, having a weak and out-of-plane polarized transition to the ground state, but this time with only a small reorganization energy of 0.27 eV. However, above it by just 0.5 eV are predicted to be the $(1)^1B_2$ and $(2)^1A_1$ states, states with symmetries consistent with the observed

dual in-plane absorption polarizations [75]. It could be that the calculations have just misrepresented the energy of $(1)^1B_1$, and that in reality the other states are of lower energy. Indeed, the $(2)^1A_1$ state shows all the required properties: intense, with a very small reorganization energy of just 0.11 eV, but $(1)^1B_2$ appears insufficiently weak. Therefore, while some required features are present, overall it would seem unlikely that these states could explain the observed h-BN emission. The triplet manifold of $V_NN_B^{-1}$ is predicted to have many low energy transitions and is clearly inconsistent with the observed h-BN defect spectra.

7.2.2.1 Spin-spin interactions and possible applications to quantum information.

While none of the defects studied appear to closely relate to observed h-BN defects, it could be possible to engineer these defects deliberately. One of the driving forces for research into h-BN defects is the possibility that they may prove useful as qubits in quantum information processing systems. I proceed by examining how useful the calculated defects are likely to be in this regard.

Spin-orbit coupling can mix the triplet and singlet spin states, generating intersystem crossings, while spin-spin interaction lifts the degeneracy of spin-multiplets. In case if sophisticated experimental data is available for a particular defect species, the calculation of spin-orbit energy can provide useful information about a defect's optical cycle and it's potential usage as a qubit.[225] Clearly, so far such data is not available for h-BN defects, therefore quantitative analysis of spin-orbit coupling is beyond the scope of present work, however to predict the possibility of inter-system crossing we have performed a qualitative analysis. Specific patterns are required for defects to be useful as qubits. For neutral V_NN_B, the calculated splitting patterns are indicated in Fig. 7.4, whereas for charged defects they are shown in Fig. 7.5. Here I present a detailed discussion on the nature of the spin-orbit interactions [220], zero-field splitting, allowed intersystem crossing and optical transitions [220].

The key conclusion reached is that, in subsequent optical cycles, Optically Detected Magnetic Resonance (ODMR) contrast can be achieved by microwave excitation for $V_NN_B^{+1}$ and $V_NN_B^{-1}$, owing to the lifetime differences of the first and second order transitions from the different triplet sub-states to the singlet ground state. This behaviour is similar to N_2V defect

in diamond. Thus $V_NN_B^{+1}$ and $V_NN_B^{-1}$, should be exploitable to realize a long-living quantum memory in h-BN, as has also been proposed for the N_2V defect in diamond [223]. Because $V_NN_B^{+1}$ and $V_NN_B^{-1}$ have similar level structure to N_2V defect in diamond.

7.2.2.2 The spin-orbit Hamiltonian

For both ground and first excited states of interest for $V_NN_B^{-1}$ and $V_NN_B^{+1}$, the spatial part of the wave function transform like either A_1, B_1 or B_2. The non-vanishing elements of $\vec{O}$ can therefore be determined and are summarized in Table 7.2.

Table 7.2 The Non-vanishing components of spin-orbit interaction for $V_NN_B^{-1}$. The quantities in rows and columns represent the symmetry of the spatial part of wave function for ground and first excited states of $V_NN_B^{-1}$.

$\vec{O}^{A_1}$	A_1	B_1	B_2	$\vec{O}^{A_2}$	A_1	B_1	B_2	$\vec{O}^{B_1}$	A_1	B_1	B_2	$\vec{O}^{B_2}$	A_1	B_1	B_2
A_1	×	0	0	A_1	0	0	0	A_1	0	×	0	A_1	0	0	×
B_1	0	×	0	B_1	0	0	×	B_1	×	0	0	B_1	0	0	0
B_2	0	0	×	B_2	0	×	0	B_2	0	0	0	B_2	×	0	0

Since the angular momentum transforms like an axial vector and has no A_1 component, I can conclude from the above table that the only non-vanishing component of $\vec{O}$ for ground and first excited state of $V_NN_B^{+1}$ and $V_NN_B^{-1}$ is the *y&x*-component. Therefore, the simplified form of the spin-orbit Hamiltonian can be written like

$$H_{so(V_NN_B^{-1})} = \sum_k \delta_{y(x)} S_K^{y(x)} l_K^{y(x)} \qquad (7.2)$$

where $\delta_{y(x)}$ is the strength of the interaction.

7.2.2.3 Spin-spin interactions

The calculated spin-spin contribution towards zero field splitting parameters (D and E) for high spin ground states of $V_NN_B^{-1}$ and $V_NN_B^{+1}$ is shown in Fig. 6. The spin-orbit coupling links those singlets and triplets states which possess same total wave function symmetry, therefore a large value of D for $V_NN_B^{-1}$ and $V_NN_B^{+1}$ means that spin selective intersystem crossing $(1)\ ^3B_1 \Leftrightarrow (1)\ ^1A_1$ can preferentially fill state of $m_s = 0$ spin projection. In addition, the first order spin-orbit interaction would link states of $m_s = \pm 1$ spin projection of $^3B_1$ with singlets $^1A_1$ for $V_NN_B^{-1}$ and $V_NN_B^{+1}$ as shown in Fig. 7.5. Based on these arguments, we

discuss the possibility of achieving spin dependent photo luminescence and ground state spin-polarization for $V_NN_B^{-1}$ and $V_NN_B^{+1}$.

7.2.2.4 Dipole allowed transitions and possibility of achieving long lived quantum memory from $V_NN_B^{-1}$ and $V_NN_B^{+1}$

In this section, we first study the effect of dipole allowed spin-preserved transitions for $V_NN_B^{-1}$ and $V_NN_B^{+1}$. For the $V_NN_B^{+1}$ ($V_NN_B^{-1}$) ground (first excited) state triplet $(1)\ ^3B_1$ ($(1)\ ^3A_1$) is split by virtue of spin-spin zero field splitting and transformed into sub-states $|B_1\ , S_Z\rangle(|A_1\ , S_Z\rangle)$ with symmetry $B_2(A_2)$ and $|B_1\ , S_Y\rangle(|A_1\ , S_y\rangle)$, $|B_1\ , S_X\rangle(|A_1\ , S_X\rangle\ )$ with symmetries $A_1(B_1)$ and $A_2(B_2)$, respectively. The spin preserved transition $(1)\ ^3B_1 \Leftrightarrow (1)\ ^3A_1$ between respective magnetic sublevels occurs for the out of plane i.e. $d_{\|} = d_x$ component of the dipole moment. Thus, for the $V_NN_B^{+1}$, after excitation from singlet ground state ($(1)\ ^1A_1$) to the phonon sideband of the optically allowed $(1)\ ^1B_2$ state, system can relax directly to $(1)\ ^1A_1$ with the emission of a photon. Alternatively, the inter-system crossing due to the spin-orbit mixing (δ_x) as a first order process (exothermic) can take place resulting in shift of $(1)^1B_2$ population to $(1)\ ^3A_1$. The transition to $m_s = \pm 1$ spin sub-states of $(1)\ ^3A_1$ is a spin selective process as only *x*-component of spin-orbit mixing can couple these states. One can note that the spin sublevels of the triplet split even at zero magnetic field that is caused by the electron spin-electron spin dipolar interaction (zero-field splitting) because of the low-symmetry crystal field. The population of $(1)\ ^3A_1$ can decay to $(1)\ ^3B_1$ and then inter-system crossing can result in preferential emptying of $m_s = \pm 1$ sub-states of $(1)\ ^3B_1$ to the singlet ground state. On the other hand, decay of $m_s = 0$ spin sublevel of $(1)\ ^3B_1$ to the singlet ground state is a second order process. Therefore, in subsequent optical cycles, ODMR contrast can be achieved by microwave excitation, owing to the lifetime differences of first and second order transitions from the different triplet sub-states to the singlet ground state. This behaviour is similar to the N_2V defect in diamond.[223] A similar procedure resulted in the preferential emptying of $m_s = \pm 1$ sub-states of $(1)^3A_1$ to the singlet ground state for $V_NN_B^{-1}$. However, the possibility of spin polarization for $V_NN_B^{-1}$ is small (but not zero) compared to $V_NN_B^{+1}$. For $V_NN_B^{-1}$ spin-orbit mixing (δ_x) as a first order process (exothermic) can take place resulting in shift of the $(1)^1B_2$ population to $(1)^3A_1$. The population of $(2)^3A_1$ can radioactively decay to

$(2)^3A_1$. In principle, the spin-orbit interaction cannot connect the lowest energy triplet $(1)^3A_1$ and the singlet $(1)^1A_1$ ground state. However, participation of phonons allows this connection in the second order. This has been recently shown to be possible for N_v^{-1} where the spin-orbit interaction cannot couple the triplet $(1)^3A_2$ ground state and the lowest energy ^1E singlet state, but participation of phonons allows intersystem crossing in the second order.[226] Thus for $V_NN_B^{-1}$, phonons of b_1 symmetry can mix $(1)^3B_1$ into $(1)^3A_1$ that would result in shorter lifetime for the $|A_1, S_y\rangle$ state than for $|B_1, S_y\rangle$, where the latter can only decay to the ground state by a third-order process. Thus although the decay of $(1)^3A_1$ to $(1)^1A_1$ is not allowed in the first order, a second order process could lead to such a decay. Hence $V_NN_B^{-1}$ and $V_NN_B^{+1}$, can be exploited to realize a long-living quantum memory in h-BN as has been achieved for N_2V defect in diamond.

Chapter 8 Conclusion

There is currently great interest in the spectroscopy of point defects in 2-D and 3-D semi-conductors. The use of DFT computational schemes to examine the geometrical and spectroscopic properties of defect sites in materials is widespread, with many successes attained. However, here I conclude that a priori calculation of properties of defect states in 2D materials remains a daunting challenge. Primarily, this work is an attempt to identify the source of SPE in h-BN, however many key issues regarding the application of standard DFT computational approaches to defect sites are identified and possible solution is presented. In this thesis, I perform a detailed survey of likely defects e.g. potential defects responsible for single photon emission from h-BN. In particular, I focused on potential quantum emission candidate defects including intrinsic e.g. vacancies and anti-sites and extrinsic defects e.g. oxygen (O), hydrogen (H), carbon (C), silicon (Si), sulphur (S), fluorine (F) and phosphorus (P) defects. A few defects were shortlisted based on the energy level structure and then based on calculated HR factor I outlined three potential defects for observed single photon emission from h-BN, i.e. V_NC_B, V_BC_N and V_NN_B. I look at V_NC_B, V_BC_N and neutral and charged states of the V_NN_B defects in h-BN in detail. I calculate the formation energy and CTL's for these defect species. Since a standard method of defects identification is calculation of HF coupling constants and compare with experiment EPR values. Therefore, I calculated the hyperfine coupling parameters for many h-BN defects and was able to identify a few defect species based upon comparisons with available experimental data. Because of limited available experimental data, my HF coupling calculations for the other defects may serve as useful theoretical data that can be compared with possible future EPR experiments.

I calculate the level structure of my shortlisted defects i.e.V_NC_B, V_BC_N and V_NN_B. I benchmark the DFT calculations for the spectroscopy of these defects with ab-initio approaches on an equal model compound and some of the key conclusions of this benchmarking approach are as under. The defect V_NC_B and the charged states of V_NN_B have an even number of electrons and hence leading to singlet ground states, with $V_NN_B^{+1}$ being isoelectronic with V_NC_B [82]. Both of these defects result in very large errors when DFT methods are compared to ab initio ones for model compounds, the cause being the intrinsic open-shell nature of the ground state and other key defect states. Comparison of DFT-based results to accurate ab initio ones for a

model compound indicate that the PBE density functional is unsuitable, that for certain properties HSE06 predict very accurate answers but for others may involve large systematic errors of up to 1 eV in magnitude, and that results from CAM-B3LYP suffer less seemingly random anomalies and are generally much more reliable. While only methods containing correction for the asymptotic potential error should be applied to defect sites owing to their likelihood of involving charge-transfer spectroscopy, practical software limitations may limit current applications in periodic systems to uncorrected functionals like HSE06. The implementation of range-corrected hybrid functionals like CAM-B3LYP into solid-state DFT codes is a priority as defect-state spectroscopy is currently a very important research field.

Generally, when using DFT, serious problems occur when states involve significant multi-reference character, especially when comparing the energies of states, which differ markedly in this regard. Errors are most pronounced for closed-shell singlet states with "bonding"-type wavefunctions spanning broken bonds. If such a state is used to describe the excited states in a TDDFT calculation, then these errors in the ground state transfer to the excited states produced. I found that for V_NC_B at the test geometry, the HSE06 energies of triplet states are predicted to be too low by ca 0.7 eV compared to the energies of closed-shell states, while the energies of open-shell singlet states are underestimated by ca. 1 eV. For CAM-B3LYP, the errors are less, 0.3 eV for triplets and 0.5 eV for open-shell singlets, with an average error of 0.4 eV. The use of TDDFT to calculate triplet state energies based on a triplet-state reference function works well, but closed-shell singlet states with significant multi-reference character cannot be used reliably. Charge states of V_NN_B suffer similar issues, whenever open-shell character is involved, with different magnitudes of errors. The problems with the open-shell nature of key states is less for $V_NN_B^{-1}$ than it is for $V_NN_B^{+1}$, owing to the change in the nature of the key HOMO orbital.

For the neutral V_NN_B, a system with an odd number of electrons, I find here that the errors in DFT are much reduced, with state energies for model compounds being in error on average by 0.0 ± 0.3 eV for CAM-B3LYP, -0.3 ± 0.2 eV for HSE06, and, as expected, very poor for PBE at -0.9 ± 0.3 eV. Thus, I conclude that universal corrections for DFT calculations cannot be obtained: at least every isoelectronic system needs to be treated independently.

In general, the errors found appear to be minimal when the defect singlet states contain minimal covalent character. Geometrical relaxation tries to heal defects by forming covalent bonds, leading to possible significant enhancement of the error magnitudes described above, with calculated bandwidths for absorption and emission spectra being subject to the same effect. However, in 2-D and 3-D materials, strong restoring forces oppose these chemical forces, minimizing errors anticipated in DFT calculations towards the more basic results observed at the test geometry. Errors of order 0.3 eV in calculated state energies can be introduced through neglect of zero-point energy and entropy contributions at 298 K. While these are small compared to the other errors in DFT calculations considered, these effects will need to be included in accurate calculation.

At present, it would appear that the only commonly available reliable approaches for calculating defect states in 2-D and 3-D materials are ab initio methods such as CCSD(T), EOM-CCSD, CASPT2 and MRCI applied to model compounds chosen large enough so that they adequately represent the extended system in which the defect is found. The recent development [136-141] of efficiently scaling techniques of this type gives potential for expanded applications. However, these methods are still not as accurate as is desired, with variations of on average 0.3 eV being found between different approaches. Improved approaches treating well both multi-reference character and triples excitations are therefore required (and will be the subject of my future studies). On the other hand, the DFT functional found most reliable, CAM-B3LYP, is still not robust enough for general use. However, HSE06 calculations should be adequate for evaluating free-energy contributions and for optimizing geometries. If used without external calibration by ab initio methods, DFT results are expected to be very accurate when only triplet states of defects are involved, with the next best scenarios being when either only closed-shell singlet states or else only open-shell singlet states are involved.

A related issue for studies of model compounds or periodic 2-D samples is the need to use systems large enough to minimize errors. Based on the results and the identified strong competition between chemical and restorative forces in controlling defect structure, model compounds intended for accurate modelling should include one or more rings of atoms outside the ring that minimally describes the defect. Use of model compounds that are too small will

introduce artefacts owing to the propensity of defect sites to close on themselves to optimize covalent bonding. In addition, while typically transitions of interest are defect-localized, this may not always be the case and the appropriateness of cluster models to transitions involving conduction or valence band transitions will always be questionable. The small model compounds might not completely embed the point defect. One problem of using small model compound is that dynamic correlation effects of the periodic systems might not be fully in cooperated. Another problem with this treatment is that the electrons of larger h-BN flakes would interact with these localized electrons via exchange and correlation effects that can effectively screen the static correlation interaction. Therefore, the error estimate might not be that accurate. It is very difficult to estimate the strength of this screening effect. This issue can be sorted by applying larger and larger models, however, this can be computationally prohibitive (and therefore beyond the scope of this thesis, but is a subject of future studies).

Another significant issue concerning DFT calculations is the need, for computational purposes, to apply the ΔSCF procedure. This method often requires physical observables to be connected to calculated properties using an empirical ansatz. Improved future computational methods will, in the short term, bring significant advances to this situation. One advance will be the implementation of long-range corrected methods like CAM-B3LYP into periodic-image codes (future work). Such methods represent the entry level for DFT calculations on defect states as only they can correctly describe charge transfer, a critical aspect of defect spectroscopy. Both here, for V_NN_B, and V_NC_B [83], I find CAM-B3LYP delivering useful results in unusual chemical situations for which HSE06 fails significantly. A second forthcoming advance will be the widespread deployment of MC-DFT schemes [143,215]. Schemes that will in a systematic fashion handle the strong electron correlation aspects critical to defect spectroscopy.

Presented herein are also a range of computer programs that can interpret and control VASP calculations. These convert laborious human effort in searching for excited states into an automated procedure that mostly works, reducing human and computer time to only a few days to complete significant searches of excited-state manifolds. These methods are generally applicable to excited states far beyond the field of defect spectroscopy.

I also calculate the photo-luminescence line-shapes for some transitions within the manifolds of these defects and make comparison with experimental line shape. Concerning, the possibility that V_NN_B defects could contribute to the observed defect spectroscopy of h-BN, from the calculations performed it is clear that this is unlikely. Only one possible transition, the $(2)^1A_1 \rightarrow (1)^1A_1$ transition predicted in $V_NN_B^{-1}$, presents an intense, narrow-band of the correct polarization, in about the right region of the spectrum. While the predicted band is exceptionally narrow and consistent with observed bandwidths, the shape of its PSB is quite different to observed shapes. Further, a second required excited state of only slightly higher energy, of symmetry $(1)^1B_2$, with absorption intensity that is also intense, was not predicted, and further its $(1)^1B_1$ state, which cannot lie below the other states, was predicted to be 0.5 eV lower in energy. For V_NC_B the transition $(2)^3B_1 \rightarrow (1)^3B_1$ appears to be in the energy range of observed single photon emission and the calculated photo-luminescence line shape resembles with experimental line shape, making this defect a strong candidate of potential emitters.

Decisions as to the likelihood that a certain defect contributes to the observed h-BN spectroscopy should not be made solely on the grounds of calculated energies. As previously mentioned, energies are difficult to reliably predict. However, band-intensity and bandwidth information is more likely to be robust, and, given the certainty by which the experimental results depict polarization, intensity, and bandwidth, with in particular the observed bandwidth being extremely low (λ = 0.04 to 0.17 eV), this information becomes critical.

A critical feature of any prediction is as to whether or not any state is predicted to distort out of plane [123,143]. Such a distortion will add significantly to the reorganization energy provided that the well depth significantly exceeds the zero-point energy of the displacing mode. Such distortions may be difficult to predict reliably, however, as they flow from the nature of the conical intersection seam that links the state of interest to nearby states of the required symmetry. While DFT methods are likely to accurately reproduce the non-adiabatic vibronic coupling constant that determine the shape of the conical intersection seam, critical also is the accurate prediction of the energy gaps between excited states. This may not be done with sufficient accuracy, leading to improper predictions of symmetry breaking distortions. Only through careful examination of the excited-state manifold can estimates be made as to the

reliability of such predictions. Preliminary searches for defect states that could explain the observed h-BN emission are therefore best done ignoring this (eventually crucial) effect.

Finally, I note that out of all the defects examined; only V_BC_N was predicted to have a triplet ground state. I show that the available combination of excited-state energetics, spin-orbit coupling and zero-field splitting parameters leads to a scenario in which ground-state spin polarization and long-lived quantum memory in h-BN can be achieved for V_BC_N and V_NC_B respectively, by optical means, making these defects of interest for use in quantum computation. Also, the calculations predict that if by some means V_NN_B defects could be engineered into h-BN and charged states +1 and -1 can be realized, then these defects can be used for quantum computing applications by accessing different defect states e.g., $V_NN_B^{+1}$ and $V_NN_B^{-1}$, can be exploited to realize a long-living quantum memory in h-BN as has also been proposed for N_2V defect in diamond.

References

[1] T. D. Ladd, F. Jelezko, R. Laflamme, Y. Nakamura, C. Monroe, and J. L. O'Brien, Nature **464**, 45 (2010).
[2] D. D. Awschalom, L. C. Bassett, A. S. Dzurak, E. L. Hu, and J. R. Petta, Science **339**, 1174 (2013).
[3] L. Sangchul, Y. Jun-Seok, J. Yongsung, C. Chunhum, K. Dong-Yu, N. Seok-In, L. Byoung Hun, and L. Takhee, Nanotechnology **23**, 344013 (2012).
[4] A. Abderrahmane, P. J. Ko, T. V. Thu, S. Ishizawa, T. Takamura, and A. Sandhu, Nanotechnology **25**, 365202 (2014).
[5] L. Xuemei, Y. Jun, Z. Jianxin, and G. Wanlin, Nanotechnology **25**, 105701 (2014).
[6] M. Abdi, P. Degenfeld-Schonburg, M. Sameti, C. Navarrete-Benlloch, and M. J. Hartmann, Physical Review Letters **116**, 233604 (2016).
[7] F. Xia, H. Wang, D. Xiao, M. Dubey, and A. Ramasubramaniam, Nature Photonics **8**, 899 (2014).
[8] G. Clark, J. R. Schaibley, J. Ross, T. Taniguchi, K. Watanabe, J. R. Hendrickson, S. Mou, W. Yao, and X. Xu, Nano Letters **16**, 3944 (2016).
[9] R.-J. Shiue, D. K. Efetov, G. Grosso, C. Peng, K. C. Fong, and D. Englund, Nanophotonics (2017).
[10] J. Cai, A. Retzker, F. Jelezko, and M. B. Plenio, Nature Physics **9**, 168 (2013).
[11] T. T. Tran, K. Bray, M. J. Ford, M. Toth, and I. Aharonovich, Nature nanotechnology **11**, 37 (2016).
[12] A. Lohrmann, B. C. Johnson, J. C. McCallum, and S. Castelletto, Reports on Progress in Physics **80**, 034502 (2017).
[13] I. Aharonovich, D. Englund, and M. Toth, Nature Photonics **10**, 631 (2016).
[14] C. Chakraborty, L. Kinnischtzke, K. M. Goodfellow, R. Beams, and A. N. Vamivakas, Nature nanotechnology **10**, 507 (2015).
[15] Y.-M. He, G. Clark, J. R. Schaibley, Y. He, M.-C. Chen, Y.-J. Wei, X. Ding, Q. Zhang, W. Yao, and X. Xu, Nature nanotechnology **10**, 497 (2015).
[16] M. Koperski, K. Nogajewski, A. Arora, V. Cherkez, P. Mallet, J.-Y. Veuillen, J. Marcus, P. Kossacki, and M. Potemski, Nature nanotechnology **10**, 503 (2015).
[17] S. Kumar, A. Kaczmarczyk, and B. D. Gerardot, Nano letters **15**, 7567 (2015).
[18] A. Srivastava, M. Sidler, A. V. Allain, D. S. Lembke, A. Kis, and A. Imamoğlu, Nature nanotechnology **10**, 491 (2015).

[19] P. Tonndorf, R. Schmidt, R. Schneider, J. Kern, M. Buscema, G. A. Steele, A. Castellanos-Gomez, H. S. van der Zant, S. M. de Vasconcellos, and R. Bratschitsch, Optica **2**, 347 (2015).
[20] J. Kern, I. Niehues, P. Tonndorf, R. Schmidt, D. Wigger, R. Schneider, T. Stiehm, S. Michaelis de Vasconcellos, D. E. Reiter, and T. Kuhn, Advanced Materials **28**, 7101 (2016).
[21] T. T. Tran, C. Elbadawi, D. Totonjian, C. J. Lobo, G. Grosso, H. Moon, D. R. Englund, M. J. Ford, I. Aharonovich, and M. Toth, ACS Nano **10**, 7331 (2016).
[22] T. T. Tran, C. Zachreson, A. M. Berhane, K. Bray, R. G. Sandstrom, L. H. Li, T. Taniguchi, K. Watanabe, I. Aharonovich, and M. Toth, Physical Review Applied **5**, 034005 (2016).
[23] N. R. Jungwirth, B. Calderon, Y. Ji, M. G. Spencer, M. E. Flatté, and G. D. Fuchs, Nano letters **16**, 6052 (2016).
[24] L. Martínez, T. Pelini, V. Waselowski, J. Maze, B. Gil, G. Cassabois, and V. Jacques, Physical Review B **94**, 121405 (2016).
[25] A. W. Schell, H. Takashima, T. T. Tran, I. Aharonovich, and S. Takeuchi, ACS Photonics **4**, 761 (2017).
[26] N. R. Jungwirth and G. D. Fuchs, Physical Review Letters **119**, 057401 (2017).
[27] X. Li, G. D. Shepard, A. Cupo, N. Camporeale, K. Shayan, Y. Luo, V. Meunier, and S. Strauf, ACS nano **11**, 6652 (2017).
[28] A. L. Exarhos, D. A. Hopper, R. R. Grote, A. Alkauskas, and L. C. Bassett, ACS nano **11**, 3328 (2017).
[29] L. Museur, E. Feldbach, and A. Kanaev, Physical Review B **78**, 155204 (2008).
[30] R. Bourrellier, S. Meuret, A. Tararan, O. Stéphan, M. Kociak, L. H. Tizei, and A. Zobelli, Nano letters **16**, 4317 (2016).
[31] T. Vuong, G. Cassabois, P. Valvin, A. Ouerghi, Y. Chassagneux, C. Voisin, and B. Gil, Physical review letters **117**, 097402 (2016).
[32] G. Grosso, H. Moon, B. Lienhard, A. Sajid, D. K. Efetov, M. M. Furchi, P. Jarillo-Herrero, M. J. Ford, I. Aharonovich, and D. Englund, Nature Communications **8**, 705 (2017).
[33] I. Aharonovich and E. Neu, Advanced Optical Materials **2**, 911 (2014).
[34] T. Plakhotnik, M. W. Doherty, and N. B. Manson, Physical Review B **92**, 081203 (2015).
[35] A. Lohrmann, B. Johnson, J. McCallum, and S. Castelletto, Reports on Progress in Physics **80**, 034502 (2017).
[36] S. A. C. McDowell, R. D. Amos, and N. C. Handy, Chem. Phys. Lett. **235**, 4 (1995).
[37] A. Spielfiedel and N. C. Handy, Phys. Chem. Chem. Phys. **1**, 2383 (1999).
[38] Z.-L. Cai and J. R. Reimers, J. Chem. Phys. **112**, 527 (2000).

[39] Z.-L. Cai, D. J. Tozer, and J. R. Reimers, J. Chem. Phys. **113**, 7084 (2000).
[40] Z.-L. Cai and J. R. Reimers, J. Phys. Chem. A **106**, 8769 (2002).
[41] Z.-L. Cai, K. Sendt, and J. R. Reimers, J. Chem. Phys. **117**, 5543 (2002).
[42] Z.-L. Cai, M. J. Crossley, J. R. Reimers, R. Kobayashi, and R. D. Amos, J. Phys. Chem. B **110**, 15624 (2006).
[43] M. J. G. Peach, P. Benfield, T. Helgaker, and D. J. Tozer, The Journal of Chemical Physics **128**, 044118 (2008).
[44] A. Sajid, S. A. Tawfik, M. Fronzi, M. Kianinia, T. T. Tran, C. Stampfl, I. Aharonovich, M. Toth, and M. J. Ford, Nanoscale **9**, 13575 (2017).
[45] G. Cassabois, P. Valvin, and B. Gil, Nature Photonics **10**, 262 (2016).
[46] D. Wickramaratne, L. Weston, and C. G. Van de Walle, The Journal of Physical Chemistry C **122**, 25524 (2018).
[47] K. Watanabe, T. Taniguchi, and K. Kanda, in *Nature Materials*2004), p. 404.
[48] P. Jaffernnou et al, in *Journal of Applied Physics*, **106**, 8769 p. 116102.
[49] K. Watanabe et al, in *Diamond and Related Materials*2011), **105**, 8769 p. 849.
[50] A. Pierret et al, in *Physical Review B*, **116**, 8769 (2014).
[51] R. Bourrelllier et al, in *ACS Photonics*2014), **110**, (2015).
[52] K. Watanabe and T. Taniguchi, in *International Journal of Applied Ceramics Technology*2011) **109**, 8769, (2016).
[53] G. Silly et al, in *Physical Review B* **106**, 8769,(2017).
[54] L. Museur and A. Kanaev, in *Journal of Applied Physics***106**, 8769, (2017).
[55] L. Museur, E. Feldbach, and A. Kanaev, in *Physical Review B* **106**, 8769,(2018).
[56] L. J. Martinez, T. Pelini, V. Waselowski, J. R. Maze, B. Gil, G. Cassebois, and V. Jacques, in *Physical Review B* **106**, 8769, (2018).
[57] C. Monroe, Nature **416**, 238 (2002).
[58] P. Michler, *Quantum Dots for Quantum Information Technologies* (Springer, 2017).
[59] E. Lucero, M. Hofheinz, M. Ansmann, R. C. Bialczak, N. Katz, M. Neeley, A. O'Connell, H. Wang, A. Cleland, and J. M. Martinis, Physical review letters **100**, 247001 (2008).
[60] A. Kuhn, M. Hennrich, and G. Rempe, Physical review letters **89**, 067901 (2002).
[61] C. Santori, M. Pelton, G. Solomon, Y. Dale, and Y. Yamamoto, Physical Review Letters **86**, 1502 (2001).
[62] R. B. Patel, A. J. Bennett, I. Farrer, C. A. Nicoll, D. A. Ritchie, and A. J. Shields, Nature photonics **4**, 632 (2010).
[63] J. Weber, Proc. Natl. Acad. Sci. USA **107**, 8513 (2010).

[64] J. J. Pla, K. Y. Tan, J. P. Dehollain, W. H. Lim, J. J. Morton, D. N. Jamieson, A. S. Dzurak, and A. Morello, Nature **489**, 541 (2012).
[65] I. Aharonovich, S. Castelletto, D. Simpson, C. Su, A. Greentree, and S. Prawer, Reports on progress in Physics **74**, 076501 (2011).
[66] R. Schirhagl, K. Chang, M. Loretz, and C. L. Degen, Annual review of physical chemistry **65**, 83 (2014).
[67] N. Elke, S. David, R.-M. Janine, G. Stefan, F. Martin, S. Matthias, and B. Christoph, New Journal of Physics **13**, 025012 (2011).
[68] G. Davies, Reports on Progress in Physics **44**, 787 (1981).
[69] A. Dietrich, K. D. Jahnke, J. M. Binder, T. Teraji, J. Isoya, L. J. Rogers, and F. Jelezko, New Journal of Physics **16**, 113019 (2014).
[70] B. Lienhard, T. Schröder, S. Mouradian, F. Dolde, T. T. Tran, I. Aharonovich, and D. Englund, Optica **3**, 768 (2016).
[71] A. W. Schell, M. Svedendahl, and R. Quidant, Advanced Materials **30**, 1704237 (2018).
[72] S. Choi, T. T. Tran, C. Elbadawi, C. Lobo, X. W. Wang, S. Juodkazis, G. Seniutinas, M. Toth, and I. Aharonovich, Acs Applied Materials & Interfaces **8**, 29642 (2016).
[73] M. Abdi, J.-P. Chou, A. Gali, and M. B. Plenio, ACS Photonics **5**, 1967 (2018).
[74] M. Abdi, M. J. Hwang, M. Aghtar, and M. B. Plenio, Physical Review Letters **119**, 233602 (2017).
[75] N. R. Jungwirth and G. D. Fuchs, Phys. Rev. Lett. **119**, 057401 (2017).
[76] X. Z. Li, G. D. Shepard, A. Cupo, N. Camporeale, K. Shayan, Y. Luo, V. Meunier, and S. Strauf, Acs Nano **11**, 6652 (2017).
[77] T. Vogl, Y. R. Lu, and P. K. Lam, Journal of Physics D-Applied Physics **50**, 295101 (2017).
[78] F. Wu, A. Galatas, R. Sundararaman, D. Rocca, and Y. Ping, Physical Review Materials **1**, 071001 (2017).
[79] A. L. Exarhos, D. A. Hopper, R. N. Patel, M. W. Doherty, and L. C. Bassett, arXiv preprint arXiv:1804.09061 (2018).
[80] S. Kim, M. Toth, and I. Aharonovich, Beilstein Journal of Nanotechnology **9**, 102 (2018).
[81] M. Koperski, K. Nogajewski, and M. Potemski, Optics Communications **411**, 158 (2018).
[82] J. R. Reimers, A. Sajid, R. Kobayashi, and M. J. Ford, Journal of Chemical Theory and Computation **14**, 1602 (2018).
[83] A. Sajid, J. R. Reimers, and M. J. Ford, Physical Review B **97**, 064101 (2018).

[84] J. Ziegler, A. Blaikie, A. Fathalizadeh, D. Miller, F. S. Yasin, K. Williams, J. Mohrhardt, B. J. McMorran, A. Zettl, and B. Aleman, Nano Letters **18**, 2683 (2018).
[85] A. W. Schell, H. Takashima, T. T. Tran, I. Aharonovich, S. Takeuchi, and Ieee, in *2017 Conference on Lasers and Electro-Optics*2017).
[86] N. R. Jungwirth, B. Calderon, Y. X. Ji, M. G. Spencer, M. E. Flatte, and G. D. Fuchs, Nano Letters **16**, 6052 (2016).
[87] L. J. Martinez, T. Pelini, V. Waselowski, J. R. Maze, B. Gil, G. Cassabois, and V. Jacques, Physical Review B **94**, 121405 (2016).
[88] M. Kianinia, C. Bradac, B. Sontheimer, F. Wang, T. T. Tran, M. Nguyen, S. Kim, Z.-Q. Xu, D. Jin, and A. W. Schell, Nature communications **9**, 874 (2018).
[89] A. W. Schell, T. T. Tran, H. Takashima, S. Takeuchi, and I. Aharonovich, Apl Photonics **1**, 091302 (2016).
[90] Z. Shotan, H. Jayakumar, C. R. Considine, M. Mackoit, H. Fedder, J. Wrachtrup, A. Alkauskas, M. W. Doherty, V. M. Menon, and C. A. Meriles, Acs Photonics **3**, 2490 (2016).
[91] E. U. Condon, Phys. Rev. **32**, 858 (1928).
[92] G. Herzberg and E. Teller, Z. Phys. Chem. **21**, 410 (1933).
[93] G. Fischer, *Vibronic Coupling* (Academic Press, London, 1984).
[94] E. B. Wilson, J. C. Decius, and P. C. Cross, *Molecular Vibrations: The Theory of Infrared and Raman Vibrational Spectra* (McGraw-Hill Book Company, New York, 1955).
[95] F. A. Cotton, *Chemical Applications of Group Theory* (Wiley, New York, 1971).
[96] B. Sontheimer, M. Braun, N. Nikolay, N. Sadzak, I. Aharonovich, and O. Benson, Physical Review B **96**, 121202 (2017).
[97] J. Toledo, D. de Jesus, M. Kianinia, A. Leal, C. Fantini, L. Cury, G. Sáfar, I. Aharonovich, and K. Krambrock, arXiv preprint arXiv:1807.05393 (2018).
[98] T. Q. P. Vuong, G. Cassabois, P. Valvin, A. Ouerghi, Y. Chassagneux, C. Voisin, and B. Gil, Physical Review Letters **117**, 097402 (2016).
[99] M. Kianinia, B. Regan, S. A. Tawfik, T. T. Tran, M. J. Ford, I. Aharonovich, and M. Toth, Acs Photonics **4**, 768 (2017).
[100] A. Gali, M. Fyta, and E. Kaxiras, Physical Review B **77**, 155206 (2008).
[101] K. Szász, T. Hornos, M. Marsman, and A. Gali, Physical Review B **88**, 075202 (2013).
[102] K. Szász, X. T. Trinh, N. T. Son, E. Janzén, and A. Gali, Journal of Applied Physics **115**, 073705 (2014).
[103] K. Szász, V. Ivády, I. A. Abrikosov, E. Janzén, M. Bockstedte, and A. Gali, Physical Review B **91**, 121201 (2015).

[104] J. C. C. Freitas, W. L. Scopel, W. S. Paz, L. V. Bernardes, F. E. Cunha-Filho, C. Speglich, F. M. Araújo-Moreira, D. Pelc, T. Cvitanić, and M. Požek, Nature Sci. Rep. **5**, 14761 (2015).
[105] K. S. Novoselov, D. Jiang, F. Schedin, T. J. Booth, V. V. Khotkevich, S. V. Morozov, and A. K. Geim, Proceedings of the National Academy of Sciences of the United States of America **102**, 10451 (2005).
[106] O. L. Krivanek, M. F. Chisholm, V. Nicolosi, T. J. Pennycook, G. J. Corbin, N. Dellby, M. F. Murfitt, C. S. Own, Z. S. Szilagyi, M. P. Oxley, S. T. Pantelides, and S. J. Pennycook, Nature **464**, 571 (2010).
[107] J. C. Meyer, A. Chuvilin, G. Algara-Siller, J. Biskupek, and U. Kaiser, Nano Letters **9**, 2683 (2009).
[108] J.-W. Feng and J.-X. Zhao, Journal of molecular modeling **20**, 2197 (2014).
[109] A. Katzir, J. Suss, A. Zunger, and A. Halperin, Physical Review B **11**, 2370 (1975).
[110] A. Zunger and A. Katzir, Physical review B **11**, 2378 (1975).
[111] E. Andrei, A. Katzir, and J. Suss, Physical Review B **13**, 2831 (1976).
[112] D. Geist and G. Römelt, Solid State Communications **2**, 149 (1964).
[113] A. Moore and L. Singer, Journal of Physics and Chemistry of Solids **33**, 343 (1972).
[114] M. Fanciulli, & Moustakas, T.D., in *Proceedings of wide band gap semiconductors*Washington, DC (United States), 1992).
[115] M. Silly, P. Jaffrennou, J. Barjon, J.-S. Lauret, F. Ducastelle, A. Loiseau, E. Obraztsova, B. Attal-Tretout, and E. Rosencher, Physical Review B **75**, 085205 (2007).
[116] L. Ci, L. Song, C. Jin, D. Jariwala, D. Wu, Y. Li, A. Srivastava, Z. Wang, K. Storr, and L. Balicas, Nature materials **9**, 430 (2010).
[117] M. Abdi, J.-P. Chou, A. Gali, and M. Plenio, (2017).
[118] L. Weston, D. Wickramaratne, M. Mackoit, A. Alkauskas, and C. G. Van de Walle, Physical Review B **97**, 214104 (2018).
[119] T. T. Tran, C. Elbadawi, D. Totonjian, C. J. Lobo, G. Grosso, H. Moon, D. R. Englund, M. J. Ford, I. Aharonovich, M. Toth, and Ieee, in *2017 Conference on Lasers and Electro-Optics*2017).
[120] C. Elbadawi, T. T. Tran, O. Shimoni, D. Totonjian, C. J. Lobo, G. Grosso, H. Moon, D. R. Englund, M. J. Ford, I. Aharonovich, and M. Toth, in *Spie Biophotonics Australasia*, edited by M. R. Hutchinson, and E. M. Goldys2016).
[121] A. Audrius, B. B. Bob, D. A. David, and G. V. d. W. Chris, New Journal of Physics **16**, 073026 (2014).
[122] A. Sajid, J. R. Reimers, R. Kobayashi, and M. J. Ford, (Submitted).
[123] G. Noh, D. Choi, J.-H. Kim, D.-G. Im, Y.-H. Kim, H. Seo, and J. Lee, Nano Letters (2018).

[124] G. D. Cheng, Y. G. Zhang, L. Yan, H. F. Huang, Q. Huang, Y. X. Song, Y. Chen, and Z. Tang, Computational Materials Science **129**, 247 (2017).
[125] J. R. Maze, A. Gali, E. Togan, Y. Chu, A. Trifonov, E. Kaxiras, and M. D. Lukin, New Journal of Physics **13**, 025025 (2011).
[126] M. Dubecký, P. Jurečka, R. Derian, P. Hobza, M. Otyepka, and L. Mitas, Journal of Chemical Theory and Computation **9**, 4287 (2013).
[127] G. P. Purvis, III and R. J. Bartlett, J. Chem. Phys. **76**, 1910 (1982).
[128] K. Raghavachari, G. W. Trucks, J. A. Pople, and M. Head-Gordon, Chem. Phys. Lett. **157**, 479 (1989).
[129] J. F. Stanton and R. J. Bartlett, J. Chem. Phys. **98**, 7029 (1993).
[130] T. Korona and H.-J. Werner, J. Chem. Phys. **118**, 3006 (2003).
[131] E. R. Davidson, Int. J. Quant. Chem. **8**, 61 (1974).
[132] D. Hegarty and M. A. Robb, Molec. Phys. **38**, 1795 (1979).
[133] K. Andersson, P.-Å. Malmqvist, and B. O. Roos, J. Chem. Phys. **96**, 1218 (1992).
[134] A. S. Zyubin, A. M. Mebel, M. Hayashi, H. C. Chang, and S. H. Lin, J. Comput. Chem. **30**, 119 (2009).
[135] J. D. Watts and R. J. Bartlett, Chem. Phys. Letts. **233**, 81 (1995).
[136] M. Del Ben, J. Hutter, and J. VandeVondele, The Journal of Chemical Physics **143**, 102803 (2015).
[137] K. Eichkorn, O. Treutler, H. Öhm, M. Häser, and R. Ahlrichs, Chem. Phys. Letts. **242**, 652 (1995).
[138] C. Hättig and F. Weigend, J. Chem. Phys. **113**, 5154 (2000).
[139] D. Usvyat, L. Maschio, and M. Schütz, The Journal of Chemical Physics **143**, 102805 (2015).
[140] F. Weigend and M. Häser, Theor. Chem. Acta **97**, 331 (1997).
[141] Z. Rolik, L. Szegedy, I. Ladjánszki, B. Ladóczki, and M. Kállay, The Journal of Chemical Physics **139**, 094105 (2013).
[142] A. Grüneis, The Journal of Chemical Physics **143**, 102817 (2015).
[143] A. B. J. Parusel and S. Grimme, J. Phys. Chem. B **104**, 5395 (2000).
[144] M. P. d. Lara-Castells, H. Stoll, B. Civalleri, M. Causa, E. Voloshina, A. O. Mitrushchenkov, and M. Pi, J. Chem. Phys. **141**, 151102 (2014).
[145] M. P. De Lara-Castells, M. Bartolomei, A. O. Mitrushchenkov, and H. Stoll, Journal of Chemical Physics **143**, 194701, 194701 (2015).
[146] M. P. de Lara-Castells, A. O. Mitrushchenkov, and H. Stoll, The Journal of Chemical Physics **143**, 102804 (2015).
[147] M. P. d. Lara-Castells, R. Fernandez-Perea, F. Madzharova, and E. Voloshina, J. Chem. Phys. **144**, 244707 (2016).
[148] A. Heßelmann, G. Jansen, and M. Schütz, Journal of Chemical Physics **122**, 014103 (2005).
[149] A. Heßelmann, The Journal of Chemical Physics **128**, 144112 (2008).

[150] M. Pitoňák and A. Heßelmann, Journal of Chemical Theory and Computation **6**, 168 (2010).
[151] A. J. Misquitta, B. Jeziorski, and K. Szalewicz, Physical Review Letters **91**, 033201 (2003).
[152] C. Tuma and J. Sauer, The Journal of Chemical Physics **143**, 102810 (2015).
[153] M. Marsman, A. Grüneis, J. Paier, and G. Kresse, Journal of Chemical Physics **130**, 184103 (2009).
[154] L. Schimka, J. Harl, A. Stroppa, A. Grüneis, M. Marsman, F. Mittendorfer, and G. Kresse, Nature Materials **9**, 741 (2010).
[155] K. Andersson, P. Å. Malmqvist, and B. O. Roos, The Journal of chemical physics **96**, 1218 (1992).
[156] K. Shamasundar, G. Knizia, and H.-J. Werner, The Journal of chemical physics **135**, 054101 (2011).
[157] D. Wang, D. Han, X.-B. Li, S.-Y. Xie, N.-K. Chen, W. Q. Tian, D. West, H.-B. Sun, and S. B. Zhang, Phys. Rev. Lett. **114**, 196801 (2015).
[158] D. Wang, D. Han, X.-B. Li, S.-Y. Xie, N.-K. Chen, W. Q. Tian, D. West, H.-B. Sun, and S. B. Zhang, Physical Review Letters **114**, 196801 (2015).
[159] A. Csóré, H. J. von Bardeleben, J. L. Cantin, and A. Gali, Physical Review B **96**, 085204 (2017).
[160] R. A. Friesner, in *Proceedings of the National Academy of Sciences*2005), pp. 6648.
[161] W. Kohn, *Electronic structure of matter–wave functions and density functionals* 2003), Nobel Lectures: Chemistry.
[162] P. Hohenberg and W. Kohn, Physical review **136**, B864 (1964).
[163] O. Gunnarsson and B. I. Lundqvist, Phys. Rev. B **13**, 4274 (1976).
[164] J. Heyd, G. E. Scuseria, and M. Ernzerhof, The Journal of Chemical Physics **118**, 8207 (2003).
[165] A. V. Krukau, O. A. Vydrov, A. F. Izmaylov, and G. E. Scuseria, The Journal of Chemical Physics **125**, 224106 (2006).
[166] G. Kresse and J. Furthmüller, Comput. Mat. Sci. **6**, 15 (1996).
[167] G. Kresse and J. Hafner, Phys. Rev. B **47**, 558 (1993).
[168] T. Yanai, D. P. Tew, and N. C. Handy, Chem. Phys. Lett. **393**, 51 (2004).
[169] R. Kobayashi and R. D. Amos, Chem. Phys. Lett. **420**, 106 (2006).
[170] Q. Wu and T. Van Voorhis, Physical Review A **72**, 024502 (2005).
[171] Q. Wu and T. Van Voorhis, The Journal of Physical Chemistry A **110**, 9212 (2006).
[172] B. Kaduk, T. Kowalczyk, and T. Van Voorhis, Chemical reviews **112**, 321 (2011).
[173] E. Gross and W. Kohn, in *Advances in quantum chemistry* (Elsevier, 1990), pp. 255.

[174] M. S. Dresselhaus, G. Dresselhaus, and A. Jorio, Berlin, Heidelberg: Springer Berlin Heidelberg **10**, 978 (2008).
[175] J. P. Perdew, W. Burke, and M. Ernzerhof, Phys. Rev. Lett. **77**, 3865 (1996).
[176] P. Ordejon, D. Sanchez-Portal, A. Garcia, E. Artacho, J. Junquera, and J. M. Soler, RIKEN Review **29**, 42 (2000).
[177] J. M. Soler, E. Artacho, J. D. Gale, A. Garcia, J. Junquera, P. Ordejon, and D. Sanchez-Portal, J. Phys.: Condens. Matter **14**, 2745 (2002).
[178] P. E. Blöchl, Physical review B **50**, 17953 (1994).
[179] G. Kresse and D. Joubert, Phys. Rev. B **59**, 1758 (1999).
[180] V. Ivády, T. Simon, J. R. Maze, I. Abrikosov, and A. Gali, Physical Review B **90**, 235205 (2014).
[181] R. O. Jones and O. Gunnarsson, Reviews of Modern Physics **61**, 689 (1989).
[182] P. J. Knowles, R. Lindh, F. R. Manby, M. Schütz, and e. al, *MOLPRO, version 2010.1, a package of ab initio programs* (University of Birmingham, Birmingham, 2010).
[183] M. J. Frisch, G. W. Trucks, H. B. Schlegel, G. E. Scuseria, M. A. Robb, J. R. Cheeseman, G. Scalmani, V. Barone, G. A. Petersson, H. Nakatsuji, X. Li, M. Caricato, A. V. Marenich, J. Bloino, B. G. Janesko, R. Gomperts, B. Mennucci, H. P. Hratchian, J. V. Ortiz, A. F. Izmaylov, J. L. Sonnenberg, Williams, F. Ding, F. Lipparini, F. Egidi, J. Goings, B. Peng, A. Petrone, T. Henderson, D. Ranasinghe, V. G. Zakrzewski, J. Gao, N. Rega, G. Zheng, W. Liang, M. Hada, M. Ehara, K. Toyota, R. Fukuda, J. Hasegawa, M. Ishida, T. Nakajima, Y. Honda, O. Kitao, H. Nakai, T. Vreven, K. Throssell, J. A. Montgomery Jr., J. E. Peralta, F. Ogliaro, M. J. Bearpark, J. J. Heyd, E. N. Brothers, K. N. Kudin, V. N. Staroverov, T. A. Keith, R. Kobayashi, J. Normand, K. Raghavachari, A. P. Rendell, J. C. Burant, S. S. Iyengar, J. Tomasi, M. Cossi, J. M. Millam, M. Klene, C. Adamo, R. Cammi, J. W. Ochterski, R. L. Martin, K. Morokuma, O. Farkas, J. B. Foresman, and D. J. Fox, Gaussian 16, 2016.
[184] J. R. Reimers, The Journal of Chemical Physics **115**, 9103 (2001).
[185] Z.-Q. Xu, C. Elbadawi, T. T. Tran, M. Kianinia, X. Li, D. Liu, T. B. Hoffman, M. Nguyen, S. Kim, and J. H. Edgar, Nanoscale **10**, 7957 (2018).
[186] S. Ali, S. A. Tawfik, M. Fronzi, M. Kianinia, T. T. Tran, C. Stampfl, I. Aharonovich, M. Toth, and M. J. Ford, Nanoscale (2017).
[187] A. Sajid, J. R. Reimers, and M. J. Ford, Physical Review B **97**, 064101 (2018).
[188] S. A. Tawfik, J. R. Reimers, C. Stampfl, and M. J. Ford, arXiv preprint arXiv:1805.11252 (2018).
[189] C. Freysoldt, B. Grabowski, T. Hickel, J. Neugebauer, G. Kresse, A. Janotti, and C. G. Van de Walle, Reviews of modern physics **86**, 253 (2014).

[190] G. Makov and M. Payne, Phys. Rev. B **51**, 4014 (1995).
[191] A. Alkauskas, B. B. Buckley, D. D. Awschalom, and C. G. Van de Walle, New Journal of Physics **16**, 073026 (2014).
[192] R. Bourrellier, S. Meuret, A. Tararan, O. Stéphan, M. Kociak, L. H. Tizei, and A. Zobelli, Nano Lett. **16**, 4317 (2016).
[193] S. N. Grinyaev, F. V. Konusov, V. Lopatin, and L. N. Shiyan, Physics of the solid state **46**, 435 (2004).
[194] B. Huang and H. Lee, Physical Review B **86**, 245406 (2012).
[195] M. S. Si and D. S. Xue, Physical Review B **75**, 193409 (2007).
[196] C. Attaccalite, M. Bockstedte, A. Marini, A. Rubio, and L. Wirtz, Physical Review B **83**, 144115 (2011).
[197] N. Berseneva, A. Gulans, A. V. Krasheninnikov, and R. M. Nieminen, Physical Review B **87**, 035404 (2013).
[198] A. Reinberg, The Journal of Chemical Physics **41**, 850 (1964).
[199] P. O. Löwdin, Advances in chemical physics, 207 (1958).
[200] S. A. Tawfik, S. Ali, M. Fronzi, M. Kianinia, T. T. Tran, C. Stampfl, I. Aharonovich, M. Toth, and M. J. Ford, Nanoscale **9**, 13575 (2017).
[201] A. Sajid, J. R. Reimers, and M. J. Ford, Phys. Rev. B **97**, 064101 (2018).
[202] S. Azevedo, J. R. Kaschny, C. M. de Castilho, and F. de Brito Mota, Nanotechnology **18**, 495707 (2007).
[203] T. Schmidt, R. Baierle, P. Piquini, and A. Fazzio, Physical Review B **67**, 113407 (2003).
[204] W. Orellana and H. Chacham, Physical Review B **63**, 125205 (2001).
[205] R.-F. Liu and C. Cheng, Physical Review B **76**, 014405 (2007).
[206] W. Kohn and L. J. Sham, Physical Review **140**, A1133 (1965).
[207] U. von Barth, Physical Review A **20**, 1693 (1979).
[208] J. R. Reimers, Z.-L. Cai, R. Kobayashi, M. Rätsep, A. Freiberg, and E. Krausz, Sci. Rep. **3**, 2761 (2013).
[209] M. Rätsep, Z.-L. Cai, J. R. Reimers, and A. Freiberg, J. Chem. Phys. **134**, 024506/1 (2011).
[210] J. R. Reimers, L. McKemmish, R. H. McKenzie, and N. S. Hush, Phys. Chem. Chem. Phys. **17**, 24598 (2015).
[211] T. Van Voorhis, T. Kowalczyk, B. Kaduk, L.-P. Wang, C.-L. Cheng, and Q. Wu, Annu. Rev. Phys. Chem. **61**, 149 (2010).
[212] D. J. Tozer and N. C. Handy, J. Chem. Phys. **109**, 10180 (1998).
[213] J. R. Reimers, L. McKemmish, R. H. McKenzie, and N. S. Hush, Phys. Chem. Chem. Phys. **17**, 24640 (2015).
[214] M. Abdi, M.-J. Hwang, M. Aghtar, and M. B. Plenio, Phys. Rev. Lett. **119**, 233602 (2017).
[215] M. Bockstedte, F. Schultz, T. Garrat, V. Ivady, and A. Gali, Quantum Materials **3**, 31 (2018).

[216] G. Li Manni, R. K. Carlson, S. Luo, D. Ma, J. Olsen, D. G. Truhlar, and L. Gagliardi, Journal of chemical theory and computation **10**, 3669 (2014).
[217] J. R. Reimers and N. S. Hush, J. Am. Chem. Soc. **117**, 1302 (1995).
[218] J. Zeng, N. S. Hush, and J. R. Reimers, J. Am. Chem. Soc. **118**, 2059 (1996).
[219] R. M. Feenstra, N. Srivastava, Q. Gao, M. Widom, B. Diaconescu, T. Ohta, G. L. Kellogg, J. T. Robinson, and I. V. Vlassiouk, Physical Review B **87**, 041406 (2013).
[220] M. Tinkham, *Group theory and quantum mechanics* (Courier Corporation, 2003).
[221] F. J. Heremans, C. G. Yale, and D. D. Awschalom, Proceedings of the IEEE **104**, 2009 (2016).
[222] D. Lee, K. W. Lee, J. V. Cady, P. Ovartchaiyapong, and A. C. B. Jayich, Journal of Optics **19**, 033001 (2017).
[223] P. Udvarhelyi, G. Thiering, E. Londero, and A. Gali, Physical Review B **96**, 155211 (2017).
[224] J. R. Reimers, J. Chem. Phys. **115**, 9103 (2001).
[225] V. Ivády, I. A. Abrikosov, and A. Gali, npj Computational Materials **4**, 76 (2018).
[226] G. Thiering and A. Gali, Physical Review B **98**, 085207 (2018).

Appendix

Table 0.1 The calculated principle values of HF tensor on nearby atoms at distance d from the defect centre, in MHz, for various ground-state (GS) defects in h-BN, with also the average principle values of the HF coupling tensor $(A_{xx}+A_{yy}+A_{zz})/3$. Key interatomic distances d are also listed.

Defect	Symm.	Atoms	*d* (Å)	A_{xx}	A_{yy}	A_{zz}	$(A_{xx}+A_{yy}+A_{zz}/3)$
V_N	D_{3h}	**B_1-B_3**	**1.27**	**19**	**19**	**57**	32(22)[b]
		B_4-B_6	2.88	6	5	14	8
		N_1-N_6	2.42	-2	-1	-3	-2
V_N^{-1}	D_{3h}	**B_1-B_3**	**1.13**	**0**	**0**	**0**	0[c]
C_N	D_{3h}	C	0	40	40	208	96
		B_1-B_3	**1.49**	**-16**	**-14**	**-22**	-17(-18)[d]
		B_4-B_9	2.89	-2	-1	-2	-2
		N_1-N_6	2.53	1	0	5	2
V_NO_{2B}	C_s	**B_1**	**1.41**	**529**	**519**	**615**	554(506)[c]
		B_2-B_3	3.77	21	21	27	23
		B_4-B_5	2.86	12	12	16	13
		B_6	2.90	-3	-2	-5	-3
		N_1-N_2	2.42	22	21	31	25
		N_3-N_4	2.61	4	4	5	4
		O_1-O_2	1.41	-215	-209	-215	-213
V_NN_B	C_{2v}	N_1	1.37	31	29	139	66
		N_2-N_3	2.40	-2	-1	12	3
		N_4	4.25	1	1	5	2
		B_1-B_2	1.37	4	0	8	4
		B_3-B_4	3.73	1	0	-3	-1
$^3V_NC_B$[e]	C_{2v}	C	1.35	497	418	503	473
		B_1-B_2	1.35	70	64	76	70
		B_3-B_4	3.70	14	12	17	14
		B_5-B_6	2.73	8	4	11	8
		N_1-N_2	2.36	7	5	10	7
		N_3-N_4	2.62	7	7	10	8
V_BC_N	C_{2v}	C	1.37	-31	6	109	28
		B_1-B_2	2.58	-5	-5	-8	-6
		B_3-B_4	2.54	-3	-1	6	1
		N_1-N_2	1.37	54	52	93	66
		N_3-N_6	3.64	4	4	6	5
		N_7-N_8	3.04	1	0	3	1
$V_BC_NSi_N$	C_s	Si	0	90	67	96	84
		C	2.77	32	30	47	36
		B_1	2.23	311	304	398	338
		B_2	2.08	166	164	206	179
		B_3	4.27	17	17	24	19
		B_4	4.64	14	14	18	15
		B_5	2.69	13	12	17	14
		B_6	2.89	12	11	16	13
		B_7	4.14	12	11	15	13
		N_1	1.74	19	19	26	21
		N_2	2.73	14	13	20	16
		N_3	2.87	13	11	20	15
		N_4	3.37	9	8	13	10
$V_NC_BSi_B$	C_s	Si	0	-28	-26	-145	-66
		C	1.91	23	22	106	50
		N_1	1.79	2	1	4	2
		N_2-N_3	2.9	-1	0	7	2
		N_4	4.79	1	1	3	2
		B_1	2.65	4	3	11	6
		B_2	3.54	3	2	8	4

[a] The values reported are for B^{11}, N^{14}, C^{13} and O^{17} isotopes, with only atoms with signal great than 2 MHz listed. Contributions from atoms interpreted as accounting for observed signals are highlighted in bold. The Fermi contact terms are listed without (with) core contribution.

[b] In ref. [114], a signal is observed of magnitude $|A_{xx}+A_{yy}+A_{zz}|/3 = 22.43\pm1.4$ MHz that is attributed to an Nv centre.

[c] In Ref. [109], a signal is observed of magnitude $|A_{xx}+A_{yy}+A_{zz}|/3 = 117.06$ MHz that is attributed to an V_N^{-1} TBC, as well as a signal at 352.70 MHz attributed to an oxygen-containing V_NO_{2B} OBC.

[d] In Ref. [113], a signal is observed of magnitude $|A_{xx}+A_{yy}+A_{zz}|/3 = 20.83$ MHz that is attributed to the B^{11} atoms in a C_N TBC.

[e] The ground state is calculated to be $^1A_1$ and the results presented are for the lowest-energy triplet state, $^3B_1$.

Appendix

Table 0.2 Bond lengths around V_NN_B, V_NC_B, V_BC_N, $N_VB_CB_{Si}$ and $B_VN_CN_{Si}$ centres.

	V_NN_B		V_NC_B		V_BC_N		$N_VB_CB_{Si}$		$B_VN_CN_{Si}$
Bond Length(Ang)	B-N	2.57	B-C	2.60	B-C	1.55	Si-N	1.82	1.74
	B-B	1.94	B-B	1.92	N-N	2.65	Si-B	1.96	2.08
	N-N	1.36	C-N	1.35	C-N	2.38	Si-c	1.91	1.72

Table 0.3 Comparison of HSE06 energies of V_NC_B defect with size of the model compound (MC), MC's consisting of 25, 57 and 101 atoms are compared with periodic structures of V_NC_B.

	HSE06 Energies			
State	25 Atom MC	57 Atoms MC	101 Atoms MC	2D
$(1)^1A_1$	[0]			
$(2)^1A_1$				2.46
$(1)^1B_1$	1.54	1.07	0.96	1.08
$(2)^1B_1$	3.00	1.92		
$(1)^1B_2$	4.55			
$(2)^1B_2$	3.82			
$(1)^1A_2$	2.41	2.14		
$(2)^1A_2$	3.83	2.51		
$(1)^3A_1$	4.00	1.69	2.00	3.00
$(1)^3B_1$	[0.77]	0.43	0.32	0.34
$(2)^3B_1$	2.70	1.56	1.80	1.92
$(1)^3B_2$	4.02			
$(2)^3B_2$	4.24			
$(1)^3A_2$	2.28	1.68		
$(2)^3A_2$	3.11	2.07		
$(3)^3A_2$	4.47	2.44		